Dissertation

submitted to the

Combined Faculty of Mathematics, Engineering and Natural Sciences

of Heidelberg University, Germany

for the degree of

Doctor of Natural Sciences

Put forward by

Katharina I. Jerg

born in: Friedrichshafen, Germany

Oral examination: April 18th, 2024

Simulation-based Low-Dose-Rate Brachytherapy Treatment Planning

Referees: Prof. Dr. Jürgen W. Hesser
Prof. Dr. Mark E. Ladd

Simulation-based Low-Dose-Rate Brachytherapy Treatment Planning

During low-dose-rate brachytherapy radioactive seeds are inserted into a tumor using hollow needles. Treatment planning refers to defining seed positions such that dose parameters for both the target and the organs at risk obey certain constraints. State-of-the-art planning techniques allow to intra-operatively update the plan with actual seed positions, but do not consider seed placement uncertainties and resulting dose deviations beforehand.

We propose two strategies to be included in treatment planning, which can help to overcome the need for frequent plan updating. Firstly, a needle insertion simulation is introduced, without the necessity for boundary conforming meshing using an embedded domain method. Secondly, we quantify seed placement sensitivity by calculating the gradients of the dose parameters with respect to the seeds' positions.

Due to the limited need for human interaction, the introduced simulation offers a possibility to be included in brachytherapy treatment planning. However, large computation times hinder real-time applications. The sensitivity analysis using automatic differentiation can easily be integrated into existing treatment planning systems and has the following advantages: During planning the displacement tolerances serve as a measure of plan robustness and reduce the time for manual planning by indicating sensitive seeds. During seed placement the tolerances show acceptable placement deviations and thus reduce possible needle re-insertions.

Simulationsbasierte Brachytherapie-Behandlungsplanung mit niedriger Dosisrate

Während der Brachytherapie mit niedriger Dosisrate werden radioaktive Seeds mit hohlen Nadeln in einen Tumor eingebracht. Die Therapieplanung bezieht sich auf die Festlegung der Seed-Positionen, sodass Dosisparameter definierte Randbedinungen für das Zielvolumen und die Risikostrukturen erfüllen. Modernste Planungstechniken ermöglichen eine intraoperative Aktualisierung des Plans anhand der tatsächlichen Seed-Positionen, berücksichtigen jedoch nicht die Unsicherheiten bei der Seed-Platzierung und die daraus resultierenden Dosisabweichungen im Voraus.

Wir schlagen zwei Strategien vor, die in die Bestrahlungsplanung integriert werden können, um die Notwenigkeit der häufigen Plananpassung zu überwinden. Erstens wird eine Simulation der Nadelplatzierung eingeführt, die durch die sogenannte Embedded-Domain-Methode keine grenzkonformen Gitter benötigt. Zweitens quantifizieren wir die Empfindlichkeit der Seed-Platzierung, indem wir die Gradienten der Dosisparameter in Bezug auf die Seed-Positionen berechnen.

Aufgrund des begrenzten Bedarfs an menschlicher Interaktion bietet die vorgestellte Simulations-Methode die Möglichkeit, in die Brachytherapie-Behandlungsplanung aufgenommen zu werden. Große Rechenzeiten erschweren jedoch die Echtzeitanwendung. Die Sensitivitätsanalyse mittels automatischer Differenzierung kann problemlos in bestehende Behandlungsplanungssysteme integriert werden und bietet die folgenden Vorteile: Während der Planung dienen die Verschiebungstoleranzen als Maß für die Robustheit des Plans und reduzieren die Zeit für die manuelle Planung, indem sie sensible Seed-Positionen anzeigen. Bei der Implantation der Seeds zeigen die Toleranzen akzeptable Platzierungsabweichungen und reduzieren somit mögliche erneute Nadel-Einführungen.

"We can do all the things we've always wanted to do, but whether it benefits the patient is going to require a lot of careful study."

David Sher, M.D., Radiation Oncologist

Contents

List of Figures

List of Abbreviations

AAPM	American Association of Physicists in Medicine
DNA	Deoxyribonucleic acid
DVH	Dose volume histograms
EBRT	External beam radiation therapy
GEC-ESTRO	Groupe Européen de Curiethérapie and European Society for Radiotherapy and Oncology
HDR	High-dose-rate
ITP	Inverse treatment planning
I-125	Iodine-125
LDR	Low-dose-rate
OAR	Organ at risk
PINN	Physics informed neural network
RT	Radiation therapy
TPS	Treatment planning system
TRUS	Transrectal ultrasound

1 Introduction

1.1 Motivation

In 2020, there were more than 1.4 million new prostate cancer cases and 375,000 deaths related to prostate cancer worldwide [1, 2]. It is therefore the second most common cancer diagnosed in men after lung cancer [2]. Known risk factors are advancing age and dietary risk factors such as obesity among others [1]. Possible treatment options are surgery, external beam radiation therapy (EBRT), or brachytherapy. Retrospective studies show that the three treatment options all result in similar overall survival [3, 4]. Low-dose-rate (LDR) brachytherapy is a radiation therapy (RT) during which radioactive seeds are inserted into a tumor through hollow needles. Compared to EBRT, brachytherapy provides a better conformality and dose concentration [3] and has the lowest toxicity and less long term side effects compared to surgery and EBRT [4]. LDR brachytherapy treatment can be performed in one session. Having less hospital visits compared to EBRT is more convenient for the patient. Therefore, brachytherapy is a highly effective treatment for low risk localised prostate cancer when there is no evidence of metastases [4].

Despite its high effectiveness, LDR brachytherapy comes with different challenges. While patient positioning and monitoring of prostate gland motion is crucial for an accurate dose delivery in EBRT [5], there is an indication that systematic seed-displacements are the main cause for dosimetric variations in LDR brachytherapy [6]. The deviation of a seed's position from its planned position can either be due to the surgeon's accuracy, tissue motion, prostate swelling, or migration after the implantation [7]. During needle insertion prostate motion and deformation can vary greatly between patients and is often the cause for seed misplacement within the prostate [8]. In LDR brachytherapy beveled tip needles are used, which cause the needle to bend during insertion. On the one hand this can assist needle steering, but on the other hand this increases the complexity of needle placement. Treatment planning involves finding the most suitable seed positions for dose delivery inside the prostate, however, the process of inserting the needles is not considered.

State-of-the-art LDR brachytherapy strategies require frequent plan updates during the treatment and plan verification after seed implantation. This constant need for reaction and updating can be reduced when treatment plans are more robust against changes in seed positioning. It is shown that the use of robust treatment plans can limit the effect of a deviation of a seed's position on the resulting dose distribution [7], however, no information about plan robustness is available during treatment planning.

To summarize, there are two challenges during LDR prostate brachytherapy treatment

planning:
1) The needle insertion and corresponding tissue deformation is not considered during planning.
2) There is no information about the robustness of the treatment plan with respect to the seeds' positions.

1.2 State-of-the-art

State-of-the-art LDR brachytherapy treatment planning techniques address the problem of seed migration and seed misplacement. While in literature different terms are used, in this work seed migration refers to a post-operative motion of the seed, while seed misplacement refers to the deviation from the planned position due to a mispositioning of the needle during the implantation. In the following, clinical methods to limit seed migration and strategies to handle seed misplacement are explained. Since medical procedures profit from simulations, we want to examine how simulations can improve LDR brachytherapy treatment planning. Therefore, it is additionally shown how simulations are used to enhance medical applications and especially target the questions of needle insertions and plan robustness in LDR brachytherapy.

1.2.1 Seed migration

The challenge of seed migration is approached by connecting seeds to strands previous to insertion. It is shown that stranded seeds limit both seed migration [6] and seed loss, which is the movement of seeds to neighboring organs. This leads to higher dose in the prostate and less dose in undesirable locations [9, 10]. Even if seed migration can be restricted by stranded seeds, it cannot be fully be prevented. There is still migration reported, especially in craniocaudal direction [11, 12].

1.2.2 LDR treatment planning strategies to address seed misplacement

There are several techniques which can be employed in a hospital for LDR prostate brachytherapy treatment planning. The basic planning procedure is a pre-planning technique. This is a two-stage procedure, where transrectal ultrasound (TRUS) images are acquired from the patient in a first step and a treatment plan is created offline. In a second procedure the patient returns to the hospital, is repositioned and treated as per treatment plan. Despite the fact that offline planning gives the physician time to produce high quality and reproducible plans, pre-planning comes with the disadvantages of having

to match the patient's position and a possible change in prostate shape or size due to anesthesia or medication [8].

LDR treatment planning developed towards one-stage procedures or also called intra-operative planning techniques. Here, the acquisition of the image data, the treatment plan creation and the seed implantation are performed in one session inside the operating room [8, 13]. Compared to the two-stage procedure this entails improved dosimetry, reduced side effects, reduced cost [14]. Superior long term biological effects were shown in a study with more than 1000 patients and median follow-up time of 47 months by Matzkin *et al.* [15].

The American Brachytherapy Society distinguishes between three different intra-operative procedures [8, 16]. During intra-operative pre-planning the plan is created immediately before the implantation and executed without moving the TRUS or the patient. During interactive planning the same applies as before, but additionally the treatment plan is step-wisely refined depending on actual needle position. There are various possibilities on how often the dose distribution is recalculated, as there are many commercial systems available. Instead of utilizing the needles' position, the actual positions of the deposited seeds are considered in the dynamic dose calculation. Here, the dose distribution is updated continuously with each seed position feedback and changes in prostate shape and size can directly be taken into account [16]. The actual 3D seed positions can be obtained through fluoroscopic imaging or cone beam computed tomography (CBCT) [8].

Depending on the implemented process the team constantly needs to react to occurring circumstances such as a misplacement of the seeds, which can be time consuming. Therefore, costly time in the operating room may be extended [17]. Both fluoroscopic and CBCT imaging expose the patient to additional imaging dose [8]. This can be omitted by utilizing an interventional magnetic resonance imaging (iMRI) system for image guidance. These systems additionally offer better soft tissue contrast [18], but come with other challenges such as limited availability [19]. A paradigm shift is necessary in LDR brachytherapy treatment planning. This means converting static planning procedures, which only account for a fixed prostate geometry and come with the need for constant reaction, into simulation-based treatment planning considering the insertion process and the uncertainties of the system.

1.2.3 Simulations in medicine

Computer simulations are used in a wide range of applications in medicine. In simulation-based medical education in the field of radiation oncology screen-based simulators or virtual reality simulators including a haptic feedback allow to build confidence and competence

among trainees [20].

There are various examples where finite element (FE) simulations are used for structural analysis in a medical context such as an optimal hip implant design [21] or a stress analysis under different loads of the lumbar spine given an adolescent idiopathic scoliosis [22]. In cardiovascular engineering fluid-structure interaction models couple computational fluid dynamics and finite element analysis, in order to model this complex environment [23]. There are numerous studies which perform sometimes even patient specific simulations in order to investigate the effect of different influences [24, 25, 26], however high computational cost hinders the clinical application [27].

1.2.4 Simulations regarding needle insertion

Needles, as flexible medical devices are used for medical procedures such as brachytherapy, biopsy, or drug delivery [28]. The minimally invasive nature of using needles decreases the risk for infections and reduces the damage to healthy tissue, which results in fast patient recovery [29]. Accurate patient-specific needle insertion simulations can give insight into the procedure and assist in pre-operative planning by previously estimating needle placement deviations and tissue motion and such identify critical seed placements.

Alterovitz *et al.* [29] implemented a 2D dynamic FE simulation of a stiff needle being inserted into homogeneous linear elastic tissue. A sensitivity analysis regarding both patient-specific parameters such as tissue stiffness or compressibility, as well as physician-controlled parameters such as insertion depth and needle sharpness shows that the latter have a larger effect on the seed placement error. Chentanez *et al.* [30] developed a 3D FE tissue simulation with the needle modelled as a flexible 1D elastic rod. The tissue is represented in a tetrahedral mesh and the simulation is validated on phantom data. Goksel *et al.* [31] implemented a complete surgical setup including a tissue deformation simulation, seed placement, simulated TRUS for visual control, and dose calculation. This is a typical example of a training device which can improve surgical training. The meshes are generated with the meshing software VIMesh.

In all of the mentioned studies the simulations are either general analyses or use patient-specific data and are performed independent of an actual surgery. To be used in a clinical routine for either pre-interventional planning, planning inside the operating room, or for robot-assisted interventions the simulations need to be performed automated with as little necessary human interaction as possible.

The mesh generation is known to be a crucial step for numerical simulations [32, 33]. There are numerous tool such as Gmsh [34], Blender [35], or ANSYS® [36] available and

under constant development. These tools focus on engineering applications and therefore use CAD-constructed objects, while in the medical context the geometric information is often represented as labeled images [33]. Recent developments focus on the implementation of fully automated meshing tools from medical image segmentations such as Meshtool [33], MeshingNet [32], or vmtk [37]. Due to the fact that less human interaction is required in the mentioned automated tools, the mesh generation process can be speeded up, it requires less expert knowledge and avoids error-prone interactive manipulations.

All of the mentioned meshing techniques target complex geometries with boundary conforming meshes. Meshing of complex geometries can take up to a few minutes [34]. Opposed to boundary conforming meshing there is the possibility to embed the domain of interest in a larger, so-called fictitious or embedded domain, which is regularly meshed [38]. The structured meshes do not need to follow the complex tissue boundaries and therefore most of the challenging steps involved during meshing can be bypassed [39] and fast mesh generation can be guaranteed. The tissue distribution is modeled in a diffuse sense with a phase field smoothly transitioning from 0 outside of the domain to 1 inside the tissue domain [40]. This method is most suitable when the input data is available in a structured grid such as voxel data, as it is the case for medical images.

1.2.5 Dose variation due to seed misplacement

The clinical outcome, which is the tumor control and side effects in healthy tissue, depends among others on the dose deposited therein. In order for a physician to approve a treatment plan certain constraints or also called dose parameters have to be fulfilled by the dose distribution. More detailed information on dose parameters for LDR brachytherapy can be found in 2.2.2. Being able to predict deviations in seed placement and understanding that seed migration can be reduced, but not avoided, it is now important to quantify the resulting effect on the dose parameters.

One option which has been followed until now is to perform numerous simulations in a Monte Carlo-like manner, calculate dose distributions thereon and such statistically get an idea of the effect of seed misplacement on the actual RT treatment [41, 7, 42, 43]. Nath *et al.* [41] evaluate the effect of needle divergence on the coverage index and the homogeneity index of the dose distribution. The authors come to the conclusion that a needle tip displacement of less than 5 mm still provides sufficient coverage of the prostate. According to Dawson *et al.* [42], even small placement errors from the planned position can change the dose significantly. Taschereau *et al.* [7] use a seed misplacement model to understand deficiencies in treatment plans and consequently adapt the plans before application to the patient. They show that using simulations beforehand in order to make

the treatment plan more robust and less sensitive to seed misplacement increases the average post-implant V_{100}, which is the target volume receiving 100% of the prescribed dose. Thus, it becomes clear that understanding the sensitivity of a treatment plan with respect to seed misplacement and adapting it such that it is more robust has a direct effect on the outcome of the treatment.

Currently, there is no available measure to understand the effect on the resulting dose distribution and therefore the dose parameters of a mispositioned seed. In order to be clinically accepted, new techniques need to be capable of being integrated into existing treatment planning systems (TPS).

1.3 Goal of this work

As described above there are different LDR treatment planning procedures employed in different hospitals. What they have in common is that they are static procedures in which the definition of seed positions is based exclusively on a given patient geometry. Neither knowledge about the seed placement process nor a prediction of uncertainties in both the seed placement and the resulting dose distribution are considered in the planning. In contrast to this static planning, the long-term goal is to provide an uncertainty-aware planning, called simulation-based planning, that allows to develop a risk-robust treatment plan offline on one hand side. On the other hand side, during the intervention, it allows for optimal dynamic updates of the plan solving the tradeoff between new needle positioning and modified needle steering. Applications of this new class of treatment plans could be robotic interventions, where the robot navigates the needles through the tissue and where the risk-adapted plan allows for optimal trajectories and corrections.

In order to realize such an ambitious, disruptive planning strategy, this thesis lays the groundwork by establishing the necessary methods to conduct this plan. In particular, the thesis advances the state-of-the-art in a) the potential to assess the uncertainty for needle placement by allowing policy-based simulations to navigate the needle and to see the residual geometrical errors, and in b) to assess the locally induced dosimetric error as a function of seed misplacement.

First, an elastic simulation of the needle insertion with random disturbances can give an insight of an expected needle and such seed displacement. Therefore we develop a simulation of the tissue deformation during insertion of a flexible beveled tip needle, which can easily be adapted to patient-specific geometries without requiring multiple tools or engaging interactions. Since the needles are released by the medical doctor before the seeds

are inserted, remaining tension inside the tissue can relax and such change the position of both the tissue and the needle within. In order to get an accurate representation of the full process, a new model for the tissue relaxation is developed. This will enhance brachytherapy treatment planning by providing information about tissue motion and needle deflection during the procedure. Considering the development of needle insertion simulations mentioned in 1.2.4, we propose the diffuse domain method for needle insertion FE simulations [44, 45], which is an embedded domain method [38] omitting the need for boundary conforming meshes. Instead, the calculation is performed on a simple regular mesh, which allows for a less error-prone and fast mesh generation. Patient-specific tissue geometries are represented by probability maps from the tissue segmentation in the available voxel data.

As simulations only allow to predict the seeds' positions inside the tissue, there is a need to understand the effect of seed misplacement on the dose parameters. The second innovation of this work is to develop a method to bridge the gap between the local variation of the seed position and its effect on the dose distribution. Understanding the sensitivity of the resulting dose with respect to a misplacement of the seeds allows to create robust treatment plans with reduced need for treatment plan updating during the procedure. Performing multiple simulations including various dose calculations before each treatment is a time consuming task and only provides statistical information about placement tolerances. Instead, it is valuable to examine plan robustness immediately during plan creation and with information about individual seeds. We therefore develop a method to calculate the gradients of the dose parameters with respect to each seed position using automatic differentiation [46]. The gradients can then be related to placement tolerances, which gives a possibility to understand the sensitivity of a dose parameter with respect to the misplacement of every individual seed.

To summarize the implementation of the following methods is pursued:

- development of a patient-specific simulation of a flexible beveled-tip needle being inserted into inhomogeneous tissue without the need for meshing complex patient geometries, including a verification of the simulation method on a real-world phantom experiment
- development of a model for the needle-tissue-relaxation after the needle was released in order to depict the full LDR brachytherapy needle insertion process
- development of a method to calculate the sensitivity of dose parameters with respect

to seed placement and the subsequent definition of placement tolerances

After implementation the methods are published and the code will be made available online in order to be used for clinical verification and realization. The clinical verification will not be part of this thesis, but instead the focus is on the method development.

1.4 Structure of the thesis

In this work three peer-reviewed journal publications regarding simulation-based brachytherapy planning are collected in order to be submitted as a cumulative thesis. The author of this dissertation is the first author of all three journal articles.

The thesis is structured as follows: In chapter 2, fundamentals, a background on radiation therapy and brachytherapy is presented. The dose calculation used during treatment planning and the calculation of dose parameters are introduced. Three peer-reviewed journal publications are presented in chapter 3. For each publication a title page shows relevant publication information regarding the article, an embedding into the context of the thesis and its contribution to the state-of-the-art. In chapter 4 the findings are discussed in the context of simulation-based treatment planning, limitations are examined and the clinical relevance is evaluated. Finally, the work is summarized and a conclusion is drawn in chapter 5.

2 Fundamentals

In this chapter the physical background of using radiation for cancer treatment is presented. This is followed by an explanation of prostate brachytherapy and the associated treatment planning process with its included dose calculation and the calculation of dose parameters.

2.1 Radiation therapy

Among other treatment methods, such as surgical removal or chemotherapy, radiation is used for the treatment of cancer. According to the German cancer aid, RT is part of the treatment for 50 to 60% of all cancer patients. For 50% of the patients, which are considered to be permanently healed, RT was part of or even the single treatment option [47]. For various cancer types both surgery and RT result in the same probability of recovery. Since surgery has a higher probability of the organ's function loss, Radio-Chemotherapy, which is a combination of RT and Chemotherapy, is preferred [47]. One example is that a surgical removal of the laryngeal will inevitably result in the loss of a patient's voice, while a combined Radio-Chemotherapy can preserve the voice function during certain stages of the tumor [47].

The fact that ionizing radiation can be used to treat cancer is due to its interaction with tissue and the resulting biological effect.

2.1.1 Basics of radiation therapy

For RT cancer treatment ionizing radiation is utilized, which refers to radiation with sufficient energy to remove an orbital electron from an atom. The clinical application of RT focuses on various types of radiation such as high-energy photons, or particles like electrons, protons, neurons, or heavy ions such as carbon ion [48].

Interaction with matter Photons are absorbed inside the tissue due to three types of interactions, namely the photoelectric effect, Compton effect, and pair production. In low-energy regime of 10-25 keV the photoelectric effect is dominant. Here, the orbital electron fully absorbs the energy of the incoming photon and leaves the atom's orbit, as illustrated in Fig. 1a. The electron then ionizes surrounding molecules [49]. When the photon energy is larger (25 keV - 25 MeV) Compton scattering, which is incoherent scattering is the most dominant effect. In this energy regime, the incoming photon is not fully absorbed by the electron, but instead both the electron and the photon are scattered (see Fig. 1a). Despite the low resulting photon energy, the photon can undergo further interactions. The photon attenuation in water as a function of energy is shown

in Fig. 1b. It can be observed that for photon energies above 25 MeV pair production is most influential. Instead of interacting with the atom's electron, the photon interacts with the nucleus producing an electron and a positron, which both ionize the tissue. When the positron combines with a free electron, two photons are generated which interact further [49].

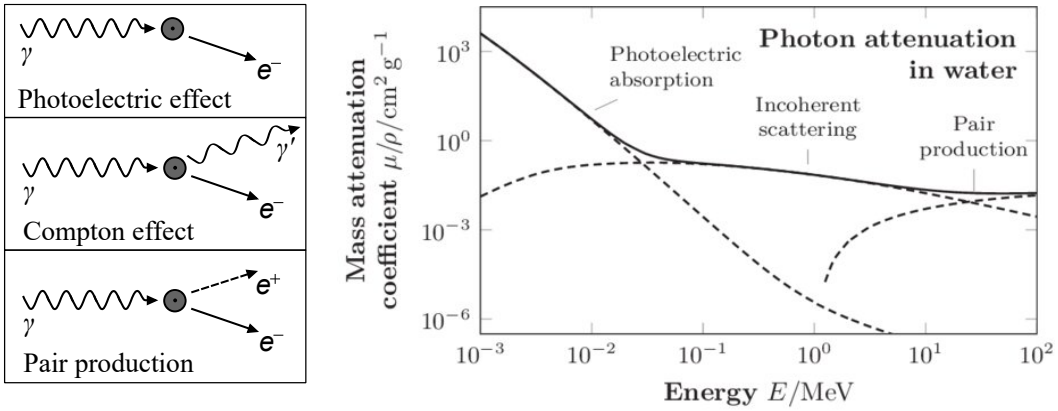

(a) Interaction types and products

(b) Photon attenuation in water for the different interactions depending on photon energy from [50]

Figure 1: Three types of photon-atom-interactions in radiation therapy

Biological effect The damage of the cell's deoxyribonucleic acid (DNA) is responsible for the biologic effects of the tissue. The radiation influences the DNA through either direct or indirection actions. During direct action, atoms of the DNA itself are ionized, leading to single- or double-strand breaks. When the radiation interacts with other atoms or molecules inside the cell it is called indirect action. When interacting with water molecules, hydroxyl ions are produced, which diffuse through the cell and can reach the DNA causing stand breaks [51, 48].

Through both direct and indirect action the radiation most often causes breaks of one of the two strands in the DNA. As one strand can easily be repaired by using the opposite strand as a template, this has only little biologic consequence. In so called double-strand breaks both strands are damaged opposite to one another breaking the chromatin into two pieces. This may result in cell killing, mutation or formation of cancer from normal cells [51].

2.1.2 Development of brachytherapy

The name brachytherapy is derived from the Greek term *brakhus* or *brachy* which can be translated to *short*. Compared to EBRT, where the radiation is applied from a distant

source, radioactive sources are placed into or very near the target. Today, the therapy is used for numerous malignancies among which are skin, cervical, uterine, breast, and prostate cancer. During LDR brachytherapy or also referred to as permanent implant brachytherapy radioactive sources are implanted into the target permanently. Both iodine seeds and beveled tip needles used for the application of the seeds are shown in Fig. 2. Contrary to LDR brachytherapy, higher activity sources are only temporarily positioned inside the target and removed when the desired dose has been delivered in high-dose-rate (HDR) brachytherapy [52].

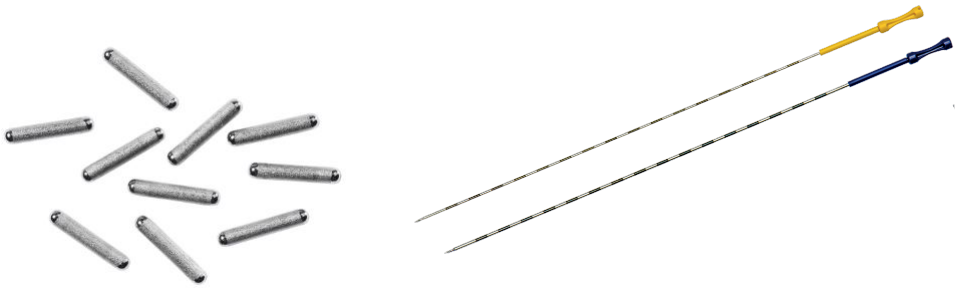

(a) (b)

Figure 2: I-125 seeds [53] (a) and needles [54] (b) for LDR brachytherapy adapted from Eckert&Ziegler

Pierre Curie invented brachytherapy in 1901 suggesting to insert a small radium tube into a tumor [55]. The application of radium to prostate cancer was first mentioned in 1914 by Pasteau and Degrais, and throughout the next decades it was reported that even though there is a response of the prostatic cancer to the radiation it cannot control the tumor. In 1972, iodine-125 (I-125) seeds were first retropubically implanted, setting the basis of modern brachytherapy. However, lacking appropriate imaging techniques the implantation was still performed blindly and the dosimetry only followed rough estimates [55]. The development of TRUS imaging opened the path to more effective and safer image-guided treatment in the 1980's [52, 3]. The calculation of a dose or dose rate at a given point combined with a medical image localizing the tumor in the patient's anatomy allows to understand whether the target is covered and if organs at risk (OARs) are spared. This can be implemented with modern resources and allows for patient-specific treatment planning [56]. Even though most of the concepts can also be applied to HDR brachytherapy, the focus of this work will be on LDR brachytherapy, because HDR monotherapy is less well established [4].

2.1.3 LDR prostate brachytherapy

According to the Groupe Européen de Curiethérapie and European Society for Radiotherapy and Oncology (GEC-ESTRO) guidelines [4] brachytherapy is an effective treatment when there is no evidence of metastases. For low and intermediate risk prostate cancer it can be used alone, while a combined therapy with EBRT is suggested for intermediate and high risk cancer in order to achieve a dose escalation.

During treatment the narcotized patient is placed in lithotomy position, i.e. on his back while the lower legs are supported such that the knees are above the hips and angled in 90 degrees. A template for needle guidance is positioned in front of the patient and connected to the TRUS probe as shown in Fig. 3. The template has an array of holes which are $5\,mm$ apart through which hollow needles are inserted using image guidance of the TRUS. The seed strands are then inserted through the needle and it is withdrawn from the patient leaving the seeds inside the tissue. The actual seed positions can be marked in the ultra sound (US) image and depending on the used treatment planning strategy the treatment plan is updated according to the seed deposition.

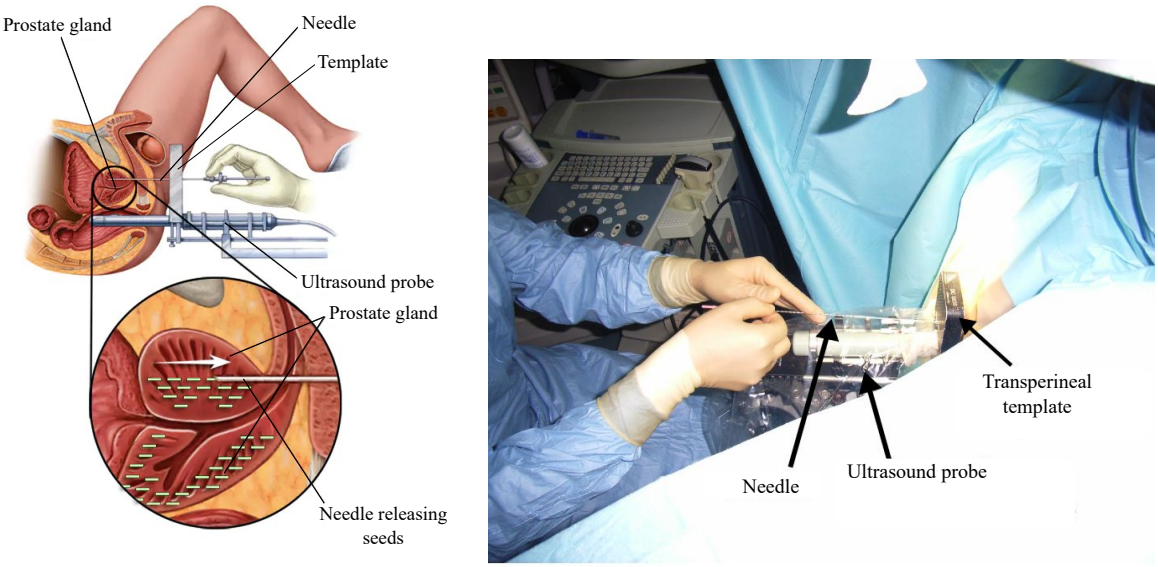

(a) (b)

Figure 3: Schematic (a) and real (b) setup of an LDR prostate brachytherapy. (a) is adapted from [57] and (b) is adapted from [58].

2.2 Treatment planning

In literature the term *treatment planning* is used in the context of prescription, dose calculation, optimization, and also clinical brachytherapy workflow strategies. In this work we refer to treatment planning as the full procedure including all steps involved in the radiation treatment after a corresponding prescription has been defined by the physician. In this section the general idea of a full treatment is explained, followed by a more detailed explanation of the most crucial steps and possible variations of the treatment procedure. The necessary steps to deliver an LDR prostate brachytherapy treatment are shown in Fig. 4. At first, 3D image data needs to be acquired on which different organs are contoured. The relevant organs for prostate brachytherapy are the prostate itself as the target region and both the urethra and the rectum, which are considered OARs. Afterwards a treatment plan, which is the definition of the aimed seed positions, is created manually or automatically with the treatment planning software. An exemplary treatment plan created with the VariSeed^{TM} LDR treatment planning system is presented in Fig. 5. When the desired seed positions are defined, hollow needles are inserted by the physician through which the seeds are then placed inside the tissue.

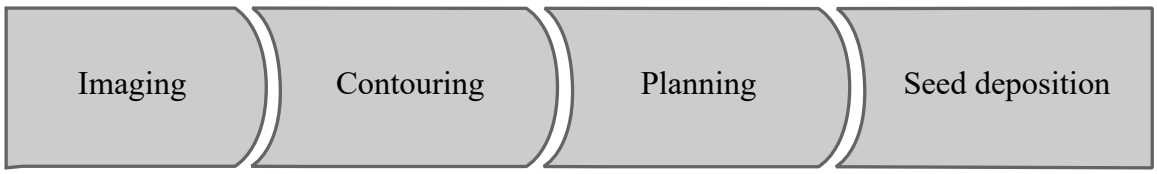

Figure 4: Flowchart of a general workflow during brachytherapy treatment planning

2.2.1 Dose calculation

In order to understand or optimize a treatment plan, the dose deposited to the tissue must be calculated. Most planning systems use the TG-43 or TG-43U1 formalism from the recommendations of the American Association of Physicists in Medicine (AAPM)[59, 60], according which the dose rate of a line-source is defined as

$$\dot{D}(r,\theta) = S_K \cdot \Lambda \cdot \frac{G_L(r,\theta)}{G_L(r_0,\theta_0)} \cdot g_L(r) \cdot F_L(r,\theta). \tag{1}$$

r is the distance from the source to the point of interest, r_0 is the reference distance of $1\,cm$, θ is the angle relative to the source's axis, and θ_0 is 90^o. S_K is the air-kerma strength,

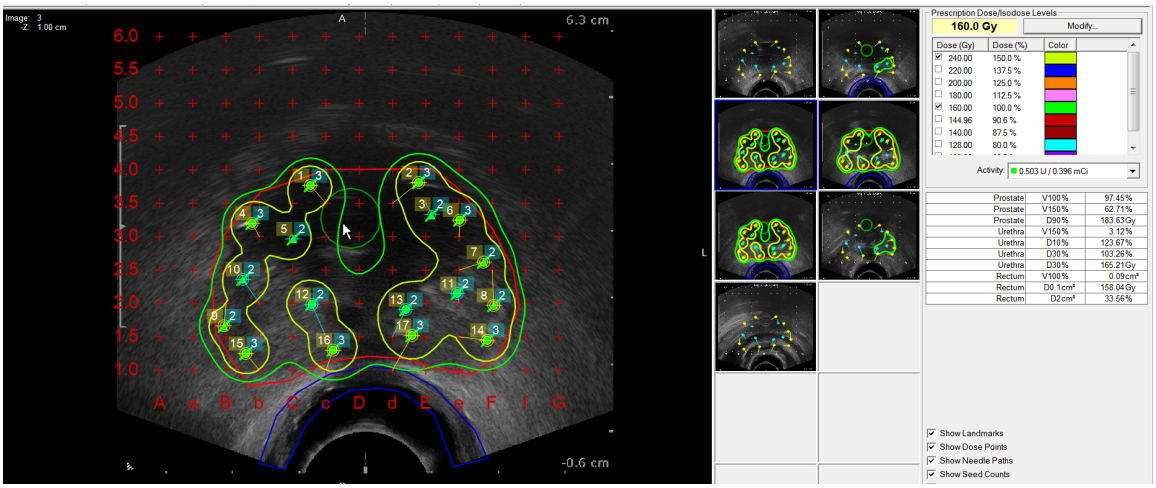

Figure 5: Prostate brachytherapy treatment plan created with the VariSeed^{TM} LDR treatment planning system version 9. In the main window the TRUS image is overlaid with a template grid (red). The tissue contours are shown in red (prostate), green (urethra), and blue (rectum) and the 160 Gy and 240 Gy isodose lines are visualized in green and yellow. The dose parameters on the right are shaded in red if the constraints are not fulfilled.

Λ is the dose-rate constant in water, G_L is the geometry function for a line source

$$\begin{aligned} G_L(r,\theta) &= \frac{\beta}{Lrsin\theta} && \text{if } \theta \neq 0^o \\ &= (r^2 - L^2/4)^{-1} && \text{if } \theta = 0^o, \end{aligned} \tag{2}$$

g_L is the radial dose function, and F_L is the 2D anisotropy function. The mentioned angles and coordinates are displayed in Fig. 6. Equation 1 is a 2D formalism treating the source as a line-source. There are various isotropic point-source approximations, from which the following is recommended [60] for the dose rate $\dot{D}$:

$$\dot{D}(r,\theta) = S_K \cdot \Lambda \cdot \frac{G_L(r,\theta_0)}{G_L(r_0,\theta_0)} \cdot g_L(r) \cdot \phi_{an}(r), \tag{3}$$

where ϕ_{an} is the 1D anisotropy function. Despite the fact that this is considered a 1D approximation, the line-source geometry function is deployed in order to improve the accuracy at small distances. A further explanation and varying definitions of those terms can be found in the TG-43 report [60]. Given this equation the dose at each point inside the tissue, which is treated as water equivalent, can be calculated from a single source.

For each possible seed position or also called dwell point x_j the dose at a certain voxel i can be calculated. This information is gathered in a so-called dose influence matrix a_{ij} from which the dose distribution $\boldsymbol{d}$ is calculated by the matrix vector product

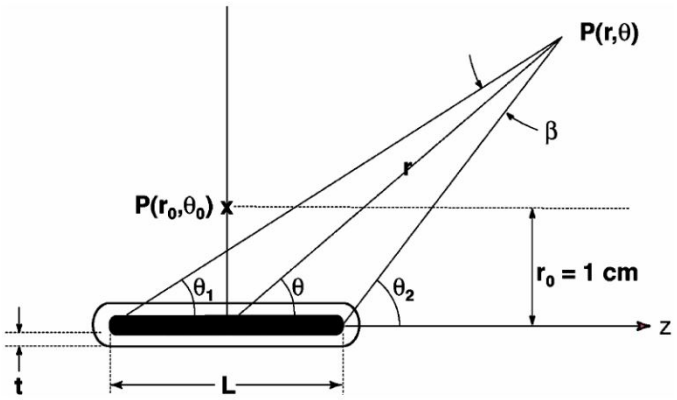

Figure 6: Coordinate system for dose calculation from [60]

$$\boldsymbol{d} = \boldsymbol{A}\boldsymbol{x}. \tag{4}$$

The length of the vector $\boldsymbol{d}$ is equal to the number of voxels. The seed configuration of all s possible dwell points is defined as a binary vector $\boldsymbol{x} = \{0, 1\}^s$ which is one for an occupied and zero for an unused seed position.

2.2.2 Dose parameters

From the calculated dose distribution and contoured imaging data cumulative dose volume histograms (DVHs) are generated. The horizontal axis shows the dose bins and the column height represents the relative organ volume which receives a dose greater or equal to the bin's dose. In a clinical routine bin sizes are chosen small, such that the DVH appears as a smooth line. From the DVH dose parameters are extracted. In LDR prostate brachytherapy dose parameters are e.g. the dose delivered to 90% of the prostate volume (D_{90}), the volume of the prostate receiving 100% of the prescribed dose (V_{100}), or the minimal dose of the $2\,cm^3$ most irradiated volume of the rectum (D_{2cc}) [61]. In order to achieve the wanted clinical outcome and avoid side affects, certain constraints on the dose parameters for both the target and the OARs are defined. Constraints for LDR brachytherapy can be found in the section *Methods and Materials* of publication III.

Either forward or inverse treatment planning (ITP) can be employed to find a seed configuration, which results in a dose distribution $\boldsymbol{d}$ close to the prescribed dose $\boldsymbol{\delta}$ and obeying all dose constraints. During ITP the problem is formulated as

$$\min\, f(\boldsymbol{\delta} - \boldsymbol{d}), \tag{5}$$

where the function $f(\cdot)$ measures the penalty associated with over- or underdosing the desired value $\boldsymbol{\delta}$ [62]. While for other radiation therapy treatments such as EBRT or HDR brachytherapy, the exposure times can have real valued numbers, the optimization becomes a binary integer programming problem for LDR brachytherapy due to the discrete nature of the treatment. It is a common practice to first create a generalized plan using ITP and then adapt it manually. Depending on the complexity of the patient's anatomy, it can acquire up to 30 minutes to create an acceptable plan [63].

3 Publications

In this chapter, the original articles concerning methods towards simulation-based brachytherapy treatment planning which are published by the author of this dissertation as a first author are printed in the original format and with kind permission of the copyright holders and publishers.

Publication I:
Needle Insertion Simulations of Stiff Needles

Title: Diffuse Domain Method for Needle Insertion Simulations

Authors: Katharina I. Jerg, René Phillip Austermühl, Karsten Roth, Jonas Große Sundrup, Guido Kanschat, Jürgen W. Hesser, Lisa Wittmayer

Journal: International Journal for Numerical Methods for Biomedical Engineering

DOI: 10.1002/cnm.3377

Thesis Context: The most obvious source of uncertainty in LDR prostate brachytherapy is that the radioactive seeds aren't deposited where they are supposed to due to inaccurate needle placement. A misplaced seed will alter the dose distribution, which may prevent the dose parameters from being achieved. This uncertainty can be estimated and addressed by modeling the insertion of needles into soft tissue as part of the treatment planning pipeline.

Contribution to state-of-the-art: State-of-the-art needle insertion simulation techniques require a mesh generation of the different tissues, which is an error prone process and often needs manual interaction. We therefore suggest to apply the diffuse domain approach to perform deformation simulations on a regular grid incorporating the tissue geometry by using probability maps directly from the tissue segmentation result. In this article we describe the method for inserting a stiff needle into elastic tissue, compare it against a simulation using a conforming mesh, present a pipeline how to automatically receive a deformation field based on the original voxel data, and apply it to an actual patient data set.

Received: 23 October 2019 | Revised: 7 May 2020 | Accepted: 27 May 2020
DOI: 10.1002/cnm.3377

RESEARCH ARTICLE - APPLICATION

WILEY

Diffuse domain method for needle insertion simulations

Katharina I. Jerg[1] | **René Phillip Austermühl**[1] | **Karsten Roth**[2] | **Jonas Große Sundrup**[3] | **Guido Kanschat**[4] | **Jürgen W. Hesser**[1] | **Lisa Wittmayer**[1]

[1]Mannheim Institue for Intelligent Systems in Medicine, Heidelberg University, Heidelberg, Germany

[2]Heidelberg Collaboratory for Image Processing (HCI), Heidelberg University, Heidelberg, Germany

[3]Institute of Computer Engineering (ZITI), Heidelberg University, Heidelberg, Germany

[4]Interdisciplinary Center for Scientific Computing (IWR), Heidelberg University, Heidelberg, Germany

Correspondence
Katharina I. Jerg, Mannheim Institue for Intelligent Systems in Medicine, Heidelberg University, Heidelberg, Germany.
Email: katharina.jerg@medma.uni-heidelberg.de

Funding information
German Research Foundation, Grant/Award Number: HE 3011/36-1

Abstract

We present a new strategy for needle insertion simulations without the necessity of meshing. A diffuse domain approach on a regular grid is applied to overcome the need for an explicit representation of organ boundaries. A phase field function captures the transition of tissue parameters and boundary conditions are imposed implicitly. Uncertainties of a volume segmentation are translated in the width of the phase field, an approach that is novel and overcomes the problem of defining an accurate segmentation boundary. We perform a convergence analysis of the diffuse elastic equation for decreasing phase field width, compare our results to deformation fields received from conforming mesh simulations and analyze the diffuse linear elastic equation for different widths of material interfaces. Then, the approach is applied to computed tomography data of a patient with liver tumors. A three-class U-Net is used to automatically generate tissue probability maps serving as phase field functions for the transition of elastic parameters between different tissues. The needle tissue interaction forces are approximated by the absolute gradient of a phase field function, which eliminates the need for explicit boundary parameterization and collision detection at the needle-tissue interface. The results show that the deformation field of the diffuse domain approach is comparable to the deformation of a conforming mesh simulation. Uncertainties of tissue boundaries are included in the model and the simulation can be directly performed on the automatically generated voxel-based probability maps. Thus, it is possible to perform easily implementable patient-specific elastomechanical simulations directly on voxel data.

KEYWORDS

diffuse domain, linear elastic equation, needle insertion, phase field, soft tissue

1 | INTRODUCTION

High dose rate (HDR) brachytherapy is a promising radiation therapy technique for inoperable primary and metastatic liver cancer.[1,2] In HDR, needles are used to place radioactive sources inside the tumor. Due to their steep dose fall-off, high therapeutic radiation doses are achieved inside the tumor while radiation sensitive healthy liver tissue is spared.[2] To ensure correct dose applications, an accurate needle placement is indispensable. Even though the needle placement can be monitored by computed tomography (CT), patient-specific and sufficiently realistic simulations can be applied

as part of the medical procedure planning.[3] An accurate tissue deformation simulation could allow simulation based treatment planning for brachytherapy. It has been shown that using computational simulators to learn surgical skills reduces the number of medical errors.[3] Needle insertion simulations are also a valuable tool for both surgical training and robot-assisted surgery.

In early publications, real-time tissue deformations were modeled with heuristic approaches, for example, mass-spring models[4] or the ChainMail algorithm.[5] Due to the fact that those models have unclear relationships between model parameters and material laws they were replaced by continuum-based procedures, which make use of constitutive laws to model the mechanical behavior of soft tissue.[6] Physical balance laws are used to determine the field variables in the domain. The finite element method (FEM) is a mesh-based approach where the domain of interest is divided into elementary building blocks on which the constitutive laws are approximated. Since large systems of equations are solved, the physical accuracy is achieved with high computational effort. Due to the complex geometry of organs, boundary-conforming mesh generation is often a complex task[6] and therefore time consuming and expensive.

In order to avoid volume meshing, so called fictitious or embedded domain methods were introduced.[7] The general idea is to embed the domain of interest in a larger regular domain. Embedded domain methods can differ in the representation of the boundary, the integration, and in the way boundary conditions are imposed. For needle insertion simulations, the corotational cutFEM[8] has been used. In the cutFEM method, cells are classified into three types: inside elements which are fully contained in the domain of interest, outside elements in which the domain of interest is not included, and cut elements containing the surface. For integration, the cut elements are split into elements which are conforming with the surface. Even though the solution is only approximated on a coarse mesh, there is a need of a discrete boundary parameterization.

Given discrete imaging modalities, like CT, it is desirable to use voxel-based models where each voxel or a group of voxels is associated with one hexahedral element. The voxel finite cell method, which uses higher order ansatz polynomials, has been used for linear elastic bone simulations from CT data.[9,10] The material stiffness at each quadrature point is derived from the Hounsfield Unit while quadrature points outside the bone are assigned to zero stiffness. Phase field[7] or also called diffuse domain methods allow finite element (FE) simulations without explicit boundary parameterization. Phase field methods have been applied to advection-diffusion problems,[11,12] crack simulations,[13,14] and prostate cancer growth.[15] Instead of applying boundary conditions on a sharp boundary, a smooth phase field function is defined transitioning from 0 outside to 1 inside the domain. This function and its gradient are used to reformulate surface terms into additional volumetric terms and thus eliminate the need for an explicit boundary parameterization.

The contribution of this paper is an elastic simulation using the example of a needle insertion on a voxel basis and without the need of meshing or explicit boundary parameterization. This automated method allows for easily implementable patient-specific simulations directly on voxel data. The phase field approximation is used to model the transition of elastic parameters at tissue boundaries inside the target volume. In a segmentation, where each voxel is defined inside or outside of a volume of interest, the boundary has a stair-like shape, which certainly does not represent the actual organ surface. Generating surface meshes still only defines an arbitrary tissue boundary obtained from geometric considerations rather than the actual data. In our approach, the shape of the organs is not directly represented by separate meshes, but indirectly by a smooth transition of elastic parameters from one region to another. The simulation can be directly computed on a regular grid without the need for meshing complex geometries. Boundary conditions between different organs do not need to be explicitly parameterized. To transfer the uncertainty of the model geometry from the segmentation into the diffuse width of the phase field is a heuristic assumption which offers great potential for a simple workflow from voxel images to a phase field and thus a simulation of a displacement field. Another challenging task is to describe the interaction between the needle and the tissue for which the phase field approach offers a simple solution. Friction forces are applied as traction forces to the tissue. These traction boundary conditions are approximated by the absolute gradient of a phase field function and are thus transformed into easily implementable volumetric terms in the differential equation.

This paper is organized as follows: The material and methods are introduced in Section 2. In Section 3, we present our results, which are discussed in Section 4. A conclusion is drawn in Section 5.

2 | MATERIAL AND METHODS

First, we introduce the embedded domain approach and explain how to avoid explicit coding of surfaces. This is followed by the elastic equation, which describes the response of the tissue. We then explain the strategy for two

validation experiments. The final setup and a three-class U-Net, which serves as automated tissue phase field extraction, are then explained. In the tissue phase field, the uncertainties arising from the segmentation procedure describe the transition of tissue parameters at the tissue boundary.

2.1 | Embedded domain and phase field approximation

In order to avoid meshing of complex geometries, the considered domain Ω is embedded in a larger fictitious domain Ω_0.[7] The Heaviside step function H

$$H(x) = \begin{cases} 1 & \forall x \in \Omega \\ 0 & \text{otherwise} \end{cases} \tag{1}$$

represents a sharp boundary to distinguish between the inside and the outside of the physical domain. A phase field function ϕ is defined as an approximation to the step function to represent a diffuse boundary as illustrated in Figure 1. The volume integral over a function $\boldsymbol{Q}$ can be written as[16-18]

$$\int_{\Omega} Q d\Omega = \int_{\Omega_0} QH d\Omega_0 \approx \int_{\Omega_0} Q\phi d\Omega_0. \tag{2}$$

In order to consider the boundary conditions on a surface Γ, the Dirac distribution δ_Γ is approximated by the absolute gradient of the phase field function. A diffuse boundary integral of a function $\boldsymbol{h}$ over a boundary Γ is modeled as follows[16,18]:

$$\int_{\Gamma} h d\Gamma = \int_{\Omega_0} h\delta_\Gamma d\Omega \approx \int_{\Omega_0} h \mid \nabla\phi \mid d\Omega. \tag{3}$$

The phase field function ϕ is chosen as[16]

$$\phi(\boldsymbol{x}) = \frac{1}{2}\left(1 - \tanh\left(\frac{3r(\boldsymbol{x})}{\epsilon}\right)\right), \ \boldsymbol{x} \in \Omega_0 \tag{4}$$

where $r(\boldsymbol{x})$ is a signed distance function representing the boundary Γ which is defined negative inside and positive outside of Ω. In the Appendix, we show that the normalization of the absolute gradient of the given phase field function is 1 and can therefore be used to approximate the delta function in the sense that the volume integral approximates the surface integral.

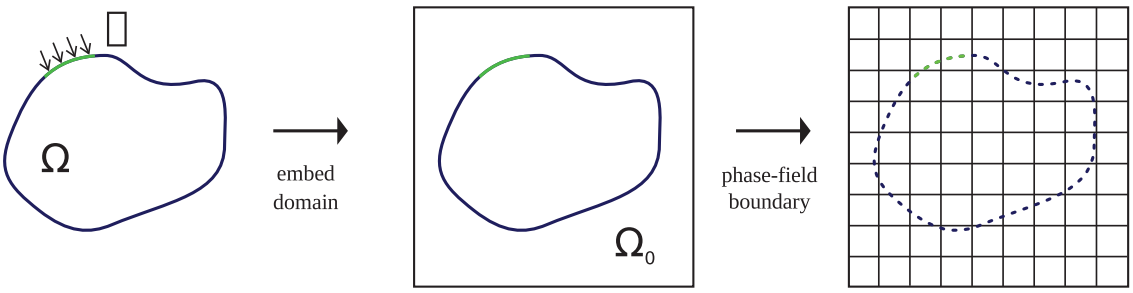

FIGURE 1 A physical domain Ω with boundary conditions on Γ is embedded in a larger domain Ω_0. Ω_0 is regularly meshed and the sharp boundary is approximated by a smooth phase field function ϕ

2.2 | Tissue model

During needle insertion, the tissue is modeled as linear elastic deformable object. Since dynamical effects such as inertia are contributing only a little due to the gradual insertion of the needle into the tissue, we simplify the model so that the tissue and the external forces are in equilibrium at all times yielding a quasi-static approximation

$$\delta W(\boldsymbol{u},\delta\boldsymbol{u}) = \int_{\Omega} (\boldsymbol{\sigma} : \delta\boldsymbol{\epsilon} - \boldsymbol{b}\cdot\delta\boldsymbol{u})\, d\Omega - \int_{\Gamma} \boldsymbol{t}\cdot\delta\boldsymbol{u}\, d\Gamma = 0. \tag{5}$$

The derivation of the variational formulation follows,[19] where δW is the virtual work, $\delta\boldsymbol{u}$ are the virtual displacements, $\boldsymbol{\sigma}$ is the stress tensor, $\delta\boldsymbol{\epsilon} = 1/2(\nabla\delta\boldsymbol{u} + \nabla\delta\boldsymbol{u}^T)$ is the virtual strain tensor, $\boldsymbol{b}$ is the body force (eg, gravity), and $\boldsymbol{t}$ denotes the traction force. Traction boundary conditions are applied on the boundary Γ and displacement boundary conditions $\boldsymbol{u} = \boldsymbol{u}^D$ are applied on Γ_D. The given formulation includes volume integrals over the physical domain Ω and a surface integral over a sharp boundary Γ. With Equations 2 and 3 the integrals can be extended to the embedding domain Ω_0, which results in the following diffuse variational formulation:

$$\delta W(\boldsymbol{u},\delta\boldsymbol{u}) \approx \int_{\Omega_0} (\boldsymbol{\sigma} : \delta\boldsymbol{\epsilon} - \boldsymbol{b}\cdot\delta\boldsymbol{u})\,\phi\, d\Omega_0 - \int_{\Omega_0} \boldsymbol{t}\cdot\delta\boldsymbol{u}\,|\,\nabla\phi\,|\, d\Omega_0 \approx 0. \tag{6}$$

In the case of an isotropic linear elastic material, the stress tensor only depends on the two Lamé parameters λ and μ. With the Einstein notation the stress tensor can be written as[20]

$$\sigma_{ij} = \lambda\delta_{ij}\epsilon_{kk} + 2\mu\epsilon_{ij}. \tag{7}$$

This leads to the respective bilinear form

$$\int_{\Omega_0} \left(\lambda\partial_i u_i \partial_j \delta u_j + \mu\partial_i u_j \partial_i \delta u_j + \mu\partial_j u_i \partial_i \delta u_j - b_i \delta u_i\right)\phi\, d\Omega_0 = \int_{\Omega_0} t_i \delta u_i\,|\,\nabla\phi\,|\, d\Omega_0. \tag{8}$$

(See Appendix for more details.) The partial derivative with respect to the $\boldsymbol{i}$-th component is denoted by ∂_i.

Equation 8 has been implemented with using the C++ finite element library deal.II.[21] The domain is discretized in a hexahedral mesh and for each space dimension linear Lagrange finite elements are used. For three spatial dimensions and eight support points in a hexahedral cell, there are 24° of freedom per cell. A tensor product of three one-dimensional two-point Gauss-Legendre quadrature formulas is used to allow for an optimal approximation during numerical integration.

In engineering, linear elastic materials are often described by the elastic modulus or also called Young's modulus $\boldsymbol{E}$ and + Poisson's ratio ν. The Lamé parameters are determined by[20]

$$\mu = \frac{E}{2(1+\nu)} \quad \lambda = \frac{\nu E}{(1+\nu)(1-2\nu)}. \tag{9}$$

The elastic properties are expressed as Young's modulus and Poisson's ratio in the following.

Studies on the mechanical properties of liver tissue[22,23] show that viscoelastic or other non-linear material laws better describe the mechanical response of liver tissue. However, in measurements the shear modulus μ of the liver has a SD of 10% between 11 healthy volunteers.[24] These uncertainties introduce errors which are currently larger than those from the approximation by a linear model. Yet, the diffuse variational formulation (Equation 6) can be easily extended to more complex tissue models.

2.3 | Validation of the diffuse domain approach

Two preliminary experiments are performed. First, a needle inserted into homogeneous tissue is simulated where the needle forces to the tissue are applied as boundary conditions through the absolute gradient of the phase field

function (Equation 8, right hand side). For this experiment, the convergence of the deformation error is analyzed and it is compared to a conforming mesh simulation with the same setup to confirm the deformation field of the tissue. Secondly, a simulation of a cube containing a tissue boundary is performed to show convergence for inhomogeneous materials, where elastic parameters transition from one region to another. Both experiments are described in the following.

2.3.1 | Needle insertion into homogeneous tissue

Diffuse needle model

The needle is modeled as a stiff cylinder with a hemispherical tip. This is a model for a rigid needle, which is much stiffer than the tissue and cannot be deformed by the interaction. Friction forces are applied as traction forces $\boldsymbol{t}$ to the tissue at the needle boundary into the direction of motion. The physical domain Ω of the tissue corresponds to the full integration domain Ω_0 without the volume occupied by the needle. The phase field function ϕ transitioning from 1 inside the physical domain to 0 outside is shown for two dimensions in Figure 2A). The traction forces are approximated via the absolute gradient of the phase field $|\nabla \phi|$ illustrated in Figure 2B). An intersection of the phase field function ϕ and its absolute gradient $|\nabla \phi|$ for different interface widths ϵ is shown in Figure 3.

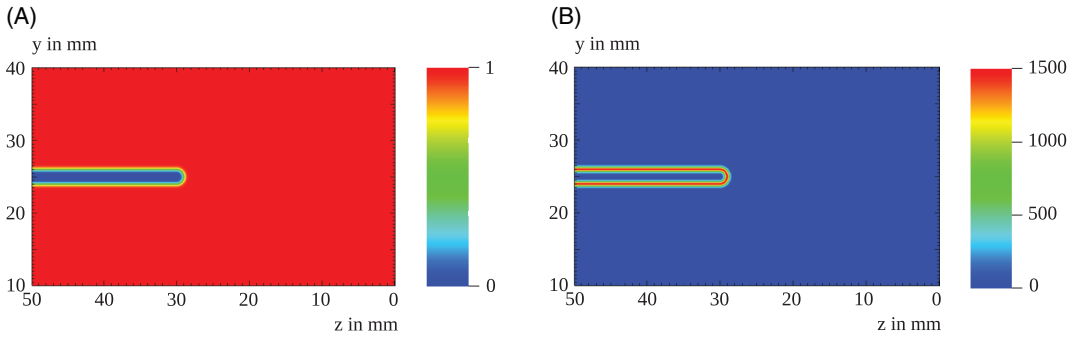

FIGURE 2 Phase field representation of the tissue after a needle with a typical diameter of 2 mm was inserted 20 mm into the tissue. The phase field function ϕ in (A) transitions from zero outside the tissue domain to one inside the tissue. (B) shows the tissue boundary, which is approximated by the absolute gradient of the phase field function $|\nabla \phi|$. The phase field width ϵ is 1 mm

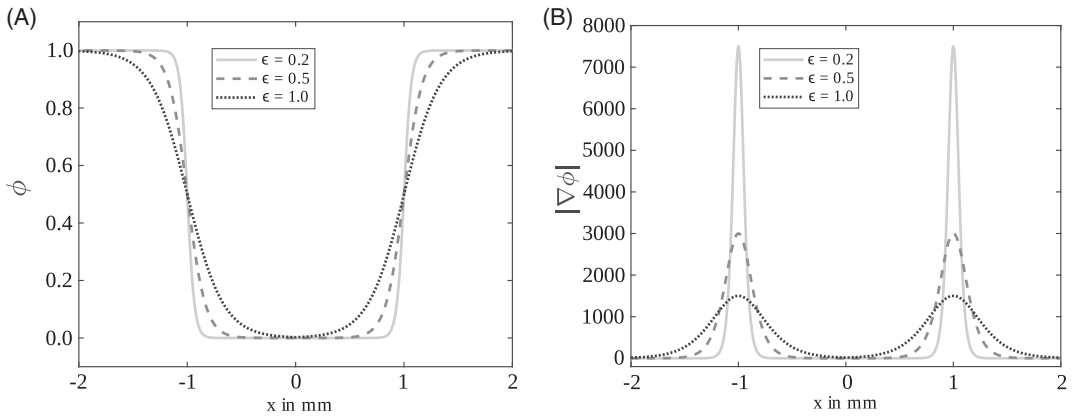

FIGURE 3 (A) phase field ϕ and (B) absolute gradient of the phase field $|\nabla \phi|$ as a function of the distance from the needle center for different phase field widths ϵ. The needle diameter is 2 mm

Convergence analysis a for decreasing needle phase field width

The convergence of the diffuse domain method has been studied for different approximations of the boundary conditions.[16,25]The interested reader is referred to[16,25] and the references therein. In order to verify the functionality of our implementation, the convergence of the error of the phase field approximation for the needle boundary's Dirac δ was analyzed for decreasing ϵ. Since there is no analytical solution to the problem, the order of convergence $\boldsymbol{p}$ was determined using Equation 10 for a decreasing phase field width.[26]

$$\frac{|d_\epsilon - d_{\alpha\epsilon}|}{|d_{\alpha\epsilon} - d_{\alpha^2\epsilon}|} = \alpha^{-p} + O(\epsilon) \tag{10}$$

d_ϵ is the displacement field resulting from a deformation simulation with phase field width ϵ after the needle was inserted 20 mm into the tissue. $|\cdot|$ is the L2-norm of the vector field integrated over the physical domain. To avoid large computation times, the needle diameter was set to 5 mm and only a quarter of the grid was simulated for this experiment. Due to symmetry, the full grid with a total size of 30 mm × 30 mm × 50 mm was split along the needle shaft into a new grid size of 15 mm × 15 mm × 50 mm. The cell size of the hexahedral grid is 0.23 mm × 0.23 mm × 0.78 mm. In order to focus on the error of the phase field width and ignore discretization errors, the cell size is kept constant. To be able to resolve the phase field with the given quadrature formula, $\varepsilon = 1$ mm was chosen as the lower limit for the phase field width. The diameter of the needle determines the upper limit for the phase field width to avoid interference of the two boundaries. The factor α by which ϵ is reduced was chosen to be 1/1.2 to ensure multiple data points within these limits.

Comparison to the conforming mesh simulation

To evaluate the performance of the tissue deformation with a phase field approximation, the result is compared to a quasi-static conforming mesh simulation performed with ANSYS 2019. This is a commercial software being used for medical and hospital supplies and thus representing the gold standard. The needle with a diameter of $d = 2$ mm and the tissue are each represented by separate meshes (see Figure 4). Cutting of meshes is a complex task and not possible with a quasi-static model. In order to neglect cutting effects, a hole is introduced into the tissue for the defined needle path. Thus, only friction forces between the needle and the tissue are considered. The needle is considered to be made of stainless steel with an elastic modulus $E_N = 193$ GPa. The linear elastic tissue model has an elastic modulus $E_T = 3$ kPa and a Poisson ratio $\nu = 0.3$. Due to symmetry, only half of the space is simulated.

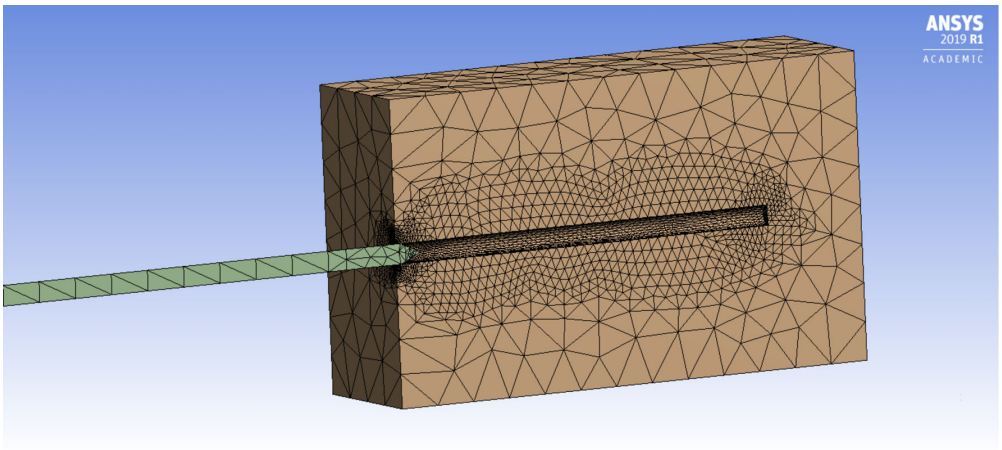

FIGURE 4 ANSYS simulation using a tetrahedral conforming mesh for both the needle and the tissue. A hole is introduced into the tissue to avoid cutting effects

2.3.2 | Diffuse tissue boundary

To verify the diffuse domain approach for tissue boundaries in inhomogeneous tissues, a small numerical example of a cube with two tissue types is analyzed. The cube with an edge length of 20 mm and a resolution of 1 mm × 1 mm × 1 mm consists of tissue$_1$ for $z \leq 10$ mm and tissue$_2$ for $z > 10$ mm (see Figure 5). The tissues differ in Young's modulus $E_1 = 2.6$ kPa and $E_2 = 5.2$ kPa, which are typical values for liver tissue.[24] The boundary at $z = 0$ mm is set to zero-displacement boundary conditions and a unit body force in negative z-direction is applied to the tissue. In order to model a diffuse transition between the different tissues, the volume is smeared out with 3D Gaussian filters with three different standard deviations $\sigma_1 = 0.5$ mm, $\sigma_2 = 1.0$ mm, and $\sigma_3 = 3.0$ mm. The displacement is analyzed at a reference point on the surface by subsequently refining the mesh.

2.4 | Needle insertion into liver tissue

The introduced diffuse domain method is now applied to liver data from a CT scan. A needle with 3 mm in diameter, as explained in Section 2.3.1, is inserted into the tissue. For the scope of this work, three tissue types are considered:

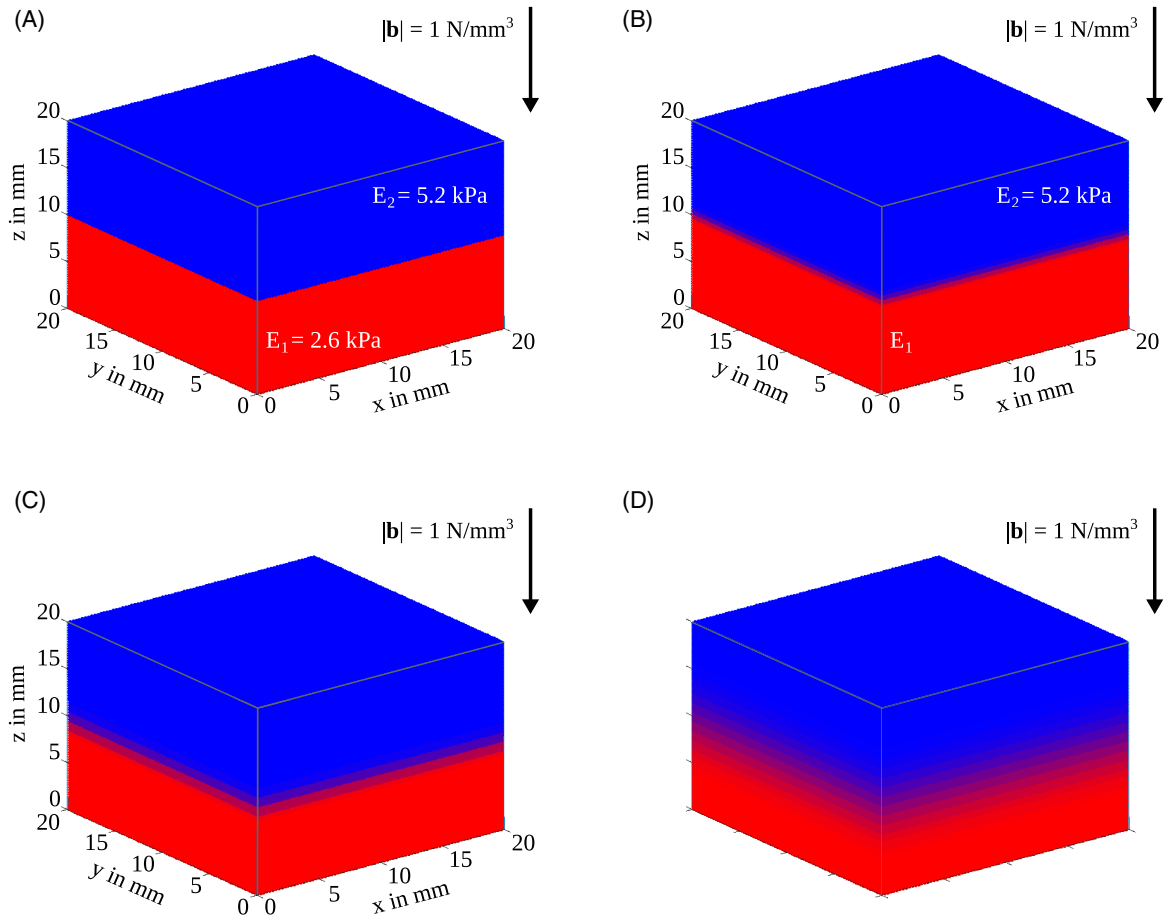

FIGURE 5 Cube with tissue$_1$ (red) and tissue$_2$ (blue). Zero-displacement boundary conditions are applied to the bottom surface at $z = 0$ and a constant body force $\boldsymbol{b} = [0\ \text{N/mm}^3, 0\ \text{N/mm}^3, -1\ \text{N/mm}^3]$ is applied to the tissue. In order to get a diffuse tissue boundary, the (A) sharp tissue boundary is filtered with Gaussian filters with SD (B) $\sigma = 0.5$ mm, (C) $\sigma = 1.0$ mm, and (D) $\sigma = 3.0$ mm

tumor tissue (E_t = 2 kPa), liver tissue (E_l = 3 kPa), and a stiff surrounding tissue (E_s = 4 kPa) in which the liver is embedded. Instead of building mesh models of those complex shapes, the underlying tissue distribution is obtained directly from the CT image. The workflow of the automated deformation simulation is illustrated in Figure 6. Tissue probability maps, which have a probability value between 0 and 1 for each tissue type in every voxel, are created with an inhouse developed deep fully-convolutional neural network. Of course other segmentation methods could be used instead. Due to the discretization of the domain into 1 mm × 1 mm × 1 mm voxels, there are segmentation uncertainties in voxels at the boundary between different tissues. This is expressed by probability values of for example, 0.3 and 0.7 for two different tissue types reflecting the uncertainty of a specific tissue in the given voxel. The probability maps are used as phase field functions in the numerical simulation from which the deformation field is obtained.

2.4.1 | Patient data

CT scans from the Liver Tumor Segmentation Dataset (LiTS)[27] were utilized to train a segmenting deep convolutional neural network and thus to obtain tissue probability maps of a human liver, a tumor and the surrounding tissue. The scans were acquired from different clinical sites and contain instances of primary (eg, hepatocellular carcinoma) and secondary tumor diseases/metastasis derived from colorectal, breast and lung cancer. In total, 131 volumes are present, divided into 105 training and 26 validation volumes. For training the neural network the data set contains manually labeled segmentation masks, defining the tissue type for each voxel. Here, the phase field method is demonstrated on one sample volume from the validation set to emphasize the applicability in concurrence with automated segmentation methods.

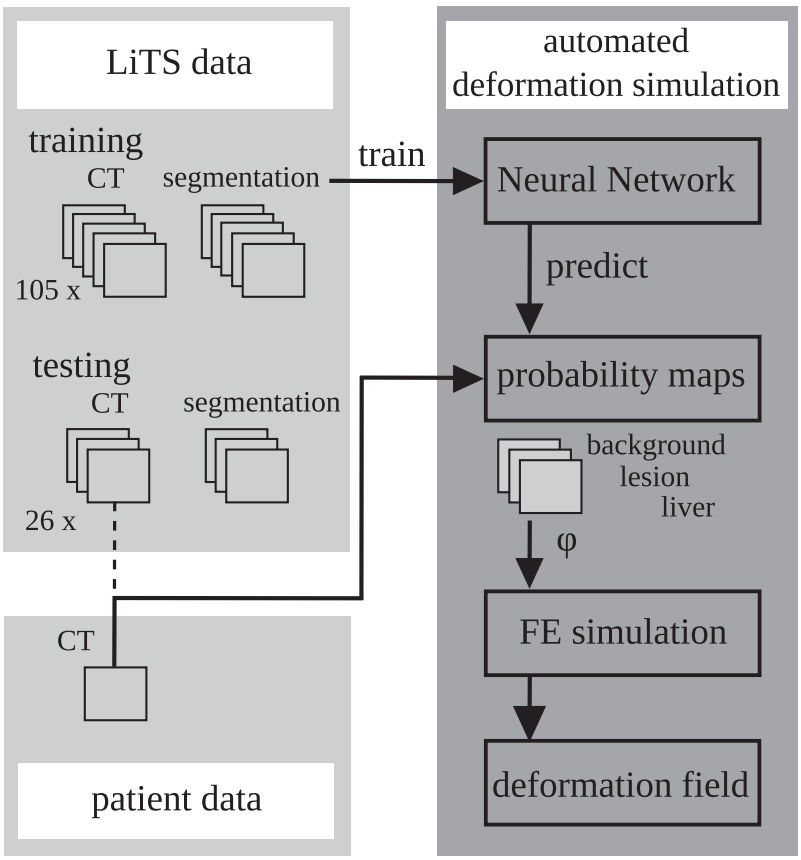

FIGURE 6 Workflow of the automated tissue deformation simulation from CT data. A neural network is trained on 105 training CT data sets with manually labeled segmentation masks. Probability maps of the liver, the lesion, and the background are predicted from the CT data of interest. For demonstration, we use one of the 26 test data sets. The probability maps serve as phase field functions ϕ for the diffuse domain FE simulation from which the deformation field is obtained

2.4.2 | From CT data to the diffuse tissue representation

In a voxel representation of a tissue as obtained from medical imaging devices, there are no clearly defined boundaries. A diffuse representation of the boundary therefore accounts for the uncertainties in the imaging data. Recently, fully automated liver and tumor segmentation methods based on deep fully-convolutional neural networks have shown promising segmentation performances.[28-31] However, these methods are of cascaded nature, meaning liver and lesions are segmented in succession. For our experiments, probability maps of liver, lesion, and background are required. Hence, we train a 2D three-class U-Net[32] with softmax output to obtain probability maps for each CT slice. Our architecture additionally makes use of residual connections,[33] batch-normalization[34] and dilated convolutions[35] in axial direction. The network is trained on 50 full, but randomized iterations over all aforementioned 105 training volumes. The Adam optimizer[36] is used with a learning rate of $3 \cdot 10^{-5}$ and a mini-batch size of 32. Our loss function is a combination of two functions. The first function is a smooth, multiclass Dice score function[37]

$$D(T,Y) = -\frac{1}{c}\sum_{k}^{c}\frac{2\sum_{i,j}^{H,W} T_{k,i,j}Y_{k,i,j}}{\sum_{i,j}^{H,W} T_{k,i,j} + \sum_{i,j}^{H,W} Y_{k,i,j} + \epsilon} \tag{11}$$

with width $\boldsymbol{W}$ and height $\boldsymbol{H}$ of the ground truth target slice $\boldsymbol{T}$ and network output $\boldsymbol{Y}$. $c = 3$ and $\epsilon = 10^{-5}$ denote the number of classes and a small addition to the denominator to avoid division by zero, respectively. The second function is a pixel weighted cross entropy loss

$$P(T,Y) = -\frac{1}{HWc}\sum_{k,i,j}^{c,H,W} \beta_{i,j} \cdot T_{k,i,j} \log Y_{k,i,j}. \tag{12}$$

The pixel weights $\beta_{i,j}$ are taken from precomputed distance-based weight maps, similar to Reference 32. However, Ronneberger et al[32] place high weights on inter-boundary pixels, whereas our approach highlights pixels generally close to liver or lesion border, both inside and outside the boundary. This ensures more accurate segmentation along these edges. The overall loss function takes the form

$$L(T,Y) = \frac{P(T,Y)}{D(T,Y) + \epsilon}. \tag{13}$$

In early training stages, a low dice score generates a strong learning signal. In later, saturated training stages, the cross entropy function comes into play, putting high emphasis on correct boundary pixel classification.

3 | RESULTS

3.1 | Needle insertion into homogeneous tissue

3.1.1 | Convergence analysis for decreasing needle phase field width

The convergence study shows a convergence of the solution error for decreasing interface width. The relative displacement error over the full domain compared to the displacement field with $\varepsilon = 1.005$ mm is shown in Figure 7. In Table 1, the order of convergence $\boldsymbol{p}$ is shown for different phase field widths. The average rate of convergence over the given range is 1.97 ± 0.23.

3.1.2 | Comparison to conforming mesh simulation

In the conforming mesh simulation performed with ANSYS, separate meshes for the needle and the tissue were generated (compare Figure 4) and the needle was inserted 20 mm into the tissue. The magnitude of the final displacement

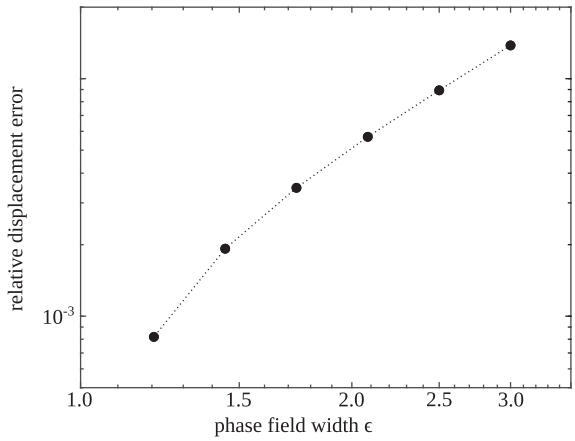

FIGURE 7 Relative displacement error compared to the simulation with the smallest simulated $\epsilon = 1.005$ mm

ϵ in mm	$\boldsymbol{p} = \log_{1.2}\left(\frac{\lvert \boldsymbol{d}_{\epsilon} - \boldsymbol{d}_{ue} \rvert}{\lvert \boldsymbol{d}_{ue} - \boldsymbol{d}_{\alpha 2_{\epsilon}} \rvert}\right)$
3.000	2.26
2.500	2.09
2.083	1.98
1.736	1.85
1.447	1.65

TABLE 1 The order of convergence $\boldsymbol{p}$ computed with Equation 10 for decreasing phase field width ϵ. To ensure multiple data points within the limits defined by grid size and needle diameter α is chosen to be 1/1.2

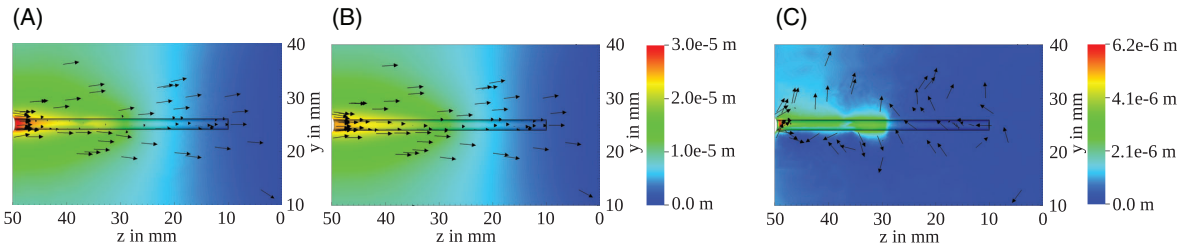

FIGURE 8 Deformation magnitude and direction (black arrows) of the soft tissue for (A) mesh based and (B) embedded domain needle insertion simulation. The deformation field of the embedded domain method is interpolated to the grid of the mesh based simulation. (C) shows the difference between the two simulations

field within the tissue is illustrated in Figure 8A. In order to compare the results, the corresponding phase field simulation with a phase field width of 1 mm was interpolated to the tetrahedra mesh of the ANSYS simulation (see Figure 8B). To ensure that no invalid solution values on nodes outside of the physical domain are used for the interpolation, the needle diameter for the phase field function ϕ was reduced to 1.5 mm. The force coefficient of the phase field simulation was scaled to minimize the weighted sum of the difference between the two deformation fields. This resulted in a relative displacement error of 7.1% over the given domain. The difference between the deformation fields is shown in Figure 8C. The deformation component parallel to the needle agrees well, while the perpendicular components are not captured by the embedded domain simulation. In the proximity of the entry point of the needle, the largest differences between the two simulations occur. Since the region of interest (eg, the liver) is embedded in a larger domain, the deformation at the entry point is not of interest. It must be mentioned that despite the symmetry of the problem, the deformation result of the conforming mesh simulation is not symmetric around the needle shaft. The symmetry of the problem is not correctly reproduced with the tetrahedral ANSYS mesh, which leads to errors in the simulation. This is an indication of potential problems arising when generating boundary conforming meshes.

3.2 | Diffuse tissue boundary

The linear elastic equation with a diffuse tissue boundary is analyzed using the example of a small cube (for setup compare Figure 5). A unit force in negative z-direction is applied to the body while there are zero Dirichlet displacement boundary conditions at $z = 0.0$ mm. In Figure 9, the deformation in z-direction at a typical point $P = [10.0\ \text{mm}, 10.0\ \text{mm}, 20.0\ \text{mm}]$ in the cube is shown for different refinements of the grid. For a phase field width of 3.0 mm, the z-displacement is underestimated by 2% compared to a phase field width of 0.5 mm.

3.3 | From CT data to diffuse tissue representation

3D probability maps are generated with the three-class U-Net from the CT data. For our experiments we use the LiTS-data set volume no. 88 from the validation data set. In Figure 10, one slice of the 3D probability maps for each the liver, the tumors and the surrounding tissue are presented. The resulting binary segmentations from these maps achieve a dice score of 94 for the liver and 62 for the tumor in comparison to the manually labeled ground truth segmentations. The position of the given slice within the liver is illustrated in Figure 11. Here, the diffuse liver boundary can be seen in a close up view. The probability maps are the most accurate information which can be obtained from the images. The

FIGURE 9 Absolute displacement in z-direction of a typical point $P = (10\ \text{mm}, 10\ \text{mm}, 20\ \text{mm})$ in the tissue as a function of the grid refinement. The interface width of the diffuse boundary is varied through filtering the volume with a 3D Gaussian filter with different standard deviations σ

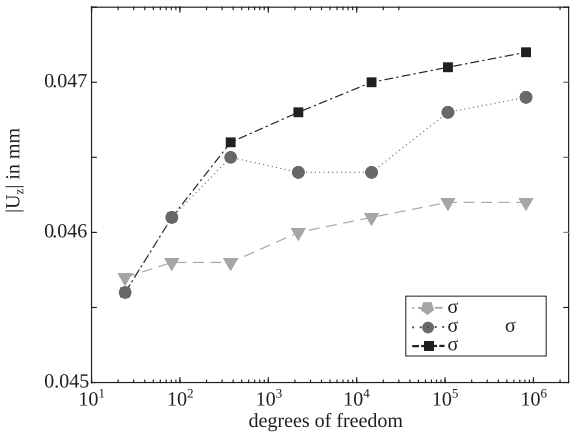

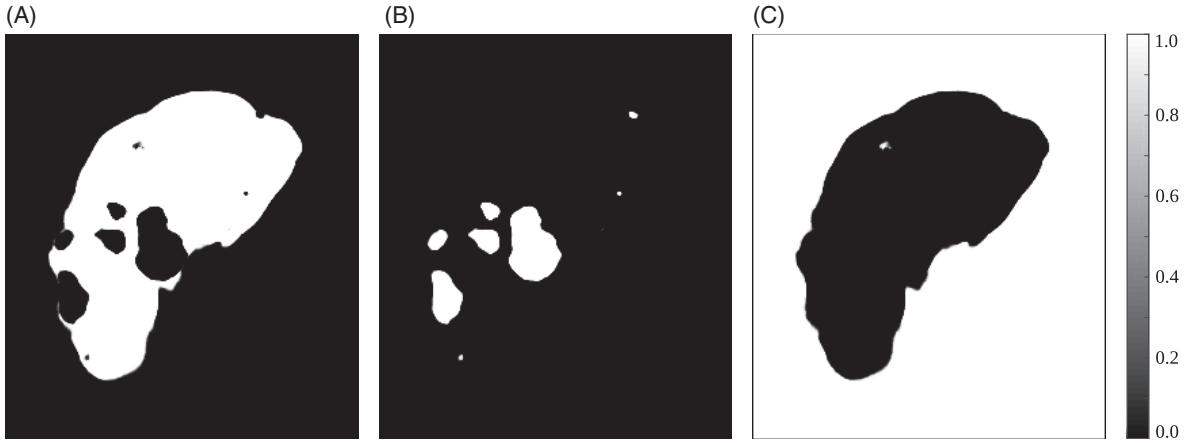

FIGURE 10 One slice of the 3D probability maps for (A) the liver, (B) the tumors, and (C) the surrounding tissue resulting from a three-class U-Net

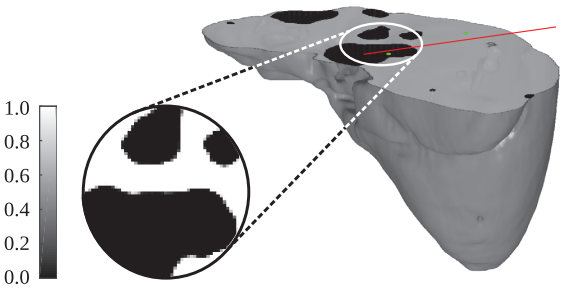

FIGURE 11 3D liver with an enlarged view of the liver probability map. Needle path and reference points are illustrated in red and green, respectively

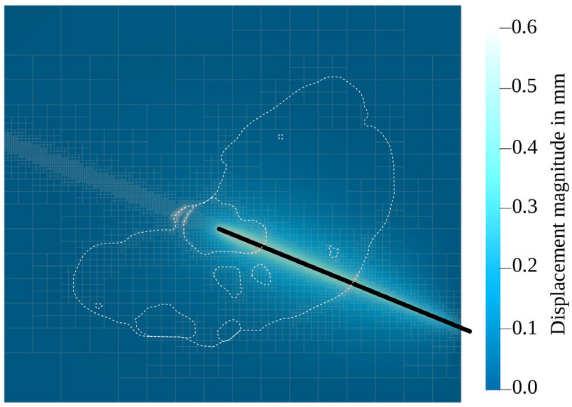

FIGURE 12 The displacement magnitude after needle insertion in one slice. The tissue boundaries are represented as white dotted lines, the needle and the mesh are illustrated in black and gray, respectively. The area within the needle is outside of the physical domain. There is no valid solution on the degrees of freedom in this region and the displacement is therefore not shown

tissue parameters transition smoothly from one organ to the other in the embedded domain. Therefore, the probability maps are used as phase field functions below.

3.4 | Needle insertion simulations on patient data

We perform a simulation of a needle insertion into a tumor of a human liver using the given probability maps. The deformation field is calculated on a regular mesh and the transition between different organs is defined by the transition of elastic parameters within the embedded domain. With this implementation, a definition of the boundary conditions between different tissue types and a collision detection become obsolete. The needle path and two evaluation points are illustrated in Figure 11 in red and green, respectively. Figure 12 shows the deformation magnitude of the tissue and the refined mesh. The grid is adaptively refined around the expected needle path and the tissue boundaries to capture the phase field function at the needle-tissue interface and the transition of tissue parameters. For the refinement around the needle shaft, all cells within 5 mm from the line connecting the entry point and the target point of the needle are refined. All cells in which the liver phase field deviates more than 0.4 on two corners of the cell are considered to be located at the tissue boundary and are therefore refined. The value 0.4 was determined experimentally and generates the most reasonable refinement around the tissue boundary. When a cell is refined multiple times, deal.II automatically refines the surrounding cells to enforce a maximal difference of one refinement level in two neighboring cells. The deformation magnitude within the needle is outside the physical domain Ω and there is no valid solution on the degrees of freedom in this region. It is therefore deleted from the plot.

The simulation is performed for different phase field widths ϵ in the absolute gradient of the phase field function approximating the boundary where traction forces are applied. In Figure 13A the deformation magnitude at the two reference points is shown. The relative error of the displacement magnitude between a phase field width of 0.5 mm and 1.0 mm is 0.3% at the reference point in the tumor and 0.5% at the point in the liver tissue. Figure 13B shows the deformation magnitude at two reference points for different refinements. The deviation from the finest resolution increases with decreasing number of degrees of freedom.

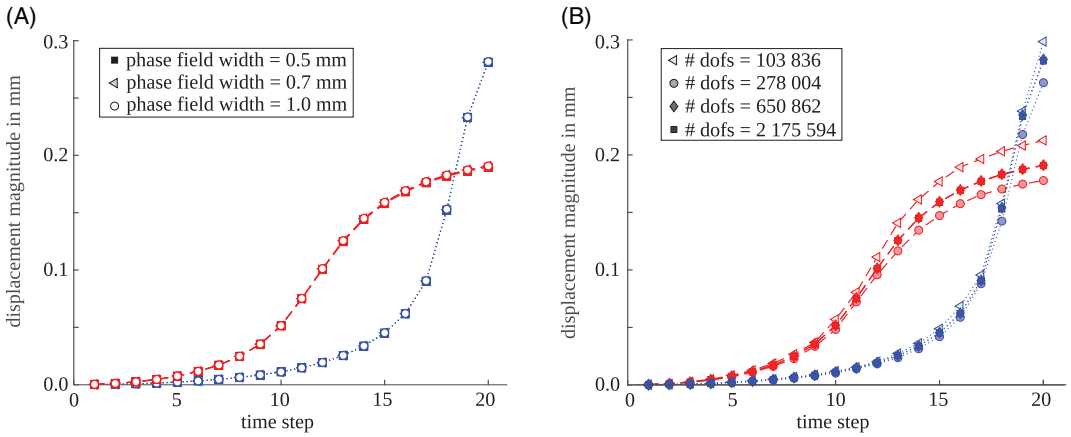

FIGURE 13 Displacement magnitude at two exemplary points in the tissue. Both points are close to the needle shaft. The red curve with dashes is a reference point in the liver tissue, the blue data connected with points corresponds to a reference point in the tumor. The displacement magnitude is shown for (A) varying phase field width and (B) varying grid refinement. The number of degrees of freedom (dofs) is indicated for different grid refinements

4 | DISCUSSION

We investigated the application of the diffuse domain approach to needle insertion FEM simulations. Two different realizations are deployed:

1. The needle tissue interaction, here simply the traction forces applied to the tissue's boundary. The needle-tissue interface is approximated by the absolute gradient of a phase field function $|\nabla \phi|$ and thus boundary terms are converted to volume terms for the integration.
2. The transition between elastic parameters in non-homogeneous tissue. For each of the three tissue types, a probability map is generated with a three-class U-Net which serves as a phase field function ϕ. Thus, each tissue type is embedded in a larger domain. Voxels on the tissue boundary in which the tissue type is not clearly defined serve as the phase field transition region.

The comparison to the conforming mesh simulation of a needle inserted into a homogeneous tissue illustrates the simplicity and applicability of the introduced method. The conforming mesh simulation was performed with the commercial finite element software ANSYS. Since it is not possible to implement the cutting process of the tissue with a quasi-static approximation, a hole was previously introduced. Thus, only friction forces between the needle and the tissue are taken into account. The result shows that even for a commercial software modeling of the friction between two surfaces is not trivial. The contact of the surfaces must be determined by collision detection. Since the tissue is deformed as soon as the needle is inserted, the contact constraints might change along the path of the needle. This explains the smaller displacement at $z = 37$ mm compared to the rest of the needle shaft. Despite the symmetry of the problem, the solution is not symmetric around the needle shaft which might arise from the meshing procedure or the described contact problem. With the introduced method, the boundary conditions are not explicitly defined on the mesh surface. Instead, surface terms are approximated by a phase field function and transformed to volumetric terms in the differential equation. The complexity of handling two meshes can be omitted, which leads to a result symmetric around the needle shaft. To model needles during the insertion into tissue, other methods than 3D meshes have been used. Among them are Euler-Bernoulli beam elements or the angular spring model, which uses connected 1D rods.[38] During the insertion into tissue, the interaction occurs at so called contact nodes, which are nodes of the tissue at the position of the needle shaft.[39] This requires frequent remeshing of the tissue, which is also not necessary in the introduced phase field method.

The deformation of a non-homogeneous tissue is realized by the gradual change of tissue parameters within one large domain. The smooth transition is obtained from probability maps of a convolutional neural network. These maps

contain the full information, which can be received from medical images. Manual or automated soft tissue segmentations, which define a tissue label for each voxel, dissemble an accuracy which is not given in the data. Tissue boundaries in general do not follow the stair-like shape of voxel boundaries. When surface or volume meshes are created from the segmentation, an exact position of the tissue boundary is pretended, as approximation of the true situation. Since there is no need for explicit boundary parameterization in the diffuse domain approach, the mentioned steps can be avoided and the full information contained in the images is used for the deformation simulation. It is of interest if the uncertainty of the segmentation can be directly translated to the uncertainty of elastic tissue parameters and traction forces. As explained before, tissue surfaces usually lie within one voxel and each surface voxel therefore contains two types of cells, for example, healthy liver cells and tumor cells. This is also the case for tumors growing diffusely into the liver tissue with a continuous transformation of the cell types. Presumably the elastic properties of this region are in between the elastic properties of the liver and the tumor. Due to the capsule around the liver, the elastic properties follow nonlinear laws when the liver membrane is punctured.[40] In order to describe the capsule, the boundary would have to have a much higher resolution. In general we cannot assume, that the uncertainty in the segmentation correlates with the uncertainty of the elastic parameters at the tissue boundary. The focus of this work is to open a simple workflow from voxel images to a deformation simulation. The limit in accuracy is mostly due to the deviation of elastic properties between patients.

The elastic shear modulus deviates about 10% between healthy patients and by a factor of about two between healthy patients and patients with cirrhosis.[24] Due to the large deviations of tissue parameters, an accurate patient specific simulation based on parameters from literature is not possible. The deformation simulation cannot be used for accurate treatment planning, but rather as training tool for typical deformation cases. If accurate deformation results and therefore patient specific tissue parameters are needed, an elastography must be performed in advance.

Using the tissue deformation for medical simulators requires real time performance. This is not given with the current implementation. Even though the time consuming system matrix can be assembled in advance, an optimization and parallelization of the assembly of the needle forces and the solving step would be necessary to reduce computation times.

Compared to a state of the art needle insertion simulator,[39] the current implementation does not yet include the deformation of a flexible needle and as mentioned lacks real time performance. However, using voxel-based patient models allows for a simple incorporation of different patient models without the need of time consuming and error-prone meshing.

There are two limitations which will be addressed in future publications. For minimal invasive medical interventions, there are different types of needles. We investigated the tissue deformation during the insertion of a rigid needle. In brachytherapy, flexible needles are used to allow for steering in the tissue. The extension to a flexible needle has to be addressed next. Additionally, studies[22,23] show that the liver tissue follows hyperelastic or viscoelastic material laws. The linear elastic tissue model is only an approximation for small deformations. The introduced diffuse elastic equation can easily be extended to non-linear tissue models, which however comes with a high computational effort. The influence of non-linear behavior must be quantified for the tissue deformation during needle insertion. In a next step, rigorous experimental validation of the present method is required. The deformation of a flexible needle regarding different angles of the bevel tip and the corresponding tissue deformation must be evaluated. It must be performed on the simple example of homogeneous tissue and further with the presence of a tissue boundary within the sample.

5 | CONCLUSION

In this paper, we present a method for elastomechanical medical simulations directly on voxel data using the example of a needle insertion simulation. We use the diffuse domain approach to model the transition of elastic parameters from one tissue to another and the interaction between the needle and the tissue. Explicit boundary parameterization and meshing of complex organ shapes is overcome. Instead, the simulation is performed on an regular grid.

The deformation result using a diffuse domain method on a regular mesh is comparable to a conventional conforming mesh simulation. While the deformation components perpendicular to the needle shaft are not captured by the current model, the much larger parallel component is described well.

Due to the voxel based tissue representation, simulations with different patient models are easily implementable. For conventional structural analysis, organs must be segmented from discrete imaging data. The organs' segmentations are discretized with meshes, which are conforming with the complex geometry of the organ and boundary conditions

between the different meshes must be defined. In the presented method, there is no need for explicit boundary parameterization and conforming meshes. There is a voxel-based tissue representation from the imaging modality to the deformation simulation. The transition between tissue types is indirectly represented by probability maps derived from the neural network. Avoiding manual segmentation and meshing allows for automated patient-specific deformation simulations.

Uncertainties of elastic parameters at tissue boundaries due to the discrete nature of imaging modalities are directly incorporated in the deformation simulation through the width of the phase field. In a mesh based approach, clear tissue boundaries are defined, which pretends a certainty that is not given in the original data.

ACKNOWLEDGEMENTS

KI Jerg acknowledges support from the German Research Foundation through the grant HE 3011/36-1.

CONFLICTS OF INTEREST

All other authors declare that they have no conflicts of interest.

DATA AVAILABILITY STATEMENT

We are making the data and the code associated with this paper available.

ORCID

Katharina I. Jerg https://orcid.org/0000-0002-8202-9936

REFERENCES

1. Bretschneider T, Ricke J, Gebauer B, Streitparth F. Image-guided high-dose-rate brachytherapy of malignancies in various inner organs–technique, indications, and perspectives. *J Contemp Brachytherapy*. 2016;8(3):253.
2. Ricke J, Wust P. Computed tomography–guided brachytherapy for liver cancer. *Semin Radiat Oncol*. 2011;21:287-293.
3. Alterovitz R, Goldberg K. *Motion Planning in Medicine: Optimization and Simulation Algorithms for Image-guided Procedures. Springer Tracts in Advanced Robotics*. Berlin, Germany: Springer; 2008.
4. Miller GS. The motion dynamics of snakes and worms. *ACM*. 1988;22:169-173.
5. Gibson SF. 3D Chainmail:a fast algorithm for deforming volumetric objects. *SI3D*. 1997;97:149.
6. Zhang J, Zhong Y, Gu C. Deformable models for surgical simulation: a survey. *IEEE Rev Biomed Eng*. 2018;11:143-164.
7. Kockelkoren J, Levine H, Rappel WJ. Computational approach for modeling intra- and extracellular dynamics. *Phys Rev E*. 2003;68:037702. https://doi.org/10.1103/PhysRevE.68.037702.
8. Bui HP, Tomar S, Bordas SP. Corotational cut finite element method for real-time surgical simulation: application to needle insertion simulation. *Comput Methods Appl Mech Eng*. 2019;345:183-211.
9. Ruess M, Tal D, Trabelsi N, Yosibash Z, Rank E. The finite cell method for bone simulations: verification and validation. *Biomech Model Mechanobiol*. 2012;11(3–4):425-437.
10. Nguyen L, Stoter S, Baum T, et al. Phase-field boundary conditions for the voxel finite cell method: surface-free stress analysis of CT-based bone structures. *Int J Numer Method Biomed Eng*. 2017;33(12):e2880.
11. Teigen KE, Li X, Lowengrub J, Wang F, Voigt A. A diffuse-interface approach for modeling transport, diffusion and adsorption/desorption of material quantities on a deformable interface. *Commun Math Sci*. 2009;7(4):1009.
12. Elliott CM, Stinner B, Styles V, Welford R. Numerical computation of advection and diffusion on evolving diffuse interfaces. *IMA J Numer Anal*. 2010;31(3):786-812.
13. Miehe C, Hofacker M, Welschinger F. A phase field model for rate-independent crack propagation: robust algorithmic implementation based on operator splits. *Comput Methods Appl Mech Eng*. 2010;199(45–48):2765-2778.
14. Borden MJ, Verhoosel CV, Scott MA, Hughes TJ, Landis CM. A phase-field description of dynamic brittle fracture. *Comput Methods Appl Mech Eng*. 2012;217:77-95.
15. Lorenzo G, Scott MA, Tew K, et al. Tissue-scale, personalized modeling and simulation of prostate cancer growth. *Proc Natl Acad Sci*. 2016;113(48):E7663-E7671.
16. Li X, Lowengrub J, Rätz A, Voigt A. Solving PDEs in complex geometries: a diffuse domain approach. *Commun Math Sci*. 2009;7(1):81-107.
17. Schlottbom M. Error analysis of a diffuse interface method for elliptic problems with Dirichlet boundary conditions. *Appl Numer Math*. 2016;109:109-122.
18. Nguyen LH, Stoter SK, Ruess M, Sanchez Uribe MA, Schillinger D. The diffuse Nitsche method: Dirichlet constraints on phase-field boundaries. *Int J Numer Methods Eng*. 2018;113(4):601-633.
19. Holzapfel GA. *Nonlinear Solid Mechanics: A Continuum Approach for Engeneering*. England: John Wiley & Sons Ltd; 2010.
20. Mase G, Mase G. *Continuum Mechanics for Engineers*. 2nd ed. Boca Raton, FL: CRC Press; 1999.

21. Arndt D, Bangerth W, Clevenger TC, et al. The deal.II library, version 9.1. *J Numer Math*. 2019;27(4):203-213. https://doi.org/10.1515/jnma-2019-0064.
22. Umale S, Deck C, Bourdet N, et al. Experimental mechanical characterization of abdominal organs: liver, kidney & spleen. *J Mech Behav Biomed Mater*. 2012;17:22-33. https://doi.org/10.1016/j.jmbbm.2012.07.010.
23. Kobayashi Y, Onishi A, Watanabe H, Hoshi T, Kawamura K, Fujie MG. in vitro validation of viscoelastic and nonlinear physical model of liver for needle insertion simulation. Proceedings of the 2nd Biennial IEEE/RAS-EMBS International Conference on Biomedical Robotics and Biomechatronics; 2008; BioRob. pp. 469–476. doi: https://doi.org/10.1109/BIOROB.2008.4762837
24. Huwart L, Peeters F, Sinkus R, et al. Liver fibrosis: non-invasive assessment with MR elastography. *NMR Biomed*. 2006;19(2):173-179.
25. Lervåg KY, Lowengrub J. Analysis of the diffuse-domain method for solving PDEs in complex geometries. 2014. arXiv preprint arXiv: 1407.7480.
26. Runborg O. Lecture notes in numerical solutions of differential equations, verifying numerical convergence rates. 2012. http://www.csc.kth.se/utbildning/kth/kurser/DN2255/ndiff13/ConvRate.pdf. Accessed on July 24, 2019.
27. Bilic P, Christ PF, Vorontsov E, et al. The liver tumor segmentation benchmark (LiTS). *arXiv:1901.04056*. 2019. https://arxiv.org/abs/1901.04056.
28. Christ PF et al. Automatic liver and lesion segmentation in CT using cascaded fully convolutional neural networks and 3D conditional random fields. Paper presented at: International Conference on Medical Image Computing and Computer-Assisted Intervention 2016; 415-423.
29. Roth K, Konopczynski TK, Hesser J. Liver lesion segmentation with slice-wise 2D tiramisu and Tversky loss function. *arXiv:1905.03639*. 2019. https://arxiv.org/abs/1905.03639.
30. Han X. Automatic liver lesion segmentation using a deep convolutional neural network method. *arXiv:1704.07239*. 2017. https://arxiv.org/abs/1704.07239.
31. Li X, Chen H, Qi X, Dou Q, Fu C, Heng P. H-DenseUNet: hybrid densely connected UNet for liver and liver tumor segmentation from CT volumes. *IEEE T Med imaging*. 2017;37(12):2663-2674.
32. Ronneberger O, Fischer P, Brox T. U-net: convolutional networks for biomedical image segmentation. Paper presented at: International Conference on Medical image computing and computer-assisted intervention 2015;234-241.
33. He K, Zhang X, Ren S, Sun J. Deep residual learning for image recognition. Paper presented at: Proceedings of the IEEE conference on computer vision and pattern recognition 2015;770-778.
34. Ioffe S, Szegedy C. Batch normalization: accelerating deep network training by reducing internal covariate shift. *arXiv:1502.03167*. 2015. https://arxiv.org/abs/1502.03167.
35. Yu F, Koltun V, Funkhouser TA. Dilated residual networks. Paper presented at: Proceedings of the IEEE conference on computer vision and pattern recognition 2017;472-480.
36. Kingma D, Ba J. Adam. A method for stochastic optimization. International Conference on Learning Representations; 2014.
37. Drozdzal M et al. The importance of skip connections in biomedical image segmentation. *Deep Learn Data Label Med Appl*. 2016; 179-187.
38. Goksel O, Dehghan E, Salcudean SE. Modeling and simulation of flexible needles. *Med Eng Phys*. 2009;31(9):1069-1078.
39. Goksel O, Sapchuk K, Salcudean SE. Haptic simulator for prostate brachytherapy with simulated needle and probe interaction. *IEEE Trans Haptics*. 2011;4(3):188-198.
40. Okamura AM, Simone C, O'leary MD. Force modeling for needle insertion into soft tissue. *IEEE Trans Biomed Eng*. 2004;51(10):1707-1716.

How to cite this article: Jerg KI, Austermühl RP, Roth K, et al. Diffuse domain method for needle insertion simulations. *Int J Numer Meth Biomed Engng*. 2020;36:e3377. https://doi.org/10.1002/cnm.3377

APPENDIX A.

Normalization of $|\nabla \phi|$

In order to use the absolute gradient of the phase field function $|\nabla \phi|$ as approximation for the δ function in Equation 3, we must show that $|\nabla \phi|$ of Equation 4 is normalized correctly. In the following we show for one dimension that its integral over the full domain results into one and it is therefore normalized as the Dirac δ.

We start with the phase field function

$$\phi(x) = \frac{1}{2}\left(1 - \tanh\left(\frac{3x}{\epsilon}\right)\right)$$

and its absolute gradient

$$|\nabla\phi| = \left|\frac{d\phi}{dx}\right| = \frac{3}{2\epsilon\cosh^2\left(\frac{3x}{\epsilon}\right)}.$$

Given that

$$\tanh(x)_{(x\to\infty)} = \frac{e^x - e^{-x}}{e^x + e^{-x}}_{(x\to\infty)} = \frac{e^x}{e^x + e^{-x}} - \frac{e^{-x}}{e^x + e^{-x}}_{(x\to\infty)} = \frac{1}{1 + e^{-2x}} - \frac{e^{-x}}{e^x + e^{-x}}_{(x\to\infty)} \approx 1 - 0 = 1$$

and

$$\tanh(x)_{(x\to-\infty)} = \frac{e^x - e^{-x}}{e^x + e^{-x}}_{(x\to-\infty)} = \frac{e^x}{e^x + e^{-x}} - \frac{e^{-x}}{e^x + e^{-x}}_{(x\to-\infty)} = \frac{e^{2x}}{e^{2x} + 1} - \frac{1}{e^{2x} + 1}_{(x\to-\infty)} \approx 0 - 1 = -1$$

the following integration over the full domain shows that it is normalized to one and that it can therefore be used to approximate the delta function.

$$\int_{-\infty}^{\infty} |\nabla\phi| dx = \int_{-\infty}^{\infty} \frac{3}{2\epsilon\cosh^2\left(\frac{3x}{\epsilon}\right)} dx = \left[\frac{1}{2}\tanh\left(\frac{3x}{\epsilon}\right)\right]_{-\infty}^{\infty} = \frac{1}{2}(1 - (-1)) = 1$$

Linear elastic equation

The derivation of the linear elastic equation for an isotropic material is shown in the following. We use the Einstein notation, hence it is summed over indices appearing twice in one term over all values of the index. The double contraction of two tensors $\boldsymbol{A}$ and $\boldsymbol{B}$ results in a scalar and is denoted by: In index notation it can be written as[19] $\boldsymbol{A} : \boldsymbol{B} = A_{ij}B_{ij}$. The partial derivative with respect to the $\boldsymbol{i}$-th variable ∂/∂_i is shortened with ∂_i and δ_{ij} describes the Kronecker delta. The phase field function ϕ and the absolute value of its gradient $|\nabla\phi|$ are scalar functions.

We start with Equation 6 and observe each of its three terms separately.

$$\delta W(\boldsymbol{u}, \delta\boldsymbol{u}) \approx \int_{\Omega_0} (\boldsymbol{\sigma} : \delta\boldsymbol{\epsilon} - \boldsymbol{b}\cdot\delta\boldsymbol{u})\phi d\Omega_0 - \int_{\Omega_0} \boldsymbol{t}\cdot\delta\boldsymbol{u} \,|\nabla\phi|\, d\Omega_0$$

$$= \underbrace{\int_{\Omega_0} \boldsymbol{\sigma} : \delta\boldsymbol{\epsilon}\phi d\Omega_0}_{I} - \underbrace{\int_{\Omega_0} \boldsymbol{b}\cdot\delta\boldsymbol{u}\phi d\Omega_0}_{II} - \underbrace{\int_{\Omega_0} \boldsymbol{t}\cdot\delta\boldsymbol{u} \,|\nabla\phi|\, d\Omega_0}_{II} \approx 0$$

$$I = \int_{\Omega_0} \boldsymbol{\sigma} : \delta\boldsymbol{\epsilon}\phi d\Omega_0$$

$$= \int_{\Omega_0} \sigma_{ij}\delta\epsilon_{ij}\phi d\Omega_0$$

With Equation 7 and $\epsilon_{ij} = \frac{1}{2}(\partial_i u_j + \partial_j u_i)$

$$= \int_{\Omega_0} \left(\lambda \delta_{ij} \epsilon_{kk} + 2\mu \epsilon_{ij}\right) \frac{1}{2} \left(\partial_i \delta u_j + \partial_j \delta u_i\right) \phi \, d\Omega_0$$

$$= \int_{\Omega_0} \left(\frac{1}{2} \lambda \delta_{ij} \epsilon_{kk} \partial_i \delta u_j + \frac{1}{2} \lambda \delta_{ij} \epsilon_{kk} \partial_j \delta u_i + \mu \epsilon_{ij} \partial_i \delta u_j + \mu \epsilon_{ij} \partial_j \delta u_i \right) \phi \, d\Omega_0$$

$$= \int_{\Omega_0} \left(\frac{1}{2} \lambda \epsilon_{kk} \partial_j \delta u_j + \frac{1}{2} \lambda \epsilon_{kk} \partial_j \delta u_j + \mu \epsilon_{ij} \partial_i \delta u_j + \mu \epsilon_{ij} \partial_j \delta u_i \right) \phi \, d\Omega_0$$

$$= \int_{\Omega_0} \left(\frac{1}{2} \lambda \partial_k u_k \partial_j \delta u_j + \frac{1}{2} \lambda \partial_k u_k \partial_j \delta u_j + \mu \frac{1}{2} \left(\partial_i u_j + \partial_j u_i\right) \partial_i \delta u_j + \mu \frac{1}{2} \left(\partial_i u_j + \partial_j u_i\right) \partial_j \delta u_i \right) \phi \, d\Omega_0$$

$$= \int_{\Omega_0} \left(\lambda \partial_k u_k \partial_j \delta u_j + \mu \frac{1}{2} \partial_i u_j \partial_i \delta u_j + \mu \frac{1}{2} \partial_j u_i \partial_i \delta u_j + \mu \frac{1}{2} \partial_i u_j \partial_j \delta u_i + \mu \frac{1}{2} \partial_j u_i \partial_j \delta u_i \right) \phi \, d\Omega_0$$

renaming k to i the first term, and i to j and j to i in the last two terms leads to

$$= \int_{\Omega_0} \left(\lambda \partial_i u_i \partial_j \delta u_j + \mu \partial_i u_j \partial_i \delta u_j + \mu \partial_j u_i \partial_i \delta u_j \right) \phi \, d\Omega_0$$

$$II = \int_{\Omega_0} \boldsymbol{b} \cdot \delta \boldsymbol{u} \, \phi \, d\Omega_0 = \int_{\Omega_0} b_i \delta u_i \, \phi \, d\Omega_0$$

$$III = \int_{\Omega_0} \boldsymbol{t} \cdot \delta \boldsymbol{u} \mid \nabla \phi \mid d\Omega_0 = \int_{\Omega_0} t_i \delta u_i \mid \nabla \phi \mid d\Omega_0$$

Publication II: Flexible Needle Insertion and Tissue Relaxation Simulation

Title: Diffuse Domain Approach for Flexible Needle Insertion and Relaxation

Authors: Katharina I. Jerg, Lalith Boggaram Naveen, Guido Kanschat, Ernest Chukwudi N. Okonkwo, Jürgen W. Hesser

Journal: International Journal for Numerical Methods for Biomedical Engineering

DOI: 10.1002/cnm.3782

Thesis Context: Utilizing realistic needle insertion simulations without the need for manual interaction during LDR brachytherapy treatment planning can improve the clinical outcome. In brachytherapy, just like many other minimally invasive procedures, flexible needles with beveled tips are used. This must be considered when implementing realistic simulations.

Contribution to state-of-the-art: To be applied to brachytherapy treatment planning, the previously introduced diffuse domain approach is extended to the use of flexible needles and such to a more sophisticated interaction between the needle and the tissue. In literature both needle insertion simulations and corresponding experiments are performed with clamped needles. During brachytherapy needles are inserted and afterwards released by the physician. Since there can be remaining tension inside the tissue the needle-tissue system relaxes when released, possibly changing the relative needle tissue positioning. Since this relative positioning is crucial for the dose calculation we additionally propose a method to model the relaxation of the system. Besides introducing the two methods, the needle insertion simulation of the flexible needle is verified on a real-world phantom experiment performed at John-Hopkins-University in 2005 [30] in this publication.

Received: 17 April 2023 | Revised: 1 September 2023 | Accepted: 8 September 2023

DOI: 10.1002/cnm.3782

APPLIED RESEARCH

WILEY

Diffuse domain approach for flexible needle insertion and relaxation

Katharina I. Jerg[1] | **Lalith Boggaram Naveen**[1] | **Guido Kanschat**[2] | **Ernest Chukwudi N. Okonkwo**[1,3] | **Jürgen W. Hesser**[1,2,4,5]

[1]Mannheim Institute for Intelligent Systems in Medicine (MIISM), Heidelberg University, Mannheim, Germany

[2]Interdisciplinary Center for Scientific Computing (IWR), Heidelberg University, Heidelberg, Germany

[3]Department of Radiotherapy and Radiation Oncology, Ortenau Klinikum Offenburg-Kehl, Offenburg, Germany

[4]Central Institute for Computer Engineering (ZITI), Heidelberg University, Heidelberg, Germany

[5]CZS Heidelberg Center for Model-Based AI, Heidelberg University, Mannheim, Germany

Correspondence
Katharina I. Jerg, Mannheim Institute for Intelligent Systems in Medicine (MIISM), Heidelberg University, Mannheim, Germany.
Email: katharina.jerg@medma.uni-heidelberg.de

Funding information
Deutsche Forschungsgemeinschaft, Grant/Award Number: HE 3011/36-1

Abstract

Needle insertion simulations play an important role in medical training and surgical planning. Most simulations require boundary conforming meshes, while the diffuse domain approach, currently limited to stiff needles, eliminates the need for meshing geometries. In this article the diffuse domain approach for needle insertion simulations is first extended to the use of flexible needles with bevel needle tips, which are represented by an Euler-Bernoulli beam. The model parameters are tuned and the model is evaluated on a real-world phantom experiment. Second, a new method for the relaxation of the needle-tissue system after the user releases the needle is introduced. The equilibrium state of the system is determined by minimizing the potential energy. The convergence rate of the coupled Laplace equations for solving the Euler-Bernoulli beam is 1.92 ± 0.14 for decreasing cell size. The diffuse penalty method for the application of Dirichlet boundary conditions results in a convergence rate of 0.73 ± 0.21 for decreasing phase field width. The simulated needle deviates on average by 0.29 mm compared to the phantom experiment. The error of the tissue deformation is below 1 mm for 97.5% of the attached markers. Two additional experiments demonstrate the feasibility of the relaxation process. The simulation method presented here is a valuable tool for patient-specific medical simulations using flexible needles without the need for boundary conforming meshing. To the best of the authors' knowledge this is the first work to introduce a relaxation model, which is a major step for simulating accurate needle-tissue positioning during realistic medical interventions.

KEYWORDS

deformable needle insertion, diffuse domain method, diffuse penalty method, Euler–Bernoulli beam theory, linear elastic equation, needle-tissue interaction, tissue relaxation

1 | INTRODUCTION

Many minimal invasive medical procedures use needles. One example is brachytherapy where radioactive sources are inserted into the tumor using bevel-tip needles. In order to ensure successful interventions, minimal side effects, and in case of brachytherapy a satisfactory dose coverage accurate placement of the needles inside the tissue is needed. In the brachytherapy planning process the needle insertion task is currently not considered, however, urologists are expected to place the needles based on experience. The knowledge about needle positioning and tissue deformation under needle insertion could therefore improve the planning process, especially if inverse radiation treatment planning is implemented. Moreover, needle-tissue interaction simulations are needed for robot-assisted surgery or surgical training.

Tissue deformation during the insertion of a stiff needle with a symmetric tip is simulated in various ways using the finite element (FE) method to model accurate tissue deformation based on constitutive laws.[1–3] However, in medical interventions flexible needles with beveled tips are used in order to steer the needle through the tissue. By rotating the needle and thus changing the direction of the bevel, the physician can manipulate the path and force the needle to move into the opposite direction. Including flexible needles and their interaction with the tissue results in a deformation on both the needle and the tissue and thus makes simulations a more challenging task.

In order to model needle deformation Goksel et al.[4] compare the beam deflection of two different 2D non-linear beam elements with an angular spring model. The Euler-Bernoulli beam theory is used to model the needle deflection by Lehmann et al.[5] and an energy based formulation is presented by Misra et al.[6] In the latter the needle deformation is related to tissue properties and force considerations on the beveled tip depending on the bevel angle. Khadem et al.[7] develop a needle model which includes the insertion velocity as input parameter. Using an arbitrary Lagrangian–Eulerian finite element method, Yamaguchi et al.[8] include tissue fracture in their simulation, which they compare to a needle insertion experiment. In these approaches only the needle deflection is evaluated on phantom experiments. The deformation of the tissue along the shaft and throughout the volume are neither investigated nor confirmed by experiment. When the positioning of the needle inside physical structures and e.g. the placement of radioactive sources in brachytherapy are under investigation, it is important to know the deformation of the soft tissue.

Chentanez et al.[9] present a 3D FE simulation of a tetrahedrally meshed tissue interacting with a 1D elastic rod. The mesh is dynamically updated to place tissue nodes on the needle shaft and apply friction boundary condition on those nodes. They show an example how a beveled tip needle can be steered around obstacles and validate the method on an experiment also including the tissue deformation traced by surface markers. A complete surgical simulation including tissue deformation, seed placement, visual control by a simulated transrectal ultrasound, dosimetry calculations, and displacement boundary constraints due to the ultrasound probe and the pelvic bone is developed by Goksel et al.[10] A quasi-static linear strain model is used to model the soft tissue. The needle's position is manipulated by the user and used as input to the simulation. A lateral movement of the needle after the user releases the needle is not considered. In order to run the simulation on patient data they employ the 3D image meshing software VIMesh to generate tetrahedral meshes of the different structures.

In our previous work a needle insertion simulation on a voxel basis and without the need of meshing was introduced.[3] It is based on the so-called fictitious or embedded domain method introduced by Kockelkoren et al.[11] The general idea is to embed the domain of interest in a larger regular domain and instead of applying boundary conditions explicitly on a sharp boundary a smooth phase field function transitioning from 0 outside to 1 inside the domain is defined. In order to differentiate between different tissue types meshing of the organs' geometries is necessary for other FEM needle insertion simulations. The time consuming meshing can be skipped using the diffuse domain or also called phase field approach, since the calculation is performed on a regular grid. The uncertainty of the tissue segmentation is translated to a representation of the smooth transitioning of elastic parameters between different tissue types inside the target volume. This automated method allows patient-specific simulations directly on voxel data and without the need of meshing complex geometries. For the interaction between needle and tissue, friction forces are applied as traction force to the tissue. These traction boundary conditions are approximated by the absolute gradient of a phase field function and are thus transformed to volumetric terms in the differential equation. The full pipeline from patient data, automated segmentation, and needle insertion simulation on complex shaped tissue can be found in Jerg et al.[3] One disadvantage of the introduced model is the use of stiff needles, which is not always the case during surgical interventions.

Another issue that, to the best of our knowledge, has never been addressed in literature is the behavior of the needle-tissue system when the physician releases the needle. This is relevant because during brachytherapy multiple needles are inserted and released and afterwards radioactive seeds are applied through the needles. In most needle

insertion experiments the needle is clamped at its base[4,9] and thus its final position is not influenced by the tissue. When the tissue sticks to the needle shaft due to stick-friction there is a remaining tension inside the tissue.

The first contribution of this article is to extend the diffuse domain needle insertion model by a flexible needle and enhance the interaction model with the soft tissue. The lateral deflection of the needle is modeled using the Euler-Bernoulli beam equation. The needle-tissue interaction consisting of friction forces on the tissue boundary is extended by lateral forces acting on the needle shaft due to tissue deformation and a resulting tip force driving the needle deformation due to its angled bevel tip. The model parameters are tuned and the model is validated on a real-world phantom experiment of a needle insertion performed at Johns Hopkins University in 2005.[9]

The second contribution of this article is the first known implementation of the needle-tissue relaxation after the needle is released by the physician. After insertion the tissue sticks to the needle due to stick friction and therefore there is no relative movement of the tissue along the needle shaft. In order to find the final needle position and tissue deformation, the relative tissue displacement along the needle is kept constant. This relative boundary condition is applied to the tissue using the diffuse penalty method[12,13] and the potential energy inside the tissue is minimized using linear optimization. This is an essential step towards realistic simulations of surgical interventions and especially for reasonable needle-tissue positioning for advanced brachytherapy planning.

This article is organized as follows: In Section 2 the improved needle-tissue interaction model is introduced after giving a short overview of the diffuse domain method and the corresponding partial differential equations. Next, the phantom data for the validation of the needle insertion is presented. In Section 3 the results of the convergence analyses for both the diffuse penalty method for the application of Dirichlet boundary conditions and the Euler-Bernoulli beam modeling the transverse displacement of the needle are shown. Next, the parameter tuning and error analysis regarding the insertion experiment and experiments regarding the relaxation process are performed. The results are discussed in Section 4 and a conclusion is drawn in Section 5.

2 | MATERIALS AND METHODS

In this chapter the diffuse domain method followed by the differential equations for both the tissue and the needle are introduced. The first is described by a quasi-static linear elastic model, while the latter obeys the Euler–Bernoulli beam theory. The needle-tissue interaction model and the model for the relaxation process due to remaining tension inside the tissue is explained. After explaining the experiments for the convergence analyses, the real-world phantom experiment used for parameter tuning and validation of the needle insertion is introduced.

2.1 | Embedded domain and phase field approximation

As shown in Figure 1, a considered domain Ω (left) can be embedded in a larger fictitious domain Ω_0[11] (middle), which is regularly meshed. The Heaviside step function $H(x) = \{1 \forall x \in \Omega, 0 \text{ otherwise}\}$ represents a sharp boundary to distinguish between inside and outside of the physical domain. A phase field function ϕ can be defined as an approximation to the step function and represents a diffuse boundary (right). The volume integral over a function Q can be written as[12–14]

$$\int_{\Omega} Q d\Omega = \int_{\Omega_0} QH d\Omega_0 \approx \int_{\Omega_0} Q\phi d\Omega_0. \tag{1}$$

In order to consider the boundary conditions on a surface Γ, the Dirac distribution δ_Γ is approximated by the absolute gradient of the phase field function $|\nabla\phi|$. A boundary integral of a function h over a boundary Γ can be written as[13,14]:

$$\int_{\Gamma} h d\Gamma = \int_{\Omega_0} h\delta_\Gamma d\Omega \approx \int_{\Omega_0} h |\nabla\phi| d\Omega. \tag{2}$$

We chose the phase field function ϕ to be

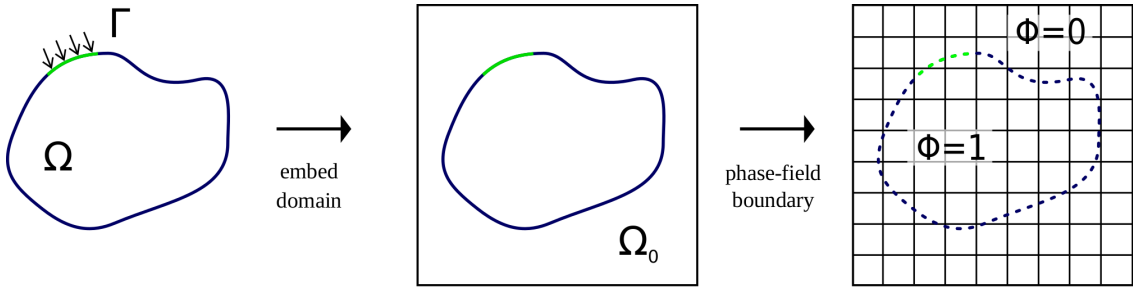

FIGURE 1 A physical domain Ω with boundary conditions on Γ (left) is embedded in a larger domain Ω_0 (middle). Ω_0 is regularly meshed and the sharp boundary is approximated by a smooth phase field function ϕ (right) from Reference 3.

$$\phi(\mathbf{x}) = \frac{1}{2}\left(1 - tanh\left(\frac{3r(\mathbf{x})}{\varepsilon}\right)\right), \mathbf{x} \in \Omega_0, \tag{3}$$

as in Li et al.[14] In the equation $r(\mathbf{x})$ is a signed distance function from the boundary Γ which is defined negative inside and positive outside of Ω and ε defines the width of the phase field function. For a more detailed explanation of the diffuse domain method and the verification of the correct normalization of $|\nabla\phi|$ the reader is referred to Jerg et al.[3]

2.2 | Tissue model and application of boundary conditions

The diffuse variational formulation of the penalty method for a quasi-static linear elastic tissue can be expressed as follows: Find the displacement field $\boldsymbol{u}$ such that

$$\begin{aligned} &\int_{\Omega_0} (\boldsymbol{\sigma} : \delta\boldsymbol{\varepsilon})\phi \, d\Omega_0 + \beta \int_{\Omega_0} \boldsymbol{u} \cdot \delta\boldsymbol{u} \, |\nabla\phi| \, d\Omega_0 = \\ &\int_{\Omega_0} \boldsymbol{t} \cdot \delta\boldsymbol{u} \, |\nabla\phi| \, d\Omega_0 + \beta \int_{\Omega_0} \boldsymbol{g} \cdot \delta\boldsymbol{u} \, |\nabla\phi| \, d\Omega_0 \end{aligned}, \tag{4}$$

for all $\delta\boldsymbol{u}$. $\delta\boldsymbol{u}$ are the virtual displacements, $\boldsymbol{\sigma}$ is the stress tensor, $\delta\boldsymbol{\varepsilon} = 1/2(\nabla\delta\boldsymbol{u} + \nabla\delta\boldsymbol{u}^T)$ is the virtual strain tensor, β is a penalty parameter, $\boldsymbol{t}$ denotes the traction force and $\boldsymbol{g}$ the displacement at the boundary. This is the same formulation as previously introduced in Jerg et al.[3] with body forces equal to zero and additional penalty terms to apply Dirichlet boundary conditions on the boundary Γ.[12] For both traction and Dirichlet boundary conditions boundary integrals are transformed to volume integrals by multiplying the absolute gradient of the phase field function $|\nabla\phi|$ according to Equation (2). In the first term the volume integral over the domain Ω is extended to the domain Ω_0 by the multiplication with the phase field function ϕ (see Equation (1)).

In the case of an isotropic linear elastic material the stress tensor only depends on the two Lamé parameters λ and μ. This leads to the respective bilinear form

$$\begin{aligned} &\int_{\Omega_0} \left(\lambda\partial_i u_i \partial_j \delta u_j + \mu\partial_i u_j \partial_i \delta u_j + \mu\partial_j u_i \partial_i \delta u_j\right)\phi \, d\Omega_0 + \beta \int_{\Omega_0} u_i \delta u_i \, |\nabla\phi| \, d\Omega_0 = \\ &\int_{\Omega_0} t_i \delta u_i \, |\nabla\phi| \, d\Omega_0 + \beta \int_{\Omega_0} g_i \delta u_i \, |\nabla\phi| \, d\Omega_0. \end{aligned} \tag{5}$$

The partial derivative with respect to the i-th component is denoted by ∂_i. It must be mentioned that traction and displacement boundary conditions are not applied at the same time. Either β or $\mathbf{t}$ is zero, which is the case during insertion or relaxation, respectively. The choice of β is crucial when using the penalty method to apply Dirichlet boundary

conditions. According to Nguyen et al.[13] it is recommended to use $\beta = 1000 \cdot E = 1000 \cdot \frac{\mu(3\lambda+2\mu)}{\lambda+\mu}$ for a linear elastic equation.

The simulation is implemented in the C++ finite element library deal.II.[15] The tissue domain is discretized in a hexahedral mesh and for each space dimension linear Lagrange finite elements are used. For numerical integration a tensor product of three one-dimensional two-point Gauss-Legendre quadrature formulas is used to allow an optimal approximation.

2.2.1 | Needle insertion

During needle insertion the end of the needle is clamped to the user's hand and is moved inside the tissue. The force applied to the tissue is equal to the cutting force at the needle tip and a sliding friction force along the shaft due to its relative velocity to the tissue. This sliding friction is the main component leading to tissue deformation and is modeled as a force boundary condition to the tissue with magnitude t and in direction parallel to the needle shaft.[3]

2.2.2 | Needle-tissue relaxation

When the user releases the needle, the external force on the needle is zero and the position may not remain fixed. The tissue sticks to the needle shaft due to static friction and the relative displacements $\boldsymbol{g}^*$ along the needle shaft are fixed. The equilibrium configuration $\widehat{\boldsymbol{g}}$ with the least tension inside the tissue is now to be found. In an isotropic linear elastic material the energy density $W(\boldsymbol{\varepsilon})$ follows a quadratic potential[16]

$$W(\boldsymbol{\varepsilon}) = \frac{\lambda}{2} tr^2(\boldsymbol{\varepsilon}) + \mu tr\left(\boldsymbol{\varepsilon}^2\right). \tag{6}$$

Integrating the energy density over the tissue domain results in the stored potential energy U and will lead to the equilibrium state of the system when minimized. Due to the setup it can be expected that this state is around a zero average displacement of the tissue along the needle shaft. The optimization is therefore performed as follows: For each coordinate direction i three deformation vector fields $\boldsymbol{d}$ in direction i are defined. They are constant over the boundary and of magnitude $|\boldsymbol{d_1}| = 0$, $|\boldsymbol{d_2}| = -\overline{\boldsymbol{g}^*}_i$, and $|\boldsymbol{d_3}| = -1.5 \cdot \overline{\boldsymbol{g}^*}_i$, where $\overline{\boldsymbol{g}^*}_i$ is the i-th component of the average boundary displacement. The deformation of the tissue for each displacement boundary condition $\boldsymbol{g} = \boldsymbol{g}^* + \boldsymbol{d}$ (compare Figure 2A, left and middle) and the potential energy U is calculated. For each coordinate direction $\boldsymbol{d^{min}}_i = \arg\min\left(U(\boldsymbol{d})_i\right)$ is determined for the parabolic fit (see Figure 2B) and finally the elastic equations of the equilibrium state are solved with boundary values $\widehat{\boldsymbol{g}} = \boldsymbol{g}^* + \boldsymbol{d^{min}}$ along the shaft (Figure 2A, right). The needle is moved by $\boldsymbol{d^{min}}$ into its rest position.

2.3 | Needle model

The response of the needle due to lateral loads along the shaft and the model of the beveled needle tip are presented in this section.

2.3.1 | Euler–Bernoulli beam

In solid mechanics the theory of beams, which is also referred to as "beam theory" deals with objects where one dimension is much larger than the other two dimensions. One simple and useful theory is described by Euler and Bernoulli and is based on the following three assumptions: (1) "The cross-section is infinitely rigid in its own plane." (2) "The cross-section of a beam remains plane after deformation" (3) "The cross-section remains normal to the deformed axis of the beam."[17] This is valid for beams with lateral loads applied resulting in small deformations. The deflection of the beam u can be described by

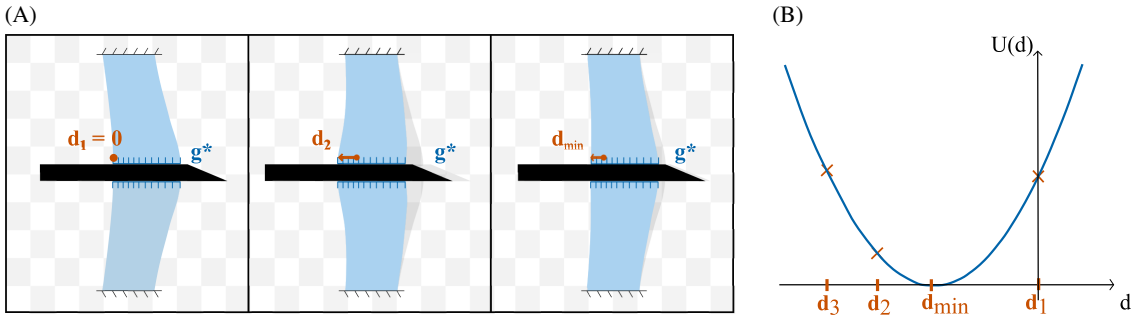

FIGURE 2 This is a 1D example of the relaxation process. After needle insertion the tissue sticks to the needle and therefore the relative displacement along the shaft $\boldsymbol{g}^*$ is constant. In order to find the equilibrium state of the needle-tissue system the deformation and thus the potential energy U are calculated for three different configurations. Two of these configurations are shown in (A) (left and middle) with constant additional displacements d_1 and d_2. Fitting a parabola in the d-U-plot and determining its vertex will give the equilibrium state at d_{min} (see (B)). The equilibrium state of the system with an additional deformation d_{min} is shown in (A) right.

$$\frac{d^2}{dx^2}\left(EI\frac{d^2u}{dx^2}\right) = q, \tag{7}$$

with the elastic modulus E, the second moment of area I, and the distributed load $q = q(x)$. When EI is constant this simplifies to

$$EI\frac{d^4u}{dx^4} = q. \tag{8}$$

After applying boundary, continuity, or symmetry conditions the beam's deflection can be calculated at position x.[18] The Euler–Bernoulli beam representing the needle in our system will be solved with an FE approach. Since deal.II does currently not support continuously differentiable finite elements, the system is rewritten as a pair of coupled Laplace equations with scalar Lagrange finite elements of degree three and five in each coordinate direction and the displacement solution is later interpolated linearly between the degrees of freedom. The biharmonic equation is therefore rewritten into a coupled pair of Laplace equations by defining $\omega = \partial_x^2 u$:

$$\begin{aligned} \omega - \partial_x^2 u &= 0 \\ EI\,\partial_x^2 \omega &= q. \end{aligned} \tag{9}$$

∂_x is the derivative in beam direction. The weak forms of the equations are obtained by multiplying test functions ψ and φ from the left and integrating over the domain. Partial integration leads to the following matrix equation

$$\begin{bmatrix} \left(\psi_i, \varphi_j\right) & \left(\partial_x\psi_i, \partial_x\psi_j\right) \\ -\left(EI\,\partial_x\varphi_i, \partial_x\varphi_j\right) & 0 \end{bmatrix} \begin{bmatrix} W_j \\ U_j \end{bmatrix} = \begin{bmatrix} 0 \\ (\varphi_i, q) \end{bmatrix}, \tag{10}$$

where we use the notation $(a,b) = \int_0^L ab\,dx$. The boundary terms $-[\psi\,\partial_x u]_0^L$ and $[EI\varphi\,\partial_x\omega]_0^L$ are implemented in the C++ finite element library deal.II[15] using so-called `FEFaceValues`. The boundary conditions are defined as follows: At $x = 0$ there is a simple support with $u|_{x=0} = 0$ and $\partial_x^2 u|_{x=0} = 0$. At $x = L$ the free end yields $\partial_x^2 u|_{x=L} = 0$ and $\partial_x^3 u|_{x=L} = 0$. In order to match the setup of a fixed template at x_0 in front of the tissue, there is an additional boundary condition $u|_{x=x_0} = 0$.

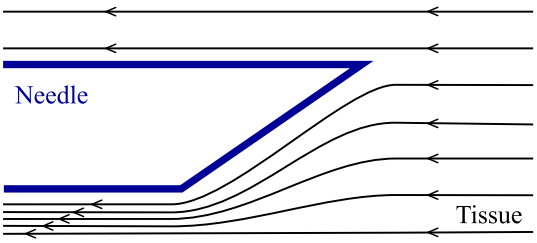

FIGURE 3 During needle insertion the beveled tip cuts the tissue asymmetrically and causes a compression of the tissue on one side of the tip. In this image the compression is below the needle resulting in a force pushing the needle upward.

2.3.2 | Bevel tip

In medical interventions such as brachytherapy needles with beveled tips are used. This allows for steering e.g. when the template holes do not align with the target position. The reason why a beveled tip results in bending of the needle is visualized in Figure 3. As the needle moves forward, the tissue is cut asymmetrically. In Figure 3 it is compressed on the lower side of the needle, while it stays uncompressed above the needle shaft. This results in a net force pushing the needle upward or more general in the direction of the bevel.[19] In the Euler-Bernoulli equation this tip force is added to the distributed load $q(x)$ at the first needle cell dropping linearly from q_{tip} to zero from the tip to the second degree of freedom.

2.4 | Needle–tissue interaction

The interaction between needle and tissue becomes more complex when the needle is flexible compared to a stiff needle. Since the Euler-Bernoulli equation only accounts for lateral displacement of the needle, its position in 3D space is defined with rods connected by joints. The number of rods is defined by the number of cells in the FE system and the position of the joints represent the position of the degrees of freedom. As visualized in Figure 4 an equilibrium state of the system is calculated when the needle is released as described in Section 2.2.2 and during insertion the following update steps are performed:

1. Move needle by distance d: Each needle joint is shifted by d along the rods' directions. Afterwards the directions are updated with the new joint positions.
2. Update tissue forces: The deformation of the tissue results in a tension force. This tension force is calculated from the current tissue deformation u_t, the previous tension force f_{t-1} and the stiffness matrix of the tissue K.

$$f_t = 2Ku_t - f_{t-1} \tag{11}$$

3. The calculated tension force acts on the needle. In order to be applied to the needle it is interpolated to its joints and the perpendicular component is extracted, because the Euler–Bernoulli beam only accounts for lateral forces. A tip force q_{tip} is added to the needle tip due to force resulting from the bevel tip angle explained in Section 2.3.2.
4. The Euler-Bernoulli beam equations (Equation (10)) are solved. Afterwards the lateral displacement of each needle joint is updated by the solution of the Euler–Bernoulli beam equations and the rods' directions are updated with the new joint positions.
5. The diffuse domain equation of the tissue (Equation (5)) is solved. The friction force parallel to the needle shaft is applied as traction boundary condition t to the tissue represented by the absolute gradient of the phase field function.

2.5 | Convergence analysis

For both the tissue and the needle equations, the convergence of the relative displacement errors are analyzed. It is defined as

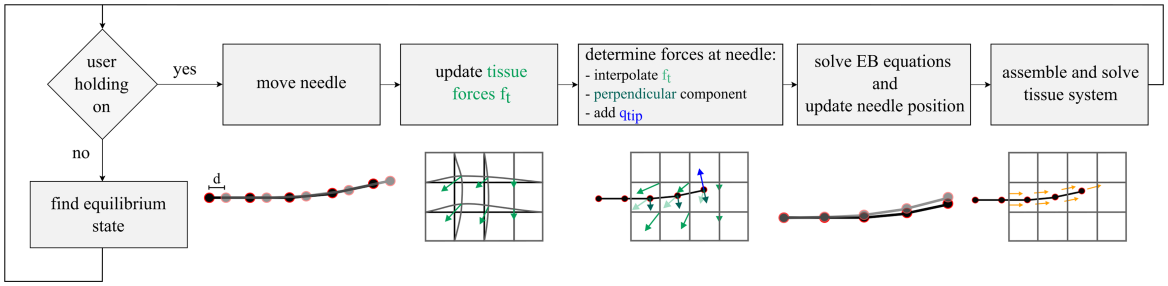

FIGURE 4 Update steps and their visualization for interaction between deformable needle and tissue.

$$d_x = \frac{|\boldsymbol{u} - \boldsymbol{u}_x|_{L2}}{|\boldsymbol{u}|_{L2}}, \tag{12}$$

where x is the parameter ε for the phase field convergence and the cell size h for mesh convergence. The numerical and the analytical solution are $\boldsymbol{u}_x$ and $\boldsymbol{u}$, respectively. The L2-norm is calculated by integrating over the corresponding domain $|\bullet|_{L2} = \int_{\Omega_0} \sqrt{\bullet^2}$ and the order of convergence p is determined by

$$\frac{d_x}{d_{\alpha x}} = \alpha^{-p} + O(x), \tag{13}$$

where α is the factor by which x is reduced.[20]

2.5.1 | Diffuse domain equations

In the diffuse formulation of the linear elastic tissue (Equation (4)) there are three phase field contributions: The phase field function ϕ for the distribution of the different tissue types, the absolute gradient of the phase field function $|\nabla\phi|$ for the traction boundary condition, and the two penalty terms multiplied by β for the application of Dirichlet boundary conditions. The convergence of the first two parts was shown in our previous work[3] and will therefore not be repeated.

The convergence of the penalty method for the diffuse application of Dirichlet boundary conditions is evaluated on the example of a 3D spherical thick shell with a radially displaced inner surface. We choose an inner radius $R_i = 50$, outer radius $R_a = 100$, elastic modulus $E = 10000$, Poisson's ratio $\nu = 0.3$, and $g = 0.2$. The analytic solution of the displacement in spherical coordinates is[21]

$$\sigma_r = -\frac{g}{\left(\frac{R_a}{R_i}\right)^3 - 1}\left[\left(\frac{R_a}{r}\right)^3 - 1\right], \tag{14}$$

$$\sigma_\phi = \sigma_\theta = \frac{g}{\left(\frac{R_a}{R_i}\right)^3 - 1}\left[\frac{1}{2}\left(\frac{R_a}{r}\right)^3 + 1\right], \tag{15}$$

$$u_r = \frac{r}{E}((1-\nu)\sigma_\theta - \nu\sigma_r). \tag{16}$$

The convergence rate of the relative deformation error due to the phase field approximation for the boundary's Dirac δ is analyzed for decreasing ε using Equation (13). In order to focus on the error of the phase field width, the grid has the same adaptive refinement around the shell boundary for all ε's. The factor α by which ε is reduced was chosen to be 1/1.3. Due to symmetry only an eighth of the sphere is simulated.

2.5.2 | Euler–Bernoulli beam equation

The displacement solution of the coupled Laplace equations for the Euler–Bernoulli beam (Equation (10)) is compared to the analytical solution for constant lateral load along the beam. The beam is clamped at $x=0$, so $u|_{x=0}=0$ and $\partial_x u|_{x=0}=0$ and the other end of the beam is free, thus $\omega|_{x=L}=0$ and $\partial_x \omega|_{x=L}=0$. The analytic solution is given by

$$u(x)=\frac{qx^2(6L^2-4Lx+x^2)}{24EI}. \tag{17}$$

We choose $q=1$, $EI=1$, and $L=8$ and analyze the convergence of the relative error of the resulting displacement for decreasing cell size h. In order to calculate the convergence rate p the cell size is reduced by a factor of $\alpha=1/2$.

2.6 | Phantom experiment for tuning and validation during needle insertion

The diffuse domain simulation of a flexible needle inserted into soft tissue is validated on a real-world experiment. The friction force between needle and tissue and the tip force of the needle are tuned and the deformation of the needle and the tissue are compared to the experiment.

2.6.1 | Phantom data

In order to validate the simulation of the needle insertion it is compared to a real-world phantom experiment recorded at Johns Hopkins University in 2005.[9] To the best of our knowledge this is the only data available which considers both needle and tissue deformation data during the insertion within one experiment. A bevel-tip needle of diameter 0.83 mm is inserted into a 11 cm × 11 cm × 3 cm[1] gel phantom. From compression tests the parameters of the tissue are determined to be $E=126\pm16$ kPa (Young's modulus) and $\nu=0.453\pm0.007$ (Poisson's ratio).[22] It is worth mentioning that the elastic parameters of prostate tissue differ between patients. However, the given values are a reasonable assumption for cancerous prostate tissue.[23,24] On the phantom's surface fiducial markers are placed to track the deformation. The video of the experiment can be found in the supplemental material of Chentanez et al.[9] In this real-world experiment, as in all others, the needle end is clamped and kept in position. The relaxation of the needle and the tissue which can occur during surgery due to remaining tension inside the tissue cannot be investigated with this data set.

Four images during the insertion of the needle are extracted from the video (see Figure 5). From these images marker positions and the needle are segmented manually. The deformation vector field at each marker is calculated by subtracting the rest position from the marker position of the deformed tissue. The needle is segmented as a polyline with approximately 15 points per cm.

2.6.2 | FEM simulation

The described experimental setup of the phantom experiment is rebuild as an FE model. The needle has a length of 20 cm and is split into 16 elements. A guidance (zero displacement) for the needle is placed in front of the tissue. The tissue is adaptively refined consisting of 372,352 cells. The refinement of the cells and the phase field function ϕ can be seen in Figure 6. The phase field function is one inside and zero outside the tissue domain, hence inside the needle. During step 3 in Section 2.4 the tissue deformation at the needle joints is needed. Since this is outside of the physical domain and there is no solution available at the surrounding vertices, the solution from the physical domain is interpolated tri-linearly to the region inside the needle for this task. The mean elastic tissue parameters of the compression experiment $E_T=126$ kPa and $\nu_T=0.453$ are used. The needle's elastic modulus is $E_N=180$ GPa, which is a typical value for stainless steel and the second moment of area is $I=9.8\cdot10^{-14}$ m^4.

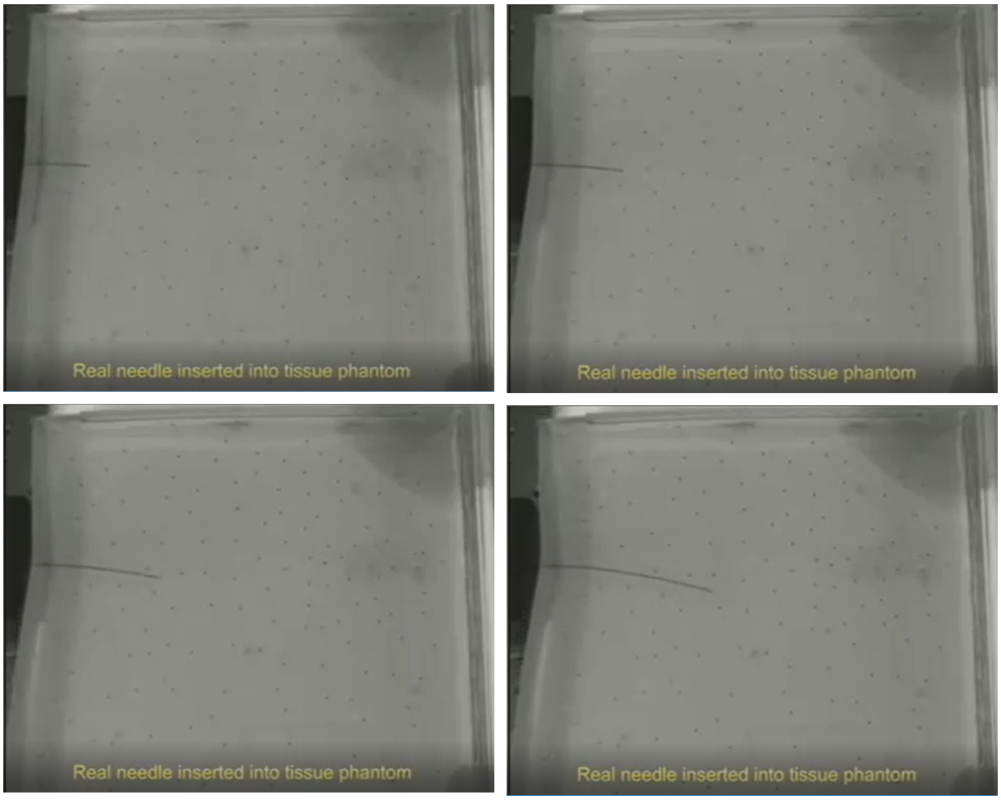

FIGURE 5 Needle insertion experiment at four different time steps.

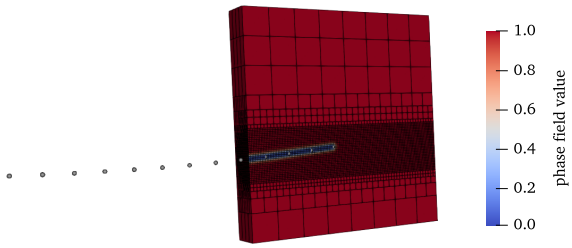

FIGURE 6 Setup of the FE simulation cut through the needle plane after the needle has been inserted. The color represents the phase field value, which is one inside the tissue and zero outside of the tissue domain. The black lines represent the cell boundaries, which are adaptively refined around the needle's path. In order to see the phase field well, the needle is only represented by its joints.

The deformation on the surface is extracted and projected to the x–y-plane. It is interpolated linearly to the scattered marker positions and afterwards a linear interpolation in time ensures that the needle insertion depth of the FE time-step corresponds to the insertion depth in the experiment. The needle is also projected to the x–y-plane. For each needle joint the distance to the experimental polyline is calculated using `p_poly_dist`.[25]

2.7 | Tissue and needle relaxation

In order to show the effect of the relaxation explained in Section 2.2.2 two experiments are performed. In both experiments a needle is inserted 57 mm into a tissue cuboid of 70 mm × 70 mm × 100 mm in z-direction and is

then released. According to Ji et al.[24] malignant prostate tissue has a mean elastic modulus of $E = (96 \pm 40)$ kPa. The elastic parameters of the pelvic floor are considered $\mu = 12.3$ kPa, which is the average shear modulus for different skeletal muscles, and $\nu = 0.493$ the Poisson ratio reported for relaxed muscle.[26]

In the first experiment the material is homogeneous prostate tissue with $E = 96$ kPa and $\nu = 0.453$. The shape of the bevel tip and therefore tip force is varied between different runs. In the second experiment the cuboid consists of two materials. For $0\,\text{mm} \leqslant z \leqslant 40\,\text{mm}$ the tissue is considered pelvic floor muscle and for $40\,\text{mm} < z \leqslant 100\,\text{mm}$ it is considered to be prostate. In order to get a smooth transitioning between elastic parameters the sharp boundary is filtered with a Gaussian kernel with sigma equal to 0.5 mm as performed in our previous work.[3] The elastic properties of the pelvic floor are constant throughout the experiment, while the elastic modulus of the prostate is varied within the range of one sigma from $E_{min} = 56$ kPa to $E_{max} = 136$ kPa.

3 | RESULTS

In this chapter the results of the convergence analyses for both the penalty method for the diffuse application of Dirichlet boundary conditions and the coupled Laplace equations for the Euler-Bernoulli beam are shown. We continue with the

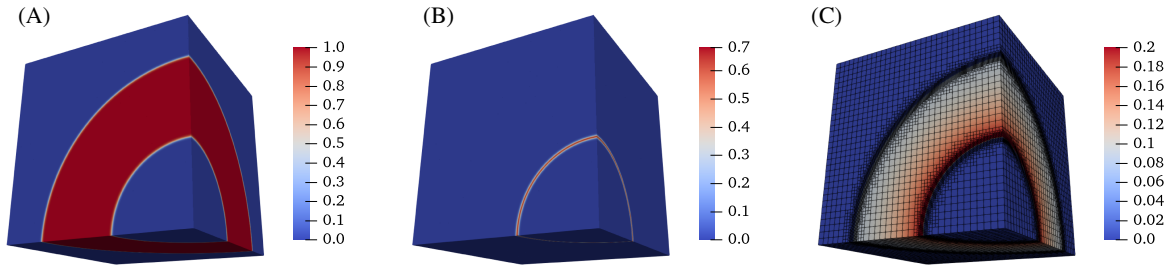

FIGURE 7 Phase field function (A), absolute gradient of the phase field for the inner surface (B), and magnitude of the deformation overlaid by the grid (C) for the a spherical thick shell and $\varepsilon = 2.2$.

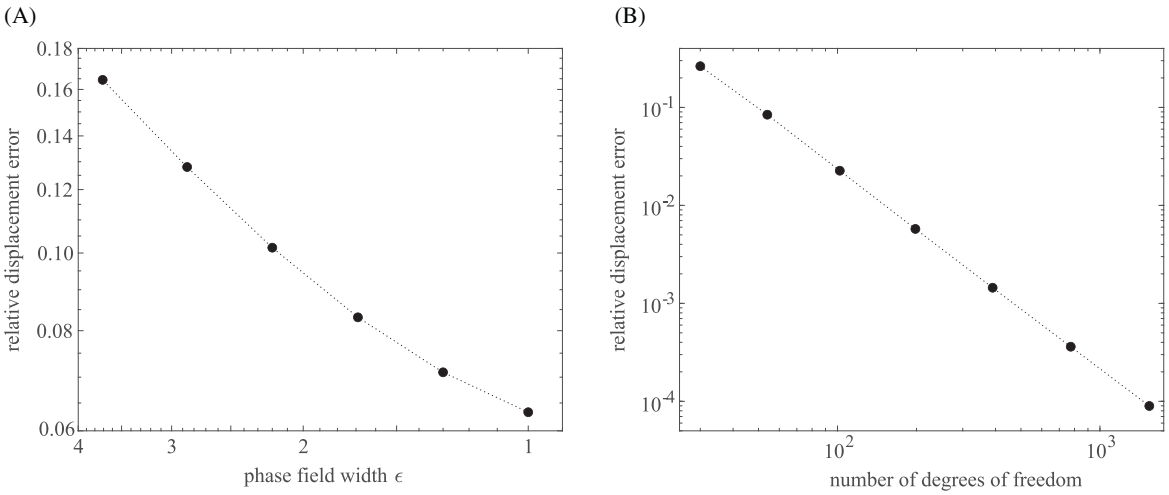

FIGURE 8 Convergence of the relative deformation error for (A) decreasing phase field width ε for the application of Dirichlet boundary conditions using the diffuse penalty method on the example of a spherical thick shell and (B) decreasing cell size for the coupled Laplace equations of the Euler–Bernoulli beam.

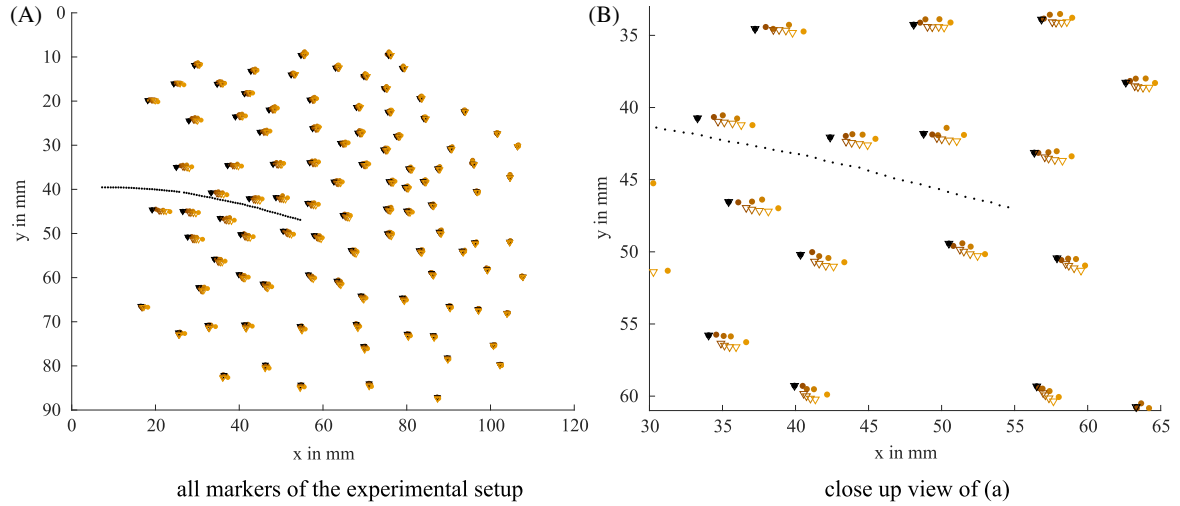

FIGURE 9 Marker positions for both the experiment (circles) and the simulation (triangles). The rest position is displayed in black. The four consecutive time steps are shown from brown to orange. The dotted line represents the needle path.

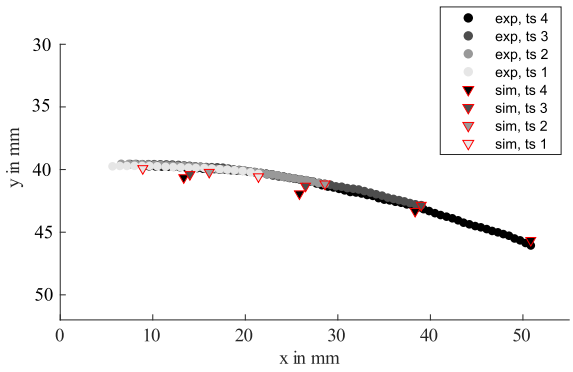

FIGURE 10 Needle position of both the experimental and simulated data for all time steps.

comparison to a real-world phantom experiment for needle insertion and the simulation results for the needle-tissue relaxation.

3.1 | Convergence analysis

3.1.1 | Penalty method for the diffuse application of Dirichlet boundary conditions

The phase field function ϕ (Equation (3)) which is one inside the thick shell and zero outside with a smooth phase field transitioning in between is shown in Figure 7A. The absolute gradient $|\nabla\phi|$ which is an approximation of the delta function for the inner surface is represented in Figure 7B. This is only the inner surface where the Dirichlet boundary condition is applied. The resulting deformation field is in radial direction and both its magnitude and the adaptively refined mesh are presented in Figure 7C. To understand the accuracy of the diffuse Dirichlet boundary conditions using the penalty method the deformation field is compared to its analytic solution (Equation (16)) for different phase field widths ε. The number of cells is 1,086,583 and there are 3,849,929 ($\approx 155^3$) degrees of freedom. The displacement error d_ε converges for decreasing ε with an average convergence rate of $p = 0.73 \pm 0.21$ (see Figure 8A).

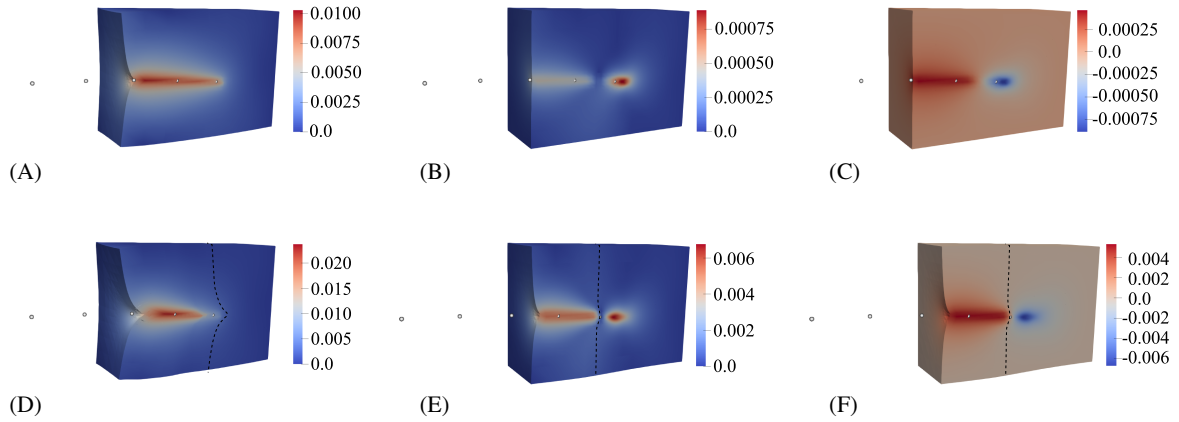

FIGURE 11 Magnitude of tissue deformation after needle insertion ((A) and (D)) and after relaxation ((B) and (E)) in m. (C) and (F) show the z component of the tissue deformation after relaxation. The top row is homogeneous prostate tissue with $E = 96$ kPa and a needle tip displacement of 4 mm after insertion. In the bottom row the dotted line shows the separation between pelvic floor tissue with $E = 36.7$ kPa on the left and prostate tissue with $E = 96$ kPa on the right. The needle is represented with white circles.

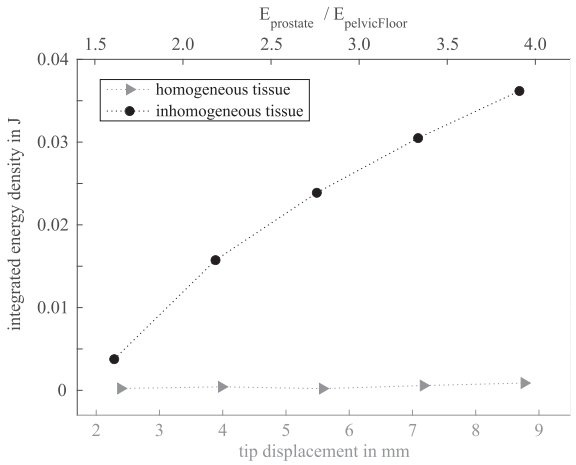

FIGURE 12 Energy density integrated over the domain after relaxation for needle insertion into homogeneous tissue with different needle tip forces and for inhomogeneous tissue with different elastic moduli for prostate tissue.

3.1.2 | Coupled Laplace equations for Euler–Bernoulli beam

Figure 8B shows the relative displacement error for increasing mesh refinement for the Euler–Bernoulli beam representation of the needle. The convergence rate is 1.92 ± 0.14.

3.2 | Needle insertion results and error estimation

Real-world experimental data is used to tune the parameters of the FE simulation and evaluate its performance. In order to estimate the uncertainty of the manual segmentation, the positioning of the markers is repeated. The positioning of 105 markers results in a mean error of (0.15 ± 0.08) mm. The result of the tissue and the needle deformation for the tuned parameters is shown in Figures 9 and 10. The marker positions of the real-world experiment are represented with circles and overlaid with the simulated positions shown as triangles for each time step. Around the needle, the

magnitude of the tissue deformation is largest with a maximal value of 4.3 mm. The deformation magnitude decreases with increasing distance to the needle. The mean and maximum error of the deformation magnitude are 0.52 mm and 1.53 mm, respectively. The root-mean-squared error is 0.56 mm. 97.5% of the errors are below 1 mm and 100% are below 2 mm. In Figure 10 the simulated needle points represented as triangles and the experimental needle position are shown. For $q_{tip} = 100$ N/m the maximal needle error has a value of 0.56 mm. The mean difference between the experiment and the simulation is 0.29 mm for an insertion depth of 50.9 mm and a deflection of 6.3 mm at the tip.

3.3 | Needle–tissue relaxation

The tissue deformation during the relaxation experiments for both the homogeneous tissue with a needle tip displacement of 4 mm and layered tissue with $E_{prostate} = 96$ kPa is shown in Figure 11. The deformation magnitude of the fully inserted needle in prostate tissue is shown in Figure 11A. When the needle is released by the physician and there is no more outer force acting on the needle the remaining tension inside the tissue relaxes and the needle is moved with the relaxing tissue (compare Figure 11B,C). In general the same behavior can be observed for inhomogeneous tissue (Figure 11 bottom row). In comparison the maximal deformation along the needle shaft is by a factor of two bigger in the softer muscle tissue. During relaxation the needle is therefore moved back by 17 mm compared to a shift of only 8 mm in homogeneous material for the shown tissue parameters. In Figure 12 the energy density integrated over the full tissue domain is shown for both experiments. It can be observed that independent of the needle tip, the remaining tension is small for homogeneous tissue. In comparison, the energy is by a factor of 8–78 larger for layered tissue and increases with increasing difference in the elastic moduli.

4 | DISCUSSION

The application of the diffuse domain approach to needle insertion FE simulations was extended by a flexible needle model and by the relaxation of the needle-tissue system after the physician releases the needle. The flexible needle is modeled as an Euler-Bernoulli beam and interacts with the tissue through interpolation of the forces. During relaxation the tissue sticks to the needle shaft and the potential energy inside the tissue is minimized by keeping the relative displacement along the shaft constant and varying the absolute displacement in each coordinate direction. These Dirichlet boundary conditions are included in the differential equation using the diffuse penalty method. The insertion of a clamped needle is validated on a real-world phantom experiment and the tissue deformation after relaxation is shown on two exemplary simulations.

With the introduced method the boundary condition is not explicitly defined on the surface of the mesh, but instead surface terms are approximated by the absolute gradient of the phase field function $|\nabla\phi|$ and thus transformed to volumetric terms of the differential equation. When implementing two interacting objects different approaches can be followed. A classical approach is to use two 3D meshes and determine their contact by collision detection. Deformation of the tissue can have an influence on this collision and constraints might change during the simulation. Furthermore, cutting a mesh remains a challenging task. Another option followed for needle insertion simulations is an angular spring model, which uses connected 1D rods.[4] During the insertion into tissue the interaction occurs at so called contact nodes, which are nodes of the tissue at the position of the needle shaft.[19] No tissue cutting, but instead a frequent remeshing of the tissue is required. This is not necessary in the introduced diffuse domain method. The 1D needle mesh and the 3D tissue mesh are independent and the interaction takes place through linear interpolation of the forces to the needle and implicit boundary parametrization of the tissue.

In order to validate the method of applying Dirichlet boundary conditions using the diffuse penalty method in our implementation, we performed a convergence analysis for decreasing phase field width ε. By using a fine resolution of the grid around the boundaries we make sure to be in the regime of the critical error level due to the length scale ε and that there is no significant contribution of the deformation error due to mesh refinement. We show that the displacement solution converges to the analytic solution when the phase field width ε goes to zero.

A real-world experiment including both the deformation of the tissue and the needle is used for validating the flexible needle-tissue model during needle insertion. The error of the tissue deformation is comparable to other state of the art methods.[9] It must be mentioned that the available deformation data is only 2D data since the markers are only placed at the surface of the gel phantom. This, however, is still a good tool to validate the method, because the

underlying tissue model is not a heuristic approach. Instead we use a constitutive law following a linear elastic differential equation for the description of tissue behavior, which depends on measured material properties. Due to a large parameter range between patients, the elastic properties of the corresponding tissues must be determined with a preliminary elastography for brachytherapy planning. Especially the effect of calcification inside the prostate on the elastic parameters is still to be studied. Effects such as anisotropy of the penetrated tissue types or a non-linear deformation response due to large deformations must be studied on real patient data. It must be mentioned that the introduced model can easily be extended to non-linear tissue models at the cost of higher computation times.

The second part of the model, which is the relaxation of the system after releasing the needle has, to the best of the authors' knowledge, not been discussed in literature so far. Both real-world phantom experiments[9,27,28] and needle insertion simulations[9,19] are usually performed with clamped needles leading to remaining tension inside the tissue, due to stick friction between the tissues and the needle shaft. When there is no external force of the clamping system this tension relaxes. During prostate brachytherapy multiple needles are inserted into the patient and afterwards radioactive seeds are applied to the prostate through those needle. To accurately model seed placement and the corresponding dose coverage, the relative position of the flexible needle inside the deformed tissue is of interest. In this article we therefore proposed the straight forward approach of minimizing the potential energy inside the tissue and thus solving for the final needle and tissue position. In homogeneous tissue and thus constant material properties along the needle shaft, the tissue relaxation leads to small remaining tension and deformation inside the tissue for various different tip displacements. Inhomogeneous tissue and thus varying elastic parameters result in different deformations along the needle shaft. Therefore both the remaining tension and the resulting deformation inside the tissue are larger after relaxation for increasing difference in elastic parameters. The preliminary simulations show a reasonable behavior, which now needs to be validated with real-world data.

Using the tissue deformation for medical simulators requires real time performance. This is not given with the current implementation. It must be mentioned that the diffuse domain approach requires fine meshes to resolve the phase field function around the boundaries, which goes along with high computation times. Even though real-time applications do not seem feasible, the advantage of this method is to easily allow patient-specific simulations without the need of time consuming and error-prone meshing and is therefore a valuable tool to be incorporated into surgical planning. The voxel-based tissue representation from the imaging modality can be directly used for the deformation simulation and the uncertainty of elastic parameters at tissue boundaries is directly incorporated through the width of the phase field function. Especially during brachytherapy, where the relative needle and tissue positioning is crucial for an optimal dose coverage, a patient-specific needle insertion simulation including relaxation can give prior knowledge about which seed placements are more sensitive compared to others.

5 | CONCLUSION AND OUTLOOK

In this article we firstly extend the diffuse domain method for medical needle insertion simulations by a flexible needle. Secondly, the relaxation of the needle-tissue system after the user releases the needle is simulated by minimizing the potential energy inside the tissue while it sticks to the needle shaft.

During needle insertion the deformation results of both the tissue and the needle using a diffuse domain method compare well to a real-world experiment of a needle insertion into a gel phantom. The simulation error is comparable to state of the art methods. As shown before, the possibility to use a voxel based tissue representation for the simulation allows easily implementable patient-specific simulations, because this is the tissue representation directly obtained from the imaging modality. This advantage has now been extended to simulate flexible needles with beveled tips, which are used during many surgical interventions.

Since needles are not clamped after insertion during most medical interventions, it is important to understand the relaxation of the system when the relative position between the needle and the deformed tissue is of interest. The plausibility of the proposed model was shown on two exemplary simulations. Comparing this model to real-world deformation data will be important to verify its usability. Since this work thoroughly explains the model, demonstrates the mathematical accuracy through convergence analyses and verifies the insertion process on a real-world phantom experiment, this is out of the scope of this article. As a next step we will compare the result of the relaxation model to ultra sound data of a needle insertion during prostate brachytherapy where the needle is released after insertion.

ACKNOWLEDGEMENTS

Katharina I. Jerg acknowledges support from the German Research Foundation through the grant HE 3011/36-1. All other authors declare that they have no conflicts of interest. Open Access funding enabled and organized by Projekt DEAL.

DATA AVAILABILITY STATEMENT

The data that support the findings of this study are openly available in ACM Digital Library at https://dl.acm.org/doi/10.1145/1576246.1531394. The code is openly available in Heidelberg Open Research Data at https://doi.org/10.11588/data/QYCZLB.

ORCID

Katharina I. Jerg https://orcid.org/0000-0002-8202-9936

ENDNOTE

[1] It must be mentioned that there are inconsistent values for the size of the phantom. The written publication states a size of 27.1 cm × 26.5 cm × 3.9 cm, whereas the video displays 11 cm × 11 cm × 3 cm. The latter is more reasonable, because this results in a needle width of about 1 mm instead of about 3 mm for the larger scaling. Therefore 11 cm × 11 cm × 3 cm is used as the phantom size.

REFERENCES

1. DiMaio SP, Salcudean SE. Needle insertion modeling and simulation. *IEEE Trans Robot Automat*. 2003;19(5):864-875.
2. Goksel O, Salcudean SE, DiMaio SP. 3D simulation of needle-tissue interaction with application to prostate brachytherapy. *Comput Aided Surg*. 2006;11(6):279-288.
3. Jerg KI, Austermühl RP, Roth K, et al. Diffuse domain method for needle insertion simulations. *Int J Numer Methods Biomed Eng*. 2020;36(9):e3377.
4. Goksel O, Dehghan E, Salcudean SE. Modeling and simulation of flexible needles. *Med Eng Phys*. 2009;31(9):1069-1078.
5. Lehmann T, Tavakoli M, Usmani N, Sloboda R. Force-sensor-based estimation of needle tip deflection in brachytherapy. *J Sens*. 2013;2013:1-10.
6. Misra S, Reed KB, Schafer BW, Ramesh K, Okamura AM. Mechanics of flexible needles robotically steered through soft tissue. *Int J Robot Res*. 2010;29(13):1640-1660.
7. Khadem M, Fallahi B, Rossa C, Sloboda RS, Usmani N, Tavakoli M. A mechanics-based model for simulation and control of flexible needle insertion in soft tissue. *IEEE Int Conf Robot Automat (ICRA) IEEE*. 2015;2015:2264-2269.
8. Yamaguchi S, Tsutsui K, Satake K, Morikawa S, Shirai Y, Tanaka HT. Dynamic analysis of a needle insertion for soft materials: arbitrary Lagrangian–Eulerian-based three-dimensional finite element analysis. *Comput Biol Med*. 2014;53:42-47.
9. Chentanez N, Alterovitz R, Ritchie D, et al. Interactive simulation of surgical needle insertion and steering. ACM SIGGRAPH *papers* 2009: 1–10. 2009.
10. Goksel O, Sapchuk K, Morris WJ, Salcudean SE. Prostate brachytherapy training with simulated ultrasound and fluoroscopy images. *IEEE Trans Biomed Eng*. 2012;60(4):1002-1012.
11. Kockelkoren J, Levine H, Rappel WJ. Computational approach for modeling intra-and extracellular dynamics. *Phys Rev E*. 2003;68(3):037702.
12. Schlottbom M. Error analysis of a diffuse interface method for elliptic problems with Dirichlet boundary conditions. *Appl Numer Math*. 2016;109:109-122.
13. Nguyen LH, Stoter SK, Ruess M, Sanchez Uribe MA, Schillinger D. The diffuse Nitsche method: Dirichlet constraints on phase-field boundaries. *Int J Numer Methods Eng*. 2018;113(4):601-633.
14. Li X, Lowengrub J, Rätz A, Voigt A. Solving PDEs in complex geometries: a diffuse domain approach. *Commun Math Sci*. 2009;7(1):81-107.
15. Arndt D, Bangerth W, Clevenger TC, et al. The `deal.II` library, version 9.1. *J Numer Math*. 2019;27:203-213. doi:10.1515/jnma-2019-0064
16. Curnier A, He QC, Zysset P. Conewise linear elastic materials. *J Elast*. 1994;37:1-38.
17. Bauchau OA, Craig JI. Euler-Bernoulli beam theory. *Struct Anal*. 2009;163:173-221.
18. Gere JM, Timoshenko SP. *Mechanics of Materials*. PWS; 1997.
19. Goksel O, Sapchuk K, Salcudean SE. Haptic simulator for prostate brachytherapy with simulated needle and probe interaction. *IEEE Trans Haptics*. 2011;4(3):188-198.
20. Runborg O. Lecture notes in Numerical Solutions of Differential Equations, Computer Science and Communication, KTH Royal Institute of Technology, Stockholm, Sweden. 2012 https://www.csc.kth.se/utbildning/kth/kurser/DN2255/ndiff13/ConvRate.pdf
21. Schillinger D, Evans JA, Frischmann F, Hiemstra RR, Hsu MC, Hughes TJ. A collocated c0 finite element method: reduced quadrature perspective, cost comparison with standard finite elements, and explicit structural dynamics. *Int J Numer Methods Eng*. 2015;102(3–4):576-631.

22. Chentanez N. Interactive simulation of surgical needle insertion and steering, PhD Thesis, UC Berkeley. 2010 https://escholarship.org/uc/item/2z09303w
23. Krouskop TA, Wheeler TM, Kallel F, Garra BS, Hall T. Elastic moduli of breast and prostate tissues under compression. *Ultrason Imaging*. 1998;20(4):260-274.
24. Ji Y, Ruan L, Ren W, et al. Stiffness of prostate gland measured by transrectal real-time shear wave elastography for detection of prostate cancer: a feasibility study. *Br J Radiol*. 2019;92(1097):20180970.
25. Yoshpe M. Distance from points to polyline or polygon. MATLAB Central File Exchange. 2022 https://www.mathworks.com/matlabcentral/fileexchange/12744-distance-from-points-to-polyline-or-polygon
26. Singh G, Chanda A. Mechanical properties of whole-body soft human tissues: a review. *Biomed Mater*. 2021;16(6):62004.
27. Abolhassani N, Patel R. Deflection of a flexible needle during insertion into soft tissue. 2006 *International Conference of the IEEE Engineering in Medicine and Biology Society* IEEE, 3858–3861. 2006.
28. Webster RJ, Memisevic J, Okamura AM. Design considerations for robotic needle steering. *Proceedings of the 2005 IEEE International Conference on Robotics and Automation* IEEE, 3588–3594. 2005.

How to cite this article: Jerg KI, Boggaram Naveen L, Kanschat G, Okonkwo ECN, Hesser JW. Diffuse domain approach for flexible needle insertion and relaxation. *Int J Numer Meth Biomed Engng*. 2023;e3782. doi:10.1002/cnm.3782

Publication III: Single Seed Placement Sensitivity in Low-Dose-Rate Prostate Brachytherapy

Title: Real-time Definition of Single Seed Placement Sensitivity in Low-dose-rate Prostate Brachytherapy

Authors: Katharina I. Jerg, Ernest Chukwudi N. Okonkwo, Frank A. Giordano, Yasser Abo-Madyan, Felix Momm, Jürgen W. Hesser

Journal: Brachytherapy

DOI: 10.1016/j.brachy.2023.10.006

Thesis Context: When including a deformation simulation into brachytherapy treatment planning we can estimate the uncertainty of needle and thus seed positions inside the tissue. It is yet unclear how much this seed misplacement influences the dose distribution in LDR brachytherapy. The next step is to determine how sensitive the dose parameters are with respect to seed placement. With this knowledge it is possible to adapt treatment plans in order to make them more robust.

Contribution to state-of-the-art: State-of-the-art LDR brachytherapy sensitivity analyses use statistical simulations based on seed displacement models and are performed offline to gain general knowledge about all seeds. In order for the analysis to be integrated into the planning procedure, we calculate the placement sensitivity for each individual seed by differentiating the dose parameter calculation. By including an automatic differentiation into the treatment planning software MatRad [64], we compute the gradients of each dose parameter with respect to the seeds' locations. This reveals the tolerance of the seed's placements without the need of an actual simulation of the placement variations. The results are assessed using 35 patient data sets and a potential visualization, which could be used in treatment planning systems is presented.

ARTICLE IN PRESS
JID: BRACHY [mNS;December 22, 2023;17:59]

ELSEVIER

BRACHYTHERAPY

Brachytherapy xxx (xxxx) xxx

Original Article

Real-time definition of single seed placement sensitivity in low-dose-rate prostate brachytherapy

Katharina I. Jerg[1,*], Ernest Chukwudi N. Okonkwo[1,2], Frank A. Giordano[3,4], Yasser Abo-Madyan[3], Felix Momm[2], Jürgen W. Hesser[1,5,6,7]

[1] *Mannheim Institute for Intelligent Systems in Medicine (MIISM), Heidelberg University, Mannheim, Germany*
[2] *Ortenau Klinikum Offenburg-Kehl, Department of Radiotherapy and Radiation Oncology, Offenburg, Germany*
[3] *Department of Radiation Oncology, University Medical Center Mannheim, University of Heidelberg, Mannheim, Germany*
[4] *DKFZ-Hector Cancer Institute at the University Medical Center Mannheim, Mannheim, Germany*
[5] *Interdisciplinary Center for Scientific Computing (IWR), Heidelberg University, Heidelberg, Germany*
[6] *Central Institute for Computer Engineering (ZITI), Heidelberg University, Heidelberg, Germany*
[7] *CZS Heidelberg Center for Model-Based AI, Heidelberg University, Mannheim, Germany*

ABSTRACT **PURPOSE:** In low-dose-rate brachytherapy, iodine-125 seeds are implanted based on a treatment plan, generated with respect to different dose constraints. The quality of the dose distribution depends on a precise seed placement, however, during treatment planning the impact on the dose parameters when certain seeds fail to be placed precisely is not clear. **METHODS AND MATERIALS:** We developed a method using automatic differentiation to calculate gradients of dose parameters with regard to the seeds' positions. Thus, we understand their sensitivity with respect to the seed placement. A statistical analysis is performed on a data set with 35 prostate brachytherapy patients. **RESULTS:** The most sensitive seeds regarding the dosimetric parameters of both rectum and urethra are close to the corresponding organ. Their gradient directions are mainly orthogonal to their surfaces. However, not all seeds close to the surface are equally sensitive with regard to the dose parameter. The most sensitive seeds regarding the prostate's dose parameters are distributed throughout the prostate and the direction of the gradients are mainly parallel to its surface. A linear regression with respect to different patient parameters shows that dose constraints which are barely fulfilled have large gradients and thus are additionally sensitive to misplacement. **CONCLUSION:** Automatic differentiation can be used to analyze dose parameter sensitivity with respect to seed placement. Integrating this into treatment planning systems is valuable as it speeds up the planning procedure, making it more robust and less dependent on user experience while showing the operating physician which needle placements require greater accuracy than others.

Keywords: Automatic differentiation; Low-dose-rate prostate brachytherapy; Seed placement; Dose objective; Sensitivity analysis

Introduction

In low-dose-rate (LDR) prostate brachytherapy, radiation is delivered through permanent implantation of radioactive seeds inside the prostate. A treatment plan is generated automatically or manually [1]. From the seed positions, the dose distribution is calculated from which a dose volume histogram is generated for each organ and is used for plan evaluation. In order for a plan to be accepted, certain organ constraints have to be met. Guidelines for those constraints are published in the AAPM [2] and the GEC-ESTRO ACROP prostate brachytherapy guidelines [3].

The operator's accuracy, tissue motion, or prostate swelling, among other human, mechanical, or biological factors, frequently result in the seeds not being placed exactly where they were planned [4]. Multiple studies analyzed how seed misplacement affects dosimetric parameters [4–9]. All of those studies vary the seeds' positions using an underlying displacement model, and they estimate the change in the dose distribution using a Monte-Carlo-

Received 3 August 2023; received in revised form 16 October 2023; accepted 16 October 2023; Available online xxx
* Corresponding author
E-mail address: katharina.jerg@medma.uni-heidelberg.de (K.I. Jerg).

1538-4721/$ - see front matter
https://doi.org/10.1016/j.brachy.2023.10.006

Please cite this article as: K.I. Jerg *et al.*, Real-time definition of single seed placement sensitivity in low-dose-rate prostate brachytherapy, Brachytherapy, https://doi.org/10.1016/j.brachy.2023.10.006

ARTICLE IN PRESS
JID: BRACHY [mNS;December 22, 2023;17:59]

like method. The seed displacement models range from straightforward Gaussian distributed random shifts [5] to more intricate models that incorporate both random seed displacement and seed collection-specific factors like seed train translation, needle divergence, curvature of the seed train, and more [4,9]. Although the experiments are designed similarly, the authors focus on different outcomes. According to Dawson et al., even small placement errors from the preplanned position can change the planned dose significantly [5]. Nath et al. state that the displacement between a needle image and its planned grid point at the base of the prostate should be kept less than 5 mm in order to ensure the desired dose coverage [8]. According to Su et al., implants with greater seed number and larger prostate volume correlate with less sensitivity of prostate's dose parameters to seed placement uncertainty. In contrast, the deviation of urethra's dose parameters do not correlate with the number of implanted seeds or prostate volume [7]. In order to improve the preplan's resistance to seed migration, Taschereau et al. use their simulation to identify the preplan's shortcomings and make necessary adjustments [4]. The relationship between seed activity and the robustness of seed placement is examined in numerous studies. In general robust plans can be generated for a wide range of seed activity, but plans become less robust to seed placement for high seed activities. On the other hand, high seed activities have the advantage of utilizing fewer seeds and needles, which reduces the surgical trauma to the patient [9,10]. The effect of a deviating seed orientation does not lead to statistically significant changes in the main clinical dose metrics [11,12].

In all of those simulations numerous dose calculations with varying seed positions are necessary to understand the robustness of the plan with regard to the seed placement. Calculating the derivatives of the dosimetric parameters with respect to the seeds' positions is, to the best of the authors' knowledge, a new approach to this topic. Regardless of the displacement model or foregoing simulations, it shows the sensitivity of each dose parameter to each individual seed placement. Understanding which seed placements have a larger effect on the outcome parameters has multiple advantages: During manual treatment planning, it can help the physicist to understand which seeds need to be placed differently in order to achieve the aimed objectives. At the same time it shows if there are seeds with high sensitivity, which could be re-planned in order to obtain robust plans. Also, it can give the operating physician an idea which needle placement require greater accuracy than others. This will speed up the planning process and the implantation procedure and make it less dependent on personal experience. We therefore introduce a method to investigate the dependence of each dose parameter on the accuracy of the placement of each seed using automatic differentiation.

This paper is organized as follows: In the next section, we describe the patient data used in this study, the used planning tool matRad [13] and the automatic differentiation algorithm integrated into matRad. After we explain the performed experiments the results are shown in section 3. The results are discussed in section 4.

Methods and materials

Patient data

In order to understand the dose parameters' change when seeds are misplaced we retrospectively use LDR treatment plans of 35 prostate brachytherapies performed at the department of radiotherapy and radiation oncology of the Ortenau Klinikum Offenburg-Kehl in Offenburg, Germany. For imaging the BK MEDICAL Pro-Focus 2202 Ultrasound system and the 8848 biplane transducer (BK Medical, Boston, MA) with a frequency of 9 MHz was used. The image data, the contoured structure sets and source locations were saved as DICOM-RT files. The seeds' reference air kerma rates were between 0.589 μGy/h at 1 m and 0.756 μGy/h at 1 m and the prostate volumes varied between 19.7 cm^3 and 71.4 cm^3 with a mean (std) of 33.6(11.1) cm^3. The seed model is the STM1251 manufactured by Bard Brachytherapy, Inc., Carol Stream, IL. The treatments were performed between November 2016 and September 2020 and the target dose for the target volume was 160 Gy. The dose constraints are shown in Table 1.

Dose calculation tool

For dose calculation we used matRad [13,14], an open source software for radiation treatment planning for research and educational purposes written in MATLAB. It is mainly designed for external photon, proton, and carbon ion therapy, but was extended to LDR brachytherapy planning using the TG-43 dose calculation algorithm [15,16] with the approximation of a 1D point source. It is worth mentioning that the introduced method is independent of the source model and can also be applied to different models.

Automatic differentiation

Automatic differentiation, or also called algorithmic differentiation, is a tool which is used in areas including computational fluid dynamics, atmospheric sciences, computational finance, and recently it has gained more attention in deep learning [17]. By converting a function into a graph and employing the chain rule to combine the derivatives of successive operations, it can calculate numerical derivatives. The computational graph of a function $f(x_1, x_2) = x_1 \exp(-\frac{1}{2}(x_1^2 + x_2^2))$ with intermediate variables $v_{-1} \ldots v_5$ is shown in Fig. 1. There is a *forward accumulation mode*, in which the derivative of a function f with respect to the first input variable x_1, $\partial f / \partial x_1$, is calculated by setting $\partial x_1 / \partial x_1 = 1$ and $\partial x_i / \partial x_1 = 0$ for all other input variables.

Please cite this article as: K.I. Jerg *et al.*, Real-time definition of single seed placement sensitivity in low-dose-rate prostate brachytherapy, Brachytherapy, https://doi.org/10.1016/j.brachy.2023.10.006

ARTICLE IN PRESS
JID: BRACHY [mNS;December 22, 2023;17:59]
K.I. Jerg et al. / Brachytherapy xxx (xxxx) xxx 3

Table 1
Dosimetry constraints in LDR prostate brachytherapy.

Organ	Parameter	Requirement
Prostate	P_D90	Minimum dose received by 90% of the prostate volume should be greater than 90% of the prescribed dose
	P_V100	Prostate volume receiving 100% of the prescribed dose should be greater than 95%
	P_V150	Prostate volume getting 150% of prescribed dose should be between 45% and 65%
Urethra	U_D10	Dose to 10% of urethra should be less than 150% of the prescribed dose
	U_D30	Dose to 30% of urethra should be less than 130% of the prescribed dose
Rectum	R_D2cc	Dose to 2cc of rectum should be less than 145 Gy
	R_D0.1cc	Dose to 0.1cc of rectum should be less than 200 Gy
	R_V100	Rectum volume getting 100% of prescribed dose (Reporting parameter)

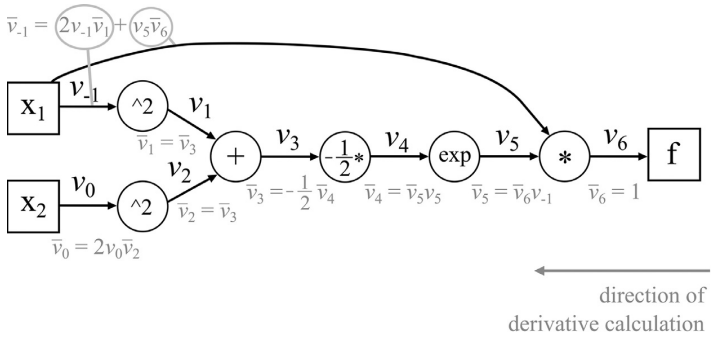

Fig. 1. Computational graph for a function $y = f(x_1, x_2) = x_1 \exp(-\frac{1}{2}(x_1^2 + x_2^2))$ and its automatic differentiation in reverse accumulation mode. v_i are the intermediate variables and the derivative of the output with respect to v_i is denoted by $\bar{v}_i = \partial y / \partial v_i$.

Then $\partial v_i / \partial x_1$ is iteratively calculated for the intermediate variables through the graph. For each input variable x_i a separate evaluation is needed. In contrast it is possible to calculate the derivatives with respect to all input variables in one pass using the *reverse accumulation mode*. Here the code is first run forward keeping track of all intermediate variables v_i and afterward the derivative values $\partial y / \partial v_i$ are propagated from the outputs to the inputs as shown in Fig. 1. The interested reader is referred to [17] for a more detailed explanation.

Corresponding to the exemplary exponential function, the dose parameter calculation can be converted into a computational graph. The input parameters of the graph are the seed positions, from which a dose distribution, dose volume histograms, and finally dose parameters are calculated. By using automatic differentiation and such applying the chain rule to elementary derivatives, the gradients of the output with respect to the input parameters can be calculated without the need for numerical approximations. In order to calculate gradients of the dose parameters with respect to the position of each seed, the automatic differentiation of MATLAB's deep learning toolbox [18] is employed in the reverse accumulation mode.

Experiments

The organs' segmentations and planned seed positions are imported from the DICOM-RT files and a dose calculation including the automatic differentiation is performed with matRad for four different dose parameters: the prostate volume receiving at least 100% of the target dose (P_V100), the minimal dose received by 90% of the prostate (P_D90), the minimal dose received by the hottest 2 cm^3 of the rectum (R_D2cc), and the minimal dose received by the most irradiated 30% of the urethra (U_D30). Thus, gradients of those parameters are calculated with respect to the position of each seed. In order to investigate the calculated gradients, three evaluations are performed: *Gradient magnitude visualization* We exemplarily show bull's eyes derived from the gradient magnitudes for three dose parameters of two different patients in a 3D view. The size of the targets indicate the allowed placement positions around the seeds. Seeds with large gradients are more sensitive to misplacement and therefore have small bull's eyes. Additionally, a 2D view which can be integrated into a treatment planning system is presented. Here, the bull's eyes overlay a transversal ultrasound (US) image. *Statistical analysis over all patients* A statistical analysis regarding the *sensitive seeds* is performed. For each dose parameter the *sensitive seeds* are defined as the seeds with the largest 5% in gradient magnitude $|\partial y / \partial \boldsymbol{x}|$. Their distribution is compared to the distribution of *all seeds* using MATLAB's two sample *t*-test `ttest2`. The null hypothesis is that the samples stem from normal distributions with equal means. If the test rejects the null hypothesis p is the significance level by which the test is rejected. A significance of less than 1% is considered to be statistically significant for the distribution of the seed positions and

Please cite this article as: K.I. Jerg *et al.*, Real-time definition of single seed placement sensitivity in low-dose-rate prostate brachytherapy, Brachytherapy, https://doi.org/10.1016/j.brachy.2023.10.006

ARTICLE IN PRESS
JID: BRACHY [mNS;December 22, 2023;17:59]

gradient directions. At first the distribution of the *sensitive seeds* between patients is investigated, followed by seed positions and gradient directions of the *sensitive seeds* in relation to the organs' surfaces. *Relationship between seed gradients and patient parameters* We want to analyze if there is a relationship between given parameters like reference air-kerma rate, prostate size, or the value of the dose parameter and the gradient magnitude of the seeds between different patients. In this experiment all seeds of all patients are considered. A linear regression of the median gradient magnitude of each patient regarding the three parameters is performed using MATLAB's `fitlm`. This is an iteratively reweighted least squares algorithm in order to perform robust fitting reducing the effect of outliers.

Results

Gradient visualization

We show a possible representation of the gradients for three different dose parameters (P_D90, U_D30, and R_D2cc) in Fig. 2. For seeds with large gradients only small deviations of the positions are allowed to assure the pursued dose coverage. In Fig. 2, the seed is shown in black surrounded by a bull's eye with a radius of

$$R = 1.5 \times \frac{1}{|\partial y / \partial \boldsymbol{x}|} \tag{1}$$

where y is a dose parameter and $\boldsymbol{x}$ is the seed position. The 3D spheres are shown as 2D discs for better visibility. It must be mentioned that the constant parameter of this equation is chosen arbitrarily. This work introduces the newly developed gradient calculation method, while an analysis on the relation to actual displacement values must be performed next. Bull's eyes with a radius of more than 5 *mm* around seeds are not shown. Instead those seeds are colored in green, because the plan is rather robust to a misplacement of those seeds.

The visualizations of the two patients show that seeds which are sensitive with respect to U_D30 and thus have small bull's eyes are close to the urethra (compare Figs. 2e and f) and sensitive seeds regarding R_D2cc are close to the rectum (see Figs. 2c and d). However, it must be mentioned that not all of the seeds in the vicinity of the OAR are equally relevant for the corresponding dose parameters. There are also seeds close to the respective OAR to which the dose parameter is not highly sensitive to. In Fig. 2b, it can be observed that the gradients vary greatly between the different seeds for P_D90 in this treatment plan. While the seeds close to the rectum are colored in green and thus have a large misplacement tolerance, the ventral seeds have bull's eyes in the range of the seed's size and therefore there is no tolerance for seed misplacement. Such a plan can be considered not robust and could be improved when this information was accessible at the time of planning.

During seed placement, the dose parameters are not considered separately, but instead a placement sensitivity of each seed with respect to all dose parameters is relevant for the clinician. We therefore show an accumulated sensitivity with respect to the three shown dose parameters. In Fig. 3 the bull's eye's radius is calculated by

$$R = 3 \times \frac{1}{\sum_y |\partial y / \partial \boldsymbol{x}|} \tag{2}$$

where the gradient magnitudes of the different dose constraints y are summed in the denominator. As in Eq. 1 the scaling constant of this equation is arbitrarily chosen and can be investigated thoroughly in further work. Additionally to the scaling factor, a weight could be added for each dose parameter in order to weight dose objectives differently. In Fig. 3a, the blue plane shows the position of the US image of Fig. 3b. The bull's eyes overlaying the US image are a suitable visualization method to help the clinician understand whether the seed is placed within the allowed bound.

The computation time of the gradients of all seeds in 1 patient is $0.86\,s \pm 0.32\,s$.

Statistical analysis over all patients

In this section, we show the results concerning the analyses of the *sensitive seeds* such as their distribution between patients, the positions within the prostate and their gradient directions relative to the organs' surfaces.

Distribution between patients

Figure 4 shows histograms for the number of *sensitive seeds* per patient regarding different dose parameters. It can be observed that for P_D90, R_D2cc, and U_D30 most patients have 3 *sensitive seeds* with a distribution between 0 and 6 (5 for R_D2cc). The distribution of *sensitive seeds* for P_V100 differs from the remaining distributions. There are two patients where 16 and 21 seeds are considered most sensitive, while 14 patients have zero *sensitive seeds*. This is due to the fact that the gradients vary greatly between patients. Plans with large gradients are more sensitive to a misplacement of the seeds and therefore less robust regarding the seed placement.

Position of sensitive seeds

The distance to the organs' surfaces is calculated for each seed. For each organ boxplots are generated for all seeds of all patients and additionally for the *sensitive seeds* of each dose parameter. For each parameter, we investigate the statistical significance whether the distribution of *sensitive seed* positions is different compared to the distribution of all seeds. In Fig. 5, the signs correspond to the following p-values: o: $p > 0.01$, *: $p < 0.01$, **: $p < 0.001$, ***: $p < 0.0001$.

In Fig. 5a, we can observe that there is no significant difference in the distance to the prostate's surface of all

Please cite this article as: K.I. Jerg *et al.*, Real-time definition of single seed placement sensitivity in low-dose-rate prostate brachytherapy, Brachytherapy, https://doi.org/10.1016/j.brachy.2023.10.006

ARTICLE IN PRESS
JID: BRACHY [mNS;December 22, 2023;17:59]
K.I. Jerg et al. / Brachytherapy xxx (xxxx) xxx 5

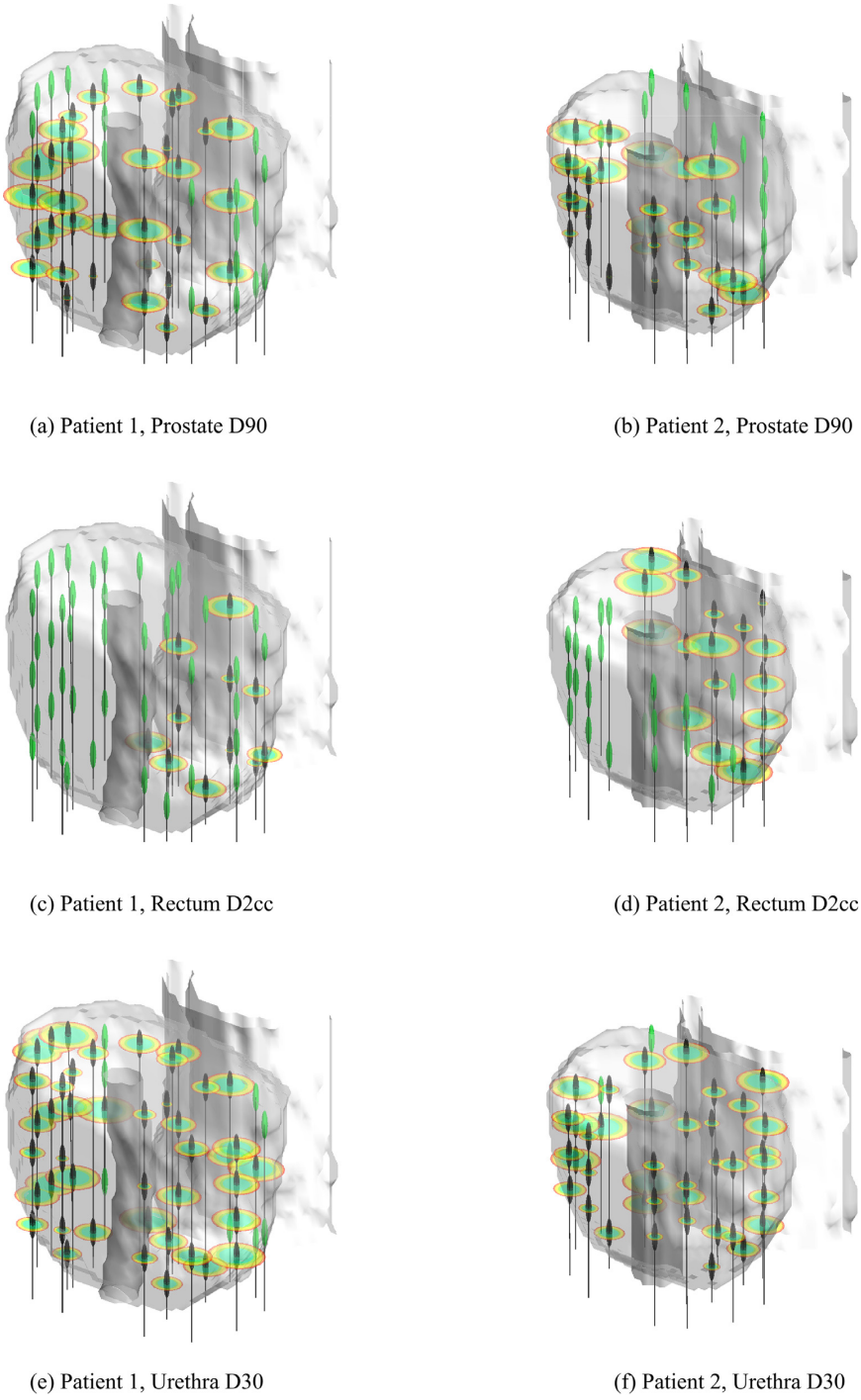

(a) Patient 1, Prostate D90

(b) Patient 2, Prostate D90

(c) Patient 1, Rectum D2cc

(d) Patient 2, Rectum D2cc

(e) Patient 1, Urethra D30

(f) Patient 2, Urethra D30

Fig. 2. Gradient magnitudes visualized as bull's eyes around the black seed for different dose parameters in two exemplary patients. The seeds are surrounded by transparent surfaces of the organs. Bull's eyes with a radius of more than 5 *mm* are not shown. Instead those robust seeds are colored in green. (For interpretation of the references to colour in this figure legend, the reader is referred to the web version of this article.)

Please cite this article as: K.I. Jerg *et al.*, Real-time definition of single seed placement sensitivity in low-dose-rate prostate brachytherapy, Brachytherapy, https://doi.org/10.1016/j.brachy.2023.10.006

ARTICLE IN PRESS
JID: BRACHY [mNS;December 22, 2023;17:59]
6 K.I. Jerg et al. / Brachytherapy xxx (xxxx) xxx

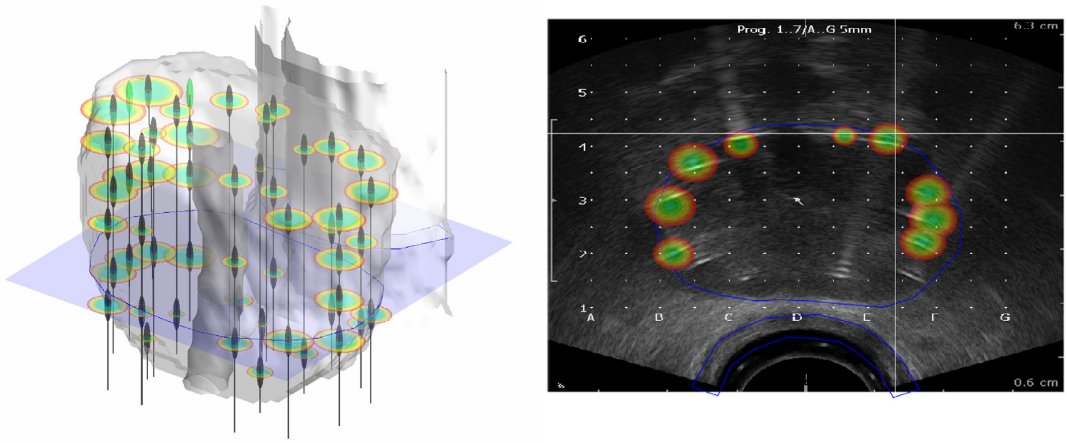

(a) (b)

Fig. 3. Accumulated gradients of all dose parameters in 3D (a) and corresponding 2D US slice as it could be shown in a treatment planning system (b). The position of the US slice inside the 3D volume is shown in blue. (For interpretation of the references to colour in this figure legend, the reader is referred to the web version of this article.)

seeds and the *sensitive seeds* regarding all four dose parameters. The distance to both the rectum and the urethra is not significantly different to all seeds for the *sensitive seeds* of P_D90 (see Figs. 5b and c). For P_V100 ($p < 0.0001$) and U_D30 ($p < 0.0001$, the *sensitive seeds* are further away from the rectum and therefore ventral seeds are more sensitive. The *sensitive seeds* for R_D2cc ($p < 0.0001$) are closer to the rectum compared to all seeds and thus located dorsal. In Fig. 5c, it can be observed that the *sensitive seeds* for R_D2cc have a larger distance to the urethra, while the *sensitive seeds* for P_V100 and U_D30 are closer to the urethra compared to all seeds ($p < 0.0001$).

Gradient direction

For every *sensitive seed,* the closest point to each surface is determined. The gradient of each dose parameter is split into a component towards the closest point, which is the gradient component orthogonal to the surface, and its component parallel to the surface. Boxplots are generated for each dose parameter and the parallel and orthogonal gradient components towards each organ surface are compared. For each parameter we investigate the statistical significance between the two directions using the same notation as before. In Fig. 6b, we can observe that there is no preferred direction of the P_V100 gradients regarding the urethra. Concerning the prostate's ($p < 0.0001$) and the rectum's ($p < 0.01$) surfaces the parallel components of the P_V100 gradients are larger compared to the orthogonal components. For the prostate this can also be observed for the P_D90 gradients with $p < 0.0001$ in Fig. 6a. There is no preferred direction of the P_D90 gradients in relation to the rectum's surface, while the gradients are larger parallel to the surface of the urethra. The gradients of the dose parameters regarding the two organs at risk, R_D2cc and U_D30, in Figs. 6c and d follow a coherent behavior: the motion toward the corresponding OAR, which is the rectum for R_D2cc and the urethra U_D30, has a larger gradient component compared to the direction parallel to the OAR with $p < 0.0001$. There is no dominant gradient direction regarding the other OAR or the prostate for both cases.

Relationship between the seed gradient and patient parameters

Partial regression plots or also called added variable plots as in Fig. 7 and Fig. A1 show the effect of adding a variable to the regression problem and therefore the influence of each parameter to the model. Each blue cross corresponds to one patient. A fitted horizontal line indicates that there is no relationship between the given variable and the y-value, while a steep slope indicates a strong relationship. The 95% confidence bounds obtained with MATLAB's `plotAdded` are shown as dotted lines.

In Fig. 7, the added variable plots for the median gradient magnitude of P_D90 and R_D2cc with respect to three parameters are shown. The fits for P_V100 and U_D30 have lower R-squared values and are therefore shown in Fig. A1 in the appendix. Figure 7a shows that for P_D90 there is no relationship between the median gradient magnitude and P_D90 itself. For increasing reference air-kerma rate the gradient magnitude and thus the sensitivity of P_D90 with respect to seed placement increases. In contrast increasing prostate volume results in smaller gradient magnitudes. The model is significant with a p-value of

Please cite this article as: K.I. Jerg *et al.*, Real-time definition of single seed placement sensitivity in low-dose-rate prostate brachytherapy, Brachytherapy, https://doi.org/10.1016/j.brachy.2023.10.006

ARTICLE IN PRESS
JID: BRACHY [mNS;December 22, 2023;17:59]
K.I. Jerg et al. / Brachytherapy xxx (xxxx) xxx 7

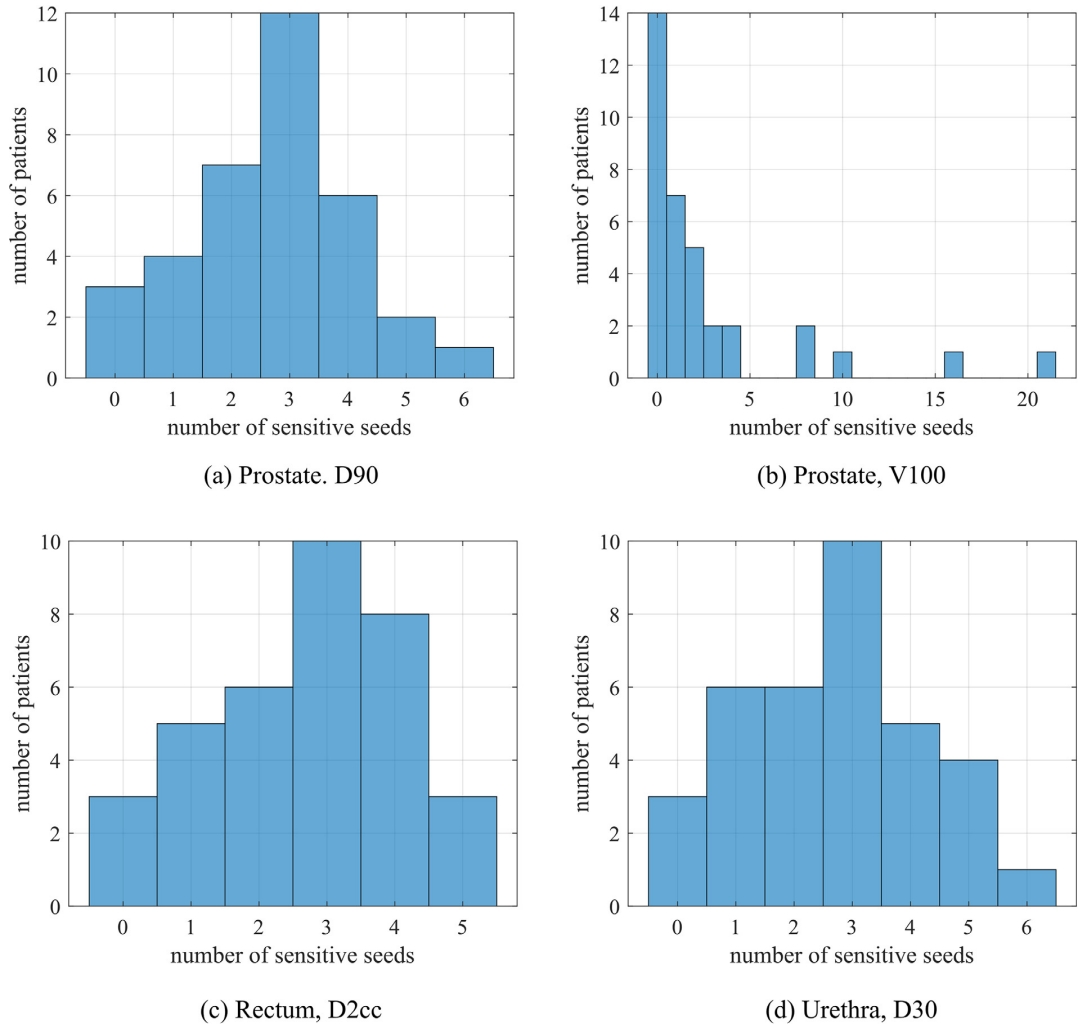

Fig. 4. Number of *sensitive seeds* per patient.

1.33e-07 and has a coefficient of determination of 66.9%. For the rectum's dose parameter, R_D2cc, in Fig. 7b, there is no relationship between its median gradient and the reference air-kerma rate. Here, the gradient magnitude decreases for increasing prostate volume. On the other hand the median gradient magnitude is larger when R_D2cc is large itself. The model has a coefficient of determination (R-squared) of 66.4% with a significance of 1.7e-07 (*p*-value).

Discussion

In this work, the gradients of the dose parameters with respect to the seeds' positions are calculated using automatic differentiation. Even though the current implementation is in the treatment planning tool MatRad, this approach could be easily transferred to any commercial LDR brachytherapy treatment planning system. Determining the gradient of a certain parameter with respect to the seeds' positions is a linear approximation of how the dose parameter changes when the seed is misplaced. This is therefore a measure of the sensitivity of the dose distribution regarding the different seed positions. One limitation of the suggested approach is that the gradient, being a linear approximation, only accounts for displacements close to the current position. This can be regarded as a local sensitivity that ignores potential alternate solutions located further away from the present placement. The advantage that the sensitivity of each seed is determined separately and thus we obtain a tolerance for each individual seed, comes with the disadvantage that an interplay between seed misplacements is not considered in the current model.

Please cite this article as: K.I. Jerg *et al.*, Real-time definition of single seed placement sensitivity in low-dose-rate prostate brachytherapy, Brachytherapy, https://doi.org/10.1016/j.brachy.2023.10.006

ARTICLE IN PRESS
JID: BRACHY [mNS;December 22, 2023;17:59]
8 K.I. Jerg et al. / Brachytherapy xxx (xxxx) xxx

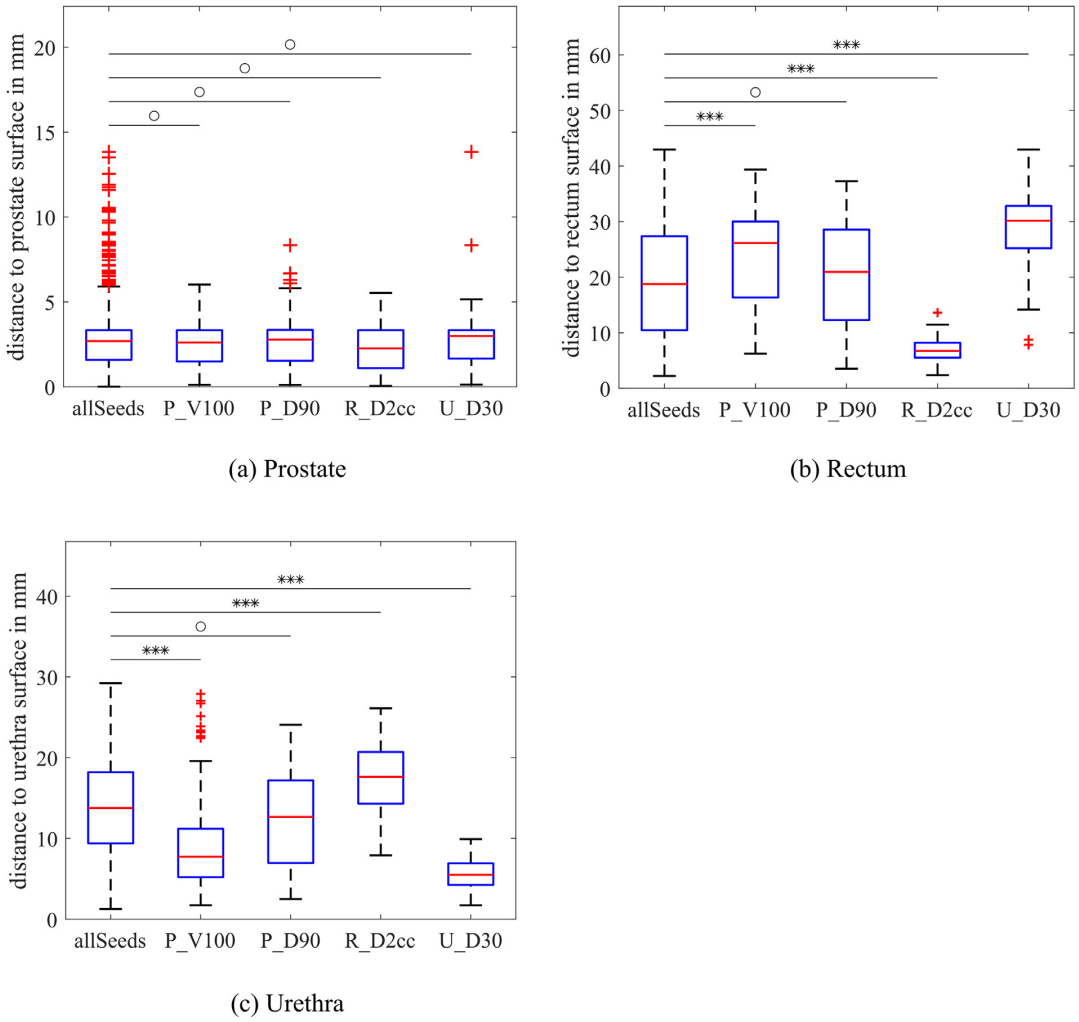

Fig. 5. Distance to (a) the prostate, (b) the rectum, and (c) the urethra for the *sensitive seeds* of the different dose parameters compared to the distances of all seeds.

While statistical seed displacement models and the dose calculations thereon consider the effect of moving all seeds at the same time, the gradient calculation implies that the remaining seeds are in their foreseen position. The impact of this effect must be evaluated further. In this work, the magnitude of the gradients and their directions are statistically analyzed between patients. The relationship between the sensitivity of the seed positioning and different patient parameters is investigated and a potential visualization method of the gradient magnitudes in treatment planning systems is exemplarily shown.

Gradient visualization. The gradient magnitudes of the seeds are represented as bull's eyes of the allowed placement region for two patients as a 3D view. Additionally, a 2D representation of the bull's eyes is shown which can be integrated into a treatment planning system. Using an inverse relation between the gradient magnitude and the radius of the tolerance bound is reasonable due to the fact that the gradient is a linear approximation of the dose parameter's change. The parameter of the function, which describes not only the relative tolerances between the seeds, but instead the absolute allowed displacement per seed must be determined in follow up work. There are two stages during an LDR treatment where this gradient visualization can improve the process: (1) During manual treatment planning it is a common procedure to consecutively change seed positions in order to determine their effect to both the target and the OAR, which is a time-consuming trial and error method. Adding the bull's eyes for the desired dose parameter can be a good indication

Please cite this article as: K.I. Jerg *et al.*, Real-time definition of single seed placement sensitivity in low-dose-rate prostate brachytherapy, Brachytherapy, https://doi.org/10.1016/j.brachy.2023.10.006

ARTICLE IN PRESS
JID: BRACHY [mNS;December 22, 2023;17:59]
K.I. Jerg et al. / Brachytherapy xxx (xxxx) xxx 9

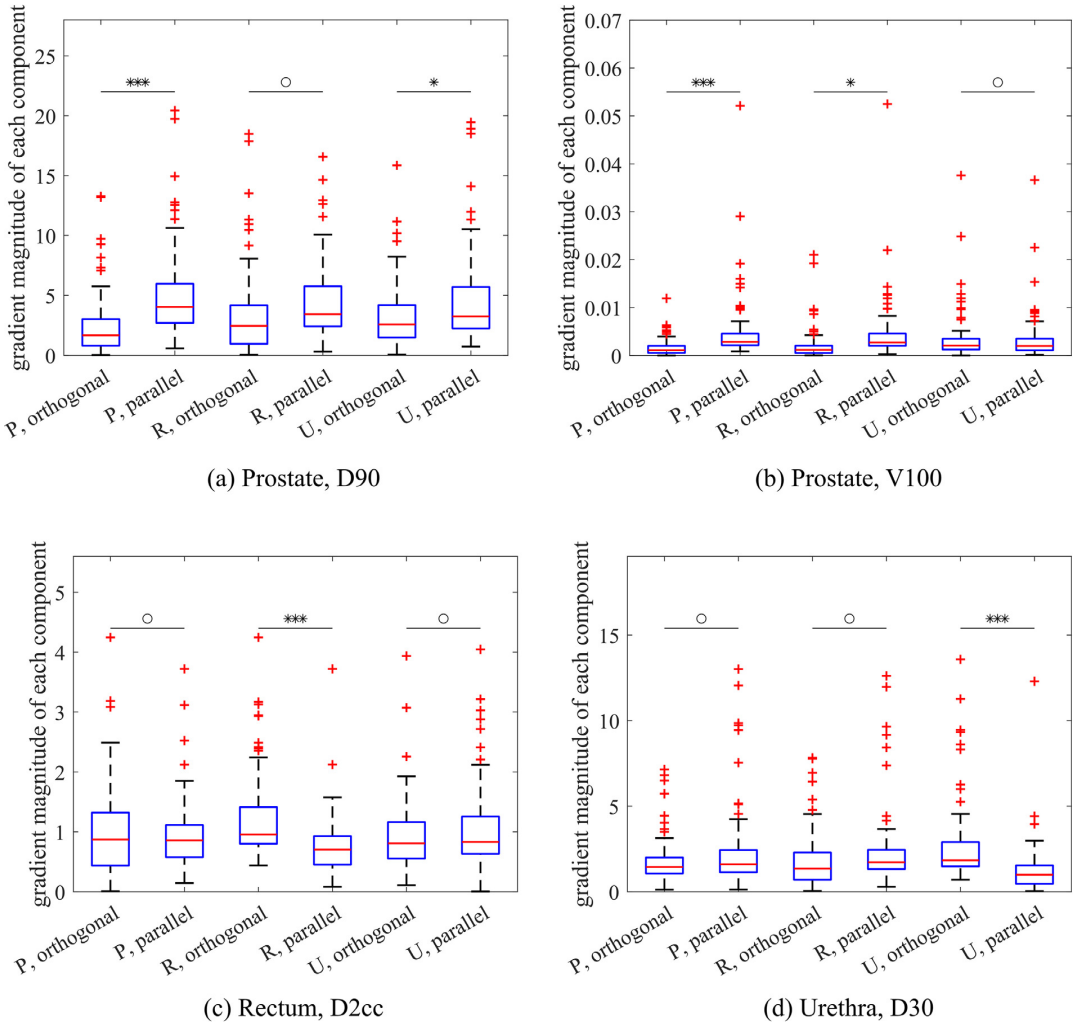

Fig. 6. Gradients of the *sensitive seeds* for each dose parameter split into parallel and orthogonal component with respect to the prostate's (P), the rectum's (R), and the urethra's (U) surface.

of which seeds have a large influence when moved and therefore need to be adjusted during manual planning. The introduced approach is universal and not limited to the presented dose parameters. It is possible to visualize the sensitivity of any wanted dose parameter. During treatment planning it is additionally possible to identify seeds with a low placement tolerance and plans can be adjusted such that the seeds become less sensitive to misplacement. This can help inexperienced physicists to generate high quality and more robust treatment plans and become faster in treatment plan generation. The computation time of less than a second will not be a limitation during treatment planning. *(2)* The procedure can benefit from the gradient visualization during needle placement. Knowing where the *sensitive seeds* are can help the operating physician to understand which needles have to be placed more precise than others. It becomes clear which needles may need repositioning due to small tolerances and for which needles a misplacement can be tolerated. Since placed needles fixate the prostate, it can make the placement of the following needle more accurate. This knowledge could therefore influence the order of needle placements.

Statistical analysis over all patients. The gradients for P_V100 differ much between patients, which means that in some plans the gradients of P_V100 are very large compared to the other patients. In these plans, a shift of the seed position greatly changes the volume which is covered with 100% of the target dose. Therefore, these patients are likely to have cold spots in their final dose distribution. If this information is available during planning it is reason-

Please cite this article as: K.I. Jerg *et al.*, Real-time definition of single seed placement sensitivity in low-dose-rate prostate brachytherapy, Brachytherapy, https://doi.org/10.1016/j.brachy.2023.10.006

ARTICLE IN PRESS
JID: BRACHY [mNS;December 22, 2023;17:59]
10 K.I. Jerg et al. / Brachytherapy xxx (xxxx) xxx

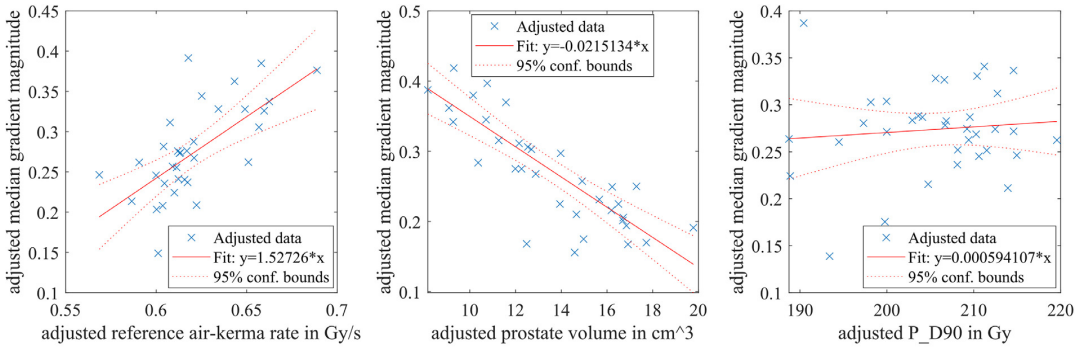

(a) Prostate, D90. R-squared = 0.669.

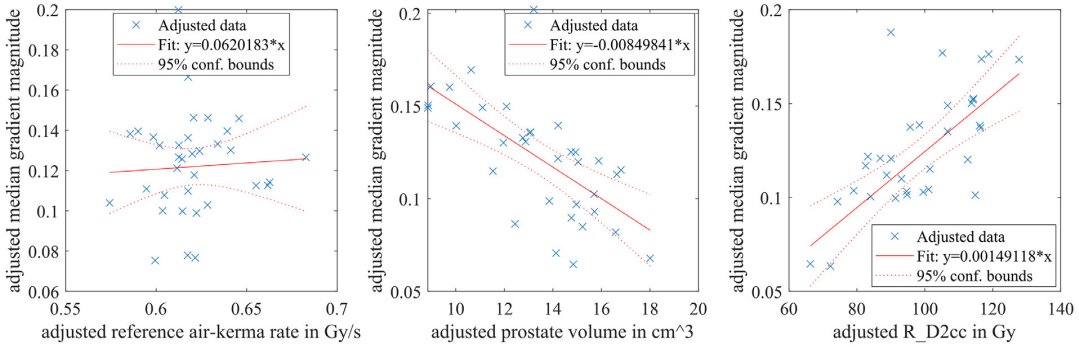

(b) Rectum, D2cc. R-squared = 0.664

Fig. 7. Added variable plots for a linear regression of the median gradient magnitude of each patient versus the three different parameters reference air-kerma rate, prostate volume, and variable value for P_D90 and R_D2cc.

able to improve the plan for less placement sensitivity and thus more robustness of the plan. While this was also suggested by Taschereau et al. [4], no foregoing simulations are necessary with our method, but instead the sensitivity calculation can be directly integrated into the dose calculation.

When looking at the position of the *sensitive seeds*, it is reasonable, that the *sensitive seeds* for R_D2cc are close to the rectum and the *sensitive seeds* for U_D30 are near the urethra. It is worth mentioning that the *sensitive seeds* for the prostate's dose parameters are not close to the prostate's surface, but instead they have the same distance to the surface as all the other seeds inside the prostate.

For the OAR, the gradient orthogonal to the corresponding organ is larger than the parallel component. This means that moving the seed towards or away from the OAR will have a larger effect on the parameter compared to moving it along the organ's surface, which agrees with common sense. This is not the case for P_V100 nor for P_D90. Here, the component parallel to the prostate's surface is larger compared to the orthogonal component. This correlates with the fact that the *sensitive seeds* are not close to the surface, but instead distributed equally within the prostate. Therefore, a change in those dose parameters is less about the confinement of the outer isodose lines with the prostate's surface, but rather about creating cold spots inside the prostate.

According to Nath et al. [8], a misplacement of less than 5 *mm* at the needle base is the desired outcome. As in all other studies, in [8] a statistical analysis was performed with a displacement of all seeds, while to the best of the authors' knowledge this is the first work to investigate the seed sensitivity separately for each seed. We demonstrate that the gradients of the different dose parameters vary significantly between seeds, making some needle placements more sensitive than others. A deviation of much less than 5 *mm* may be required for some needles, whilst a wider tolerance may be acceptable for others.

Relationship between the seed gradient and patient parameters. Analyzing the relationship between the gradient

Please cite this article as: K.I. Jerg *et al.*, Real-time definition of single seed placement sensitivity in low-dose-rate prostate brachytherapy, Brachytherapy, https://doi.org/10.1016/j.brachy.2023.10.006

ARTICLE IN PRESS
JID: BRACHY [mNS;December 22, 2023;17:59]
K.I. Jerg et al. / Brachytherapy xxx (xxxx) xxx 11

magnitude and different parameters can help to get a better understanding of the influence of single seeds for upcoming patients. In general it can be said that there is either no or an inverse relation regarding the gradient magnitude and size of the prostate. For small prostates the seed placement is more sensitive compared to larger prostates, which agrees with the findings of Su et al. [7]. For the OAR large dose parameters have large gradients, while for the prostate there is no relation between P_V100 and P_D90 and their gradients. Since we are trying to minimize R_D2cc and U_D30 this indicates that dose constraints of the OAR, which are barely fulfilled are additionally highly dependent on the seed placement and therefore easy to be missed. Constraints which are over-fulfilled are less dependent on the correct seed placement in two respects: First the gradients are smaller and thus the effect of a misplacement will be smaller, and second a change of the dose parameter will not as easily miss the constraint. From this result, it can therefore be suggested that it is reasonable to generate treatment plans which over-fulfill the constraints if possible. Larger seed activities lead to less robust plans with respect to R_D90 similar to [9].

Conclusion and Outlook

Automatic differentiation can be used to analyze the sensitivity of a dose parameter regarding the seed placement. To the best of the authors' knowledge this is the first work to investigate the placement sensitivity through a direct gradient calculation instead of running numerous simulations with statistical seed displacements. This direct calculation can be valuable to be integrated into planning systems for three reasons: First, it can speed up manual planning and make it less dependent on the experience of the treatment planner. Second, it can be used to generate plans which are robust against misplacement of the seeds. And third, it shows the operating clinician where the *sensitive seeds* are and which needle placements require more accuracy than others.

The introduced approach is not limited to the presented dose parameters, but also gradients of other parameters can be investigated with the current implementation. Additionally, the concept can be extended to other LDR brachytherapy targets or high-dose-rate brachytherapy. As a next step it would be valuable to perform an analysis which connects the gradients to actual displacement values.

Data accessibility

We are making the code and data associated with this paper available under https://doi.org/10.11588/data/Y3KIPM when published.

Disclosures

K.I. Jerg was supported by the German Research Foundation [grant number HE 3011/36-1] and was supported for travel from the Medical Faculty of the University of Heidelberg. J.W. Hesser acknowledges support from the German Research Foundation through the grant HE 3011/36-1. F.A. Giordano has received research grants from Elekta AB, grants, stocks, support for attending meetings, consulting fees, and equipment from TME Pharma AG, grants from Guerbet SA, grants, consulting fees and support for attending meetings from Carl Zeiss Meditec AG, consulting fees from Cureteq AG and Novocure, honoraria from AstraZeneca and Medac GmbH, and support for attending meetings from Varian. All other authors declare that they have no conflicts of interest.

Declaration of generative AI and AI-assisted technologies in the writing process

During the preparation of this work, the authors used QuillBot AI in order to improve language and readability. After using this tool, the authors reviewed and edited the content as needed and take full responsibility for the content of the publication.

Supplementary material

Supplementary material associated with this article can be found, in the online version, at doi:10.1016/j.brachy.2023.10.006

Appendix

Please cite this article as: K.I. Jerg *et al.*, Real-time definition of single seed placement sensitivity in low-dose-rate prostate brachytherapy, Brachytherapy, https://doi.org/10.1016/j.brachy.2023.10.006

ARTICLE IN PRESS
JID: BRACHY [mNS;December 22, 2023;17:59]
12 K.I. Jerg et al. / Brachytherapy xxx (xxxx) xxx

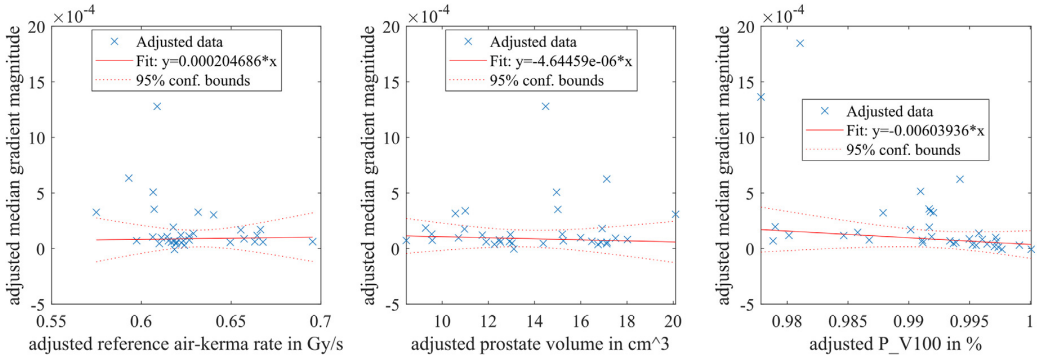

(a) Prostate, V100. R-squared = 0.396.

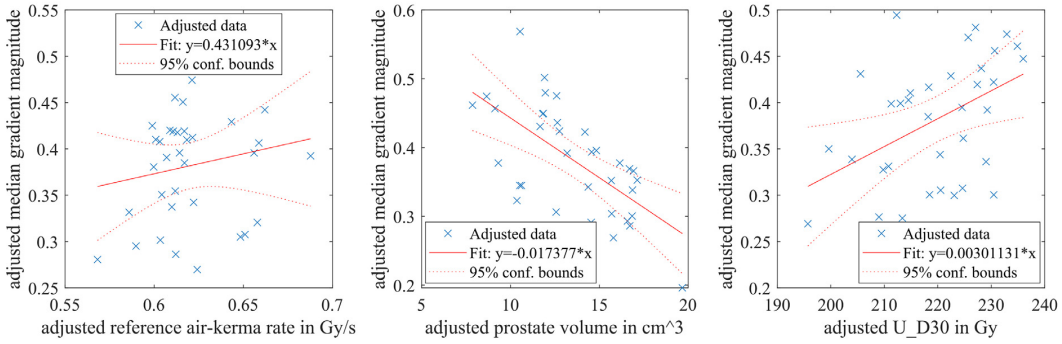

(b) Urethra, D30. R-squared = 0.508.

Fig. A1. Added variable plots for a linear regression of the median gradient magnitude of each patient versus the three different parameters reference air-kerma rate, prostate volume, and variable value for P_V100 and U_D30.

References

[1] Zelefsky MJ, Zaider M. Low-dose-rate brachytherapy for prostate cancer: preplanning vs. intraoperative planningintraoperative planning is best. *Brachytherapy* 2006;5(3):143–144.

[2] Nath R, Anderson LL, Luxton G, et al. Dosimetry of interstitial brachytherapy sources: recommendations of the aapm radiation therapy committee task group no. 43. *Med Phys* 1995;22(2):209–234.

[3] Henry A, Pieters BR, Siebert FA, et al. Gec-estro acrop prostate brachytherapy guidelines. *Radiother Oncol* 2022;167:244–251.

[4] Taschereau R, Roy J, Pouliot J. Monte carlo simulations of prostate implants to improve dosimetry and compare planning methods. *Med Phys* 1999;26(9):1952–1959.

[5] Dawson J, Wu T, Roy T, et al. Dose effects of seeds placement deviations from pre-planned positions in ultrasound guided prostate implants. *Radiother Oncol* 1994;32(3):268–270.

[6] Gao M, Wang J, Nag S, Gupta N. Effects of seed migration on post-implant dosimetry of prostate brachytherapy. *Med Phys* 2007;34(2):471–480.

[7] Su Y, Davis BJ, Furutani KM, et al. Dosimetry accuracy as a function of seed localization uncertainty in permanent prostate brachytherapy: increased seed number correlates with less variability in prostate dosimetry. *Phys Med Biol* 2007;52(11):3105.

[8] Nath S, Chen Z, Yue N, et al. Dosimetric effects of needle divergence in prostate seed implant using and radioactive seeds. *Med Phys* 2000;27(5):1058–1066.

[9] Beaulieu L, Archambault L, Aubin S, et al. The robustness of dose distributions to displacement and migration of 125i permanent seed implants over a wide range of seed number, activity, and designs. *Int J Radiat Oncol Biol Phys* 2004;58(4):1298–1308.

[10] Bues M, Holupka EJ, Meskell P, Kaplan ID. Effect of random seed placement error in permanent transperineal prostate seed implant. *Radiother Oncol* 2006;79(1):70–74.

[11] Corbett J, Jezioranski J, Crook J, et al. The effect of seed orientation deviations on the quality of 125i prostate implants. *Phys Med Biol* 2001;46(11):2785.

[12] Collins Fekete C-A, Plamondon M, Martin A-G, et al. Quantifying the effect of seed orientation in postplanning dosimetry of low–dose-rate prostate brachytherapy. *Med Phys* 2014;41(10):101704.

[13] M. Bangert, matrad. https://github.com/e0404/matRad, Accessed April 21, 2023.

[14] Wieser H-P, Cisternas E, Wahl N, et al. Development of the open-source dose calculation and optimization toolkit matrad. *Med Phys* 2017;44(6):2556–2568. doi:10.1002/mp.12251.

[15] Rivard MJ, Coursey BM, DeWerd LA, et al. Update of aapm task group no. 43 report: a revised aapm protocol for brachytherapy dose calculations. *Med Phys* 2004;31(3):633–674.

Please cite this article as: K.I. Jerg *et al.*, Real-time definition of single seed placement sensitivity in low-dose-rate prostate brachytherapy, Brachytherapy, https://doi.org/10.1016/j.brachy.2023.10.006

[16] Rivard MJ, Venselaar JL, Beaulieu L. The evolution of brachytherapy treatment planning. *Med Phys* 2009;36(6Part1):2136–2153.
[17] Baydin AG, Pearlmutter BA, Radul AA, Siskind JM. Automatic differentiation in machine learning: a survey. *J Mach Learn Res* 2018;18:1–43.
[18] Automatic differentiation in deep learning toolbox, (https://de.mathworks.com/help/deeplearning/ug/include-automatic-differentiation.html). Accessed June 7, 2023.

Please cite this article as: K.I. Jerg *et al.*, Real-time definition of single seed placement sensitivity in low-dose-rate prostate brachytherapy, Brachytherapy, https://doi.org/10.1016/j.brachy.2023.10.006

4 Discussion

In this thesis two methods are developed, which can transition LDR prostate brachytherapy treatment planning from a static, geometry based planning towards a simulation-based planning, which incorporates knowledge about placement uncertainties and plan robustness. The first implementation is a simulation of a flexible needle being inserted into soft tissue without the need for creating boundary conforming meshes. This offers a possibility to include patient-specific simulations into treatment planning in order to predict critical needle placements and estimate uncertainties in advance. The second implementation, which is the integration of automatic differentiation of the dose parameters, offers a tool to evaluate the sensitivity due to seed movement and therefore plan robustness directly during treatment planning. In the following the potential and limitation of both methods are discussed in more detail and an outlook for further developments is given. Afterwards the clinical relevance which can be expected when including the methods into existing LDR brachytherapy treatment strategies is elaborated.

4.1 Diffuse domain needle insertion simulation

The potential, limitations, and outlook of the first two publications with regard to simulation-based LDR prostate brachytherapy treatment planning are presented in the following.

4.1.1 Potential

The benefit of embedded domain methods is the simple and fast mesh generation. Structured Cartesian grids can easily be generated and there is no alignment to curved boundaries necessary. Additionally there is no need to have matching mesh boundaries between the different tissues. We use the application of boundary conditions in a diffuse sense and such the uncertainty of the volume segmentation can be directly translated to the width of the phase field. In an automated pipeline probability maps from the segmentation algorithm in a voxel representation can be directly used as tissue distributions in the simulation. In the first publication [44], where the diffuse domain method for needle insertion simulations is introduced, HDR is mentioned as a possible application, however, it is also applicable to LDR brachytherapy needles.

In publication I CT data of the liver is consulted. It is shown that it is possible to use automatically segmented tissue probability maps as geometric information to define elastic parameters for the simulation. During an LDR brachytherapy session TRUS data is

obtained for treatment planning. Even though there are automated segmentation methods for TRUS prostate images [65, 66], during LDR treatment planning the segmentation of the prostate and the OARs are nowadays still obtained manually. Thus no probability maps are available, but instead there is a discrete distribution of the different tissue types, meaning each voxel is assigned to exactly one tissue type. In order to apply the diffuse boundary conditions an artificial uncertainty can be defined by filtering the image with a Gaussian kernel, similar to the validation experiments in publication I. While this is not a real segmentation uncertainty, this method can be utilized until automated segmentation methods are used in a clinical routine in the future. Recent developments on uncertainty estimation of prostate ultrasound segmentation using deep learning [67] can give elaborate options for automated image segmentation and an uncertainty measure for reasonable tissue probability maps. This can serve as input to the introduced simulation method in the future.

Due to reduced computation times we approximate the tissue motion with linear elasticity for small deformations. The introduced diffuse domain method can also be applied to more complex tissue models including non-linear elasticity. Large deformations of soft tissue are better described with isotropic non-linear elastic models such as Ogden's law [68] or Mooney-Rivlin [69], which comes with the cost of larger computation times.

Needle deflection can be described by finite element methods (FEM) using triangular elements, FEM using nonlinear beam elements, or an angular spring model. [70] Since our approach is to move away from boundary conforming tetrahedral meshing and additionally beam elements are expected to be more suitable to model beam-like structures such as needles [31], a 1D Euler-Bernoulli beam model is considered to model needle deflection. This is the case in many other needle insertion experiments [71, 72, 73, 74] and offers the possibility to calculate the beam deflection given an applied load to the shaft. The disadvantage of not accounting for longitudinal compression [70] is not crucial for the given application.

In literature there are different needle-tissue interaction types such as a constant friction coefficient [75], velocity-dependent sliding friction force [76], or stick-slip friction models [77, 30]. We implemented the simplest model which is a constant sliding friction along the needle shaft during insertion. There is only one parameter, which needs to be tuned for the sliding friction and the resulting deformation field compares well to the phantom experiment. Puncture forces are measured [78], but do not have an effect on the resulting tissue deformation after the puncture has been performed. Since we are interested in the tissue deformation and resulting seed position and not the forces, as it is

the case for haptic feedback in medical simulators, this was omitted. After the needle has been inserted and the relative velocity between the needle and the tissue becomes zero, the tissue is assumed to stick to the needle along the entire shaft.

During LDR brachytherapy multiple needles are inserted into the prostate before they are loaded with seeds. Compared to phantom experiments where the needles are clamped in the insertion tool [79, 30], they are released by the physician in the real setup. When the needle is clamped outside the tissue and the tissue sticks to the needle due to static friction there is a remaining tension inside the tissue. To the best of the author's knowledge this has not been investigated in literature so far even though this relaxation can be seen in first needle insertion ultrasound experiments. A model was developed which incorporates the relaxation process into the simulation in order to get a full understanding of the relative needle tissue positioning during the surgery. The introduced model is based on the assumption that the tissue sticks to the needle shaft, which is reasonable due to zero relative motion after needle insertion. The potential energy inside the tissue is minimized and the corresponding position of the needle is determined. First experiments show that the remaining energy inside the tissue is larger for inhomogeneous tissue, due to different tissue deformations along the needle shaft. While parameter tuning of the dynamic friction and the force of the beveled needle tip are needed to get a reliable insertion simulation, there are no parameters in the relaxation process. The stability of the relaxation depends on the choice of needle positions for the minimization of the quadratic potential function. Needle positions which result into a stable solution are presented in the publication II for reasonable tissue parameters. This is therefore not a limiting factor of the model.

Having patient-specific elastic needle insertion simulations available has two advantages: First, the simulations can be used beforehand for a statistical analysis on the robustness of the system and to define critical steps during the insertion. An analysis with random variation of parameters can give an estimate of expected needle displacements. Second, the simulation can estimate insertion paths during the procedure and hint the physician to take action in order to reach the desired target (e.g. rotate the needle). Due to the clinician's prior knowledge, real-time path estimate is not necessary for medical treatments carried out by humans. However, it is indispensable during automated needle insertion using robots, which makes real-time computations necessary. The implemented simulation therefore brings us closer to simulation-based brachytherapy treatment planning.

4.1.2 Limitation

Real-time simulations are necessary to integrate simulations into the clinical routine. This, however, is not given with the current implementation. Having to resolve the phase field function requires fine meshing along the boundaries, which results in a large number of cells and such degrees of freedoms. A pre-computation of the stiffness matrix could highly decrease the computation time, but as the needle moves through the tissue the phase field values change throughout the volume and such a pre-computation is not possible.

A second limitation regarding patient-specific simulations is the fact that elastic parameters deviate greatly between patients. Ji *et al.* report a standard deviation of 42% of the mean Young's modulus for prostates with malignant lesions [80]. To perform reliable patient-specific simulations an elastography is needed before the simulation. In order to omit this additional session, another possibility is to start the simulation with default parameters and estimate the tissue parameters in real-time during insertion utilizing the tissue and needle deformation obtained from the TRUS.

There are additional factors which introduce uncertainties into the dose distribution and are not considered in the current simulation. Effects such as seed migration due to swelling or bleeding of the prostate [81] are not accounted for in the simulation. The effect of seed migration after the implantation can be limited by using stranded seeds, but still takes place during or after procedures [11, 12].

4.1.3 Further developments

As a next step we work on the validation of the relaxation model on real world ultrasound data of a needle which is inserted into soft tissue and then released. It is important to understand if stick friction long the entire shaft and the approximation of a quadratic potential is sufficient to describe the relaxation process. Multiple needle insertions will be used to tune the unknown tissue parameters during the insertion. Additional experiments will allow to estimate the errors of both the needle position and the tissue deformation field after the relaxation.

Implementing needle-tissue deformation simulations inside a clinical routine requires real-time performance. As discussed before this is not feasible with the current implementation, but can be approached using physics informed neural networks [82] (PINNs). Compared to the traditional FEM approach neither meshes nor solving large matrix

equations is required for PINNs. Instead the solution of a differential equation is obtained by constructing a loss function such that linear constraints are embedded during training. The training can be sped up and the accuracy of the model can be improved by enhancing the model with data-driven learning. In recent work benchmark linear continuum elasticity problems are solved accurately [83]. To the best of the author's knowledge no implementation of interacting devices or materials using PINNs has been published so far.

4.2 Seed sensitivity analysis

In this section the potential, limitations, and outlook of the third publication of this thesis is discussed in the context of simulation-based LDR prostate brachytherapy.

4.2.1 Potential

The sensitivity of dose parameters in LDR prostate brachytherapy has up to now been approached by performing statistical simulations of the seed positions and afterwards evaluating to resulting dose distributions [41, 7, 42, 43]. This was either performed to obtain general knowledge about placement tolerances or in an experimental study to improve plan robustness before the treatment. To the best of the author's knowledge this is the first work in which the subject of understanding the dose parameters' sensitivity with respect to seed placement has been tackled with a substantially different approach. By calculating the gradients of a dose parameter with respect to the seed positions using automatic differentiation of the dose calculation algorithm, we are moving away from solving this questions with classical simulations. Instead of repeating multiple dose calculations, it is now possible to answer the question of placement sensitivity with a simple backward pass during the computation. The gradients of the dose parameters with respect to the seed's positions can be directly translated into a placement tolerance of each seed. This has the potential of being integrated directly into the TPS and to provide newly updated information throughout the treatment inside the operating room.

In the statistical analysis of Nath et al. [41], a misplacement of less than $5\,mm$ at the needle base is suggested to preserve a good dose distribution. In the experiments with 35 patient data sets, we demonstrate that the gradients of the different dose parameters vary significantly between seeds. From this we can conclude that some needle placements are more sensitive than others. A deviation of less than $5\,mm$ may be required for some needles, whilst a wider tolerance may be acceptable for others. Instead of providing one tolerance

level as a general suggestion, it is now possible to assign a tolerance for each seed separately.

There are two stages at which the visualization of the placement tolerance can be beneficial for the LDR brachytherapy procedure:

During treatment planning it can be used to speed up manual planning and additionally to create robust treatment plans. After inverse treatment planning, it is a common procedure to manually change seed positions in the TPS in order to optimize the plan and improve the dose parameters. This is a time-consuming trial and error method and highly dependent on human experience. Showing the magnitudes of the gradients inside the TPS represents which seeds have a large influence on the desired dose parameter when moved and therefore are worth to be adjusted during manual planning. Additionally, the direction of the gradient leading to an increase of the desired dose parameter can be provided, assisting the physicist in determining which direction the seed should be moved. This is mostly beneficial for inexperienced medical physicists and can help to reduce the experience gap. Another advantage which can even assist expert treatment planners is the fact that by visualizing the gradients it is possible to understand how robust a plan is with respect to seed misplacement or seed migration. It was shown before that the clinical outcome is better when more robust treatment plans are utilized [7]. When small tolerances indicate that a misplacement will have a large effect on the resulting dose distribution, it is worth to adapt the treatment plan such that it is more robust to seed misplacement. With the introduced method this is feasible during treatment planing without the need for simulations.

During needle insertion the seed placement tolerance shows the operating physician how accurate the needles need to be placed. It becomes clear which needles may need repositioning due to small tolerances and for which needles a deviation from the planned position can be tolerated and a repeated needle insertion can be omitted. Since placed needles fixate the prostate, it can make the placement of the following needle more accurate. The knowledge about the most sensitive needles could therefore influence the placement order.

4.2.2 Limitation

The gradient, which is a linear approximation of the dose parameter's change due to seed movement, only accounts for displacements close to the current position. Using automatic differentiation to understand placement tolerance must be regarded as a local sensitivity measure ignoring potential alternate solutions located further away from the

present placement.

By calculating the gradients of the dose parameters with respect to each seed position a tolerance level for individual seeds is obtained. On the one hand this is an advantage compared to statistical simulations where the entire group of seeds is regarded and only statistical information about the seeds is gained. However, this comes with the disadvantage that an interplay between seed misplacements is not considered in the current model. While statistical seed displacement models and the dose calculations thereon consider the effect of moving all seeds at the same time, the gradient calculation implies that the remaining seeds are in their foreseen position. The impact of this effect must be evaluated further.

4.2.3 Further developments

The parameter translating the gradients to displacement tolerances and such the radii of the discs shown in the TPS are currently chosen arbitrarily. A comparison to a statistical seed displacement and such a parameter tuning needs to be performed in order to receive reliable allowed tolerances for the seed displacement.

When displaying a tolerance level during needle insertion, the gradients of different dose parameters are combined into one tolerance in order to account for multiple dose parameters at the same time. This is currently performed by weighting all dose parameters equally. As a possible extension a weighting could be added to the implementation reflecting the importance of certain objectives.

The next step is an integration of the automatic differentiation method into the clinical workflow. This will allow to study the clinical benefit of the method during every day procedures.

4.3 Clinical relevance

In this section the clinical relevance for the two developed methods to enhance treatment planning in existing treatment planning stategies is discussed. Moreover, an outlook on a clinical validation of the methods is presented.

4.3.1 Clinical relevance in existing planning strategies

During LDR brachytherapy treatments, physicians may encounter many problems. One such challenge is intestinal movement, which can significantly alter the prostate's geometry and necessitate re-planning, even in cases when some of the seeds have already been implanted. Unexpected patient movement while the anesthesia is not functioning properly is another potential complication. Despite their rarity, these cases highlight the urgent need for fast LDR treatments.

It is necessary to distinguish between different treatment planning strategies in order to assess the clinical significance of the methods that have been proposed for speeding up and thus enhancing prostate brachytherapy treatment planning.

Two stage pre-planning During two stage pre-planning the tissue deformation simulation with statistical variations of both the insertion angle and needle rotation can provide knowledge about critical needle positioning. It can predict seeds with large expected placement errors, help to avoid critical structures, and identify regions with limited seed and therefore dose coverage. When using the introduced diffuse domain method boundary conforming meshing of the structures is omitted. This comes with the benefit of less human interaction, as the automatic segmentation, regular meshing, and the finite element simulation can be performed in one pipeline without the need for manual interaction or a separate meshing software. While no real-time performance is required during pre-planning, large computation times, however, limit the acceptance in clinical planning routines. Besides the needle insertion simulation, the introduced seed sensitivity method is of high relevance for pre-planning procedures. Especially during pre-planning it is important to create robust treatment plans with large acceptable placement tolerances. This allows to achieve clinical targets even when there is no adaption of the plan during seed placement. Robust treatment plans ensure to deliver the desired target dose to the patient fast, because there is less need for reinserting needles when the aimed target position is missed. This prohibits complications due to long treatment times. Additionally, robust treatment plans allow to deliver the desired plan at first try and reduce the need for additional seed placements after a concluding CT scan.

Intra-operative pre-planning Simulation-based intra-operative planning comes with the challenge that fast computations are necessary to guarantee a fast and smooth surgery. An implementation of the needle insertion simulation therefore does not seem feasible in intra-operative planning. However, similar to two-stage pre-planning, intra-operative pre-planning highly benefits from robust treatment plans with all of the advantages mentioned

above. Incorporating automatic differentiation of the dose calculation into the TPS is easily applicable with a potentially large benefit for the treatment.

Interactive planning and dynamic dose calculation In contrast to the two pre-planning methods, the plan robustness is not as critical for interactive planning techniques to achieve the desired target dose, because the plan can be updated after seed placement. To reduce the time for the patient under anaesthesia and limit the mentioned complications it is reasonable to speed up the procedure. Robust treatment plans can therefore still improve interactive planning by minimizing the need for updating the treatment plan. By identifying seeds with large impact on specific dose parameters when being moved, the automatic differentiation can speed up manual planning and thus assist inexperienced medical physicists. Due to the lack of real-time computations the presented tissue deformation simulation cannot be used during interactive brachytherapy treatment planning.

Independent of the planning strategy, the visualization of a displacement tolerance during needle insertion can both speed up seed placement and patient recovery, because re-insertions of needles might be avoided when large tolerances are indicated.

Both of the introduced methods pave a path towards simulation-based treatment planning and improve the planning procedures by including both the uncertainty in seed placement through tissue deformation and the subsequent uncertainty of the dose distribution. As the automatic differentiation is easy to integrate into existing TPS and it can assist during both planning and needle insertion, this is considered to be the most significant contribution of this work.

4.3.2 Outlook for a clinical validation

The focus of this work is to provide methodological basis to transform static geometry-based LDR brachytherapy treatment planning into simulation-based treatment planning, including knowledge about plan robustness. As a next step these methods have to be transferred into a clinical setup and validated therein. For a validation on patient data a foregoing elastography can provide patient-specific elastic tissue parameters. Needle insertion simulations with varying tissue parameters can give an estimate on the placement uncertainty. While needle insertions performed by humans will lack reproducibility and are susceptible to manual interactions, the uncertainties can be validated by an experiment using robotic needle insertions with known insertion parameters. Using the expected placement uncertainties and the possibility to translate this to variations in the dose

parameters with the developed method, plans can be adapted in order to become more robust. As a last step, a study of LDR prostate brachytherapy treatments which compares both patients undergoing traditional or simulation-based treatment planning, can give insight whether the newly developed methods are beneficial to the patient.

5 Summary and Conclusion

In this work three publications which set a methodological basis for simulation-based low-dose-rate brachytherapy treatment planning are presented.

In the first two publications the development of a needle insertion FE simulation is presented. A flexible needle can be inserted into inhomogeneous tissue and released, which causes a relaxation of the tissue and the needle's position. By applying the diffuse domain approach, which is an embedded domain method, the underlying grid can be regularly meshed and tissue boundaries are represented by so-called phase field functions. These functions are one inside a tissue and smoothly transition to zero outside the tissue domain and can be obtained from probability maps from automated segmentation methods. The insertion process of a flexible needle was confirmed with a real-world experiment. Including elastic deformation simulations into brachytherapy treatment planning helps to include the needle insertion process into treatment planning and identify critical events, such as large expected placement errors. Performing multiple simulations with varying parameters can help to estimate expected placement variations. To be integrated into the clinical practise, it is important that no human interaction is necessary in order to not delay ongoing clinical routines. The possibility to avoid boundary conforming meshing and include geometric information directly through voxel data from the imaging modality can pave a path towards using elastic simulations in medical procedures. However, large computations times currently limit the acceptance of the method.

In the third publication a novel method to quantify the sensitivity of the dose parameters with respect to seed misplacement is introduced. While this problem is traditionally tackled with statistical simulations, up to now only statistical information about the placement tolerance was obtained. The newly introduced method avoids the statistical answer to this question, but instead calculates a sensitivity for each seed individually by calculating the derivatives of a dose parameter with respect to the seeds' positions. While an analysis how to convert gradients into real displacement tolerances is still to be performed, this approach is substantial due to its simple implementation on the one hand and the wide range of applications on the other. Firstly, it can help during brachytherapy treatment planning in order to understand the robustness of a treatment plan with respect to seed placement. Secondly, it can speed up manual treatment planning and make it less dependent on human experience, because seeds with large effects on specific dose parameters and the direction of preferred seed positioning can be indicated. Thirdly, it shows the allowed tolerances of the seeds during seed placements, indicating which needles might need to be re-inserted and which can remain in their position. All in all, this can reduce the overall implantation time.

In conclusion, this work shows that computational methods have not been fully exploited in LDR prostate brachytherapy treatment planning. In the history of brachytherapy, reliable dose calculations and optimization have been game changing in understanding, improving, and calculating LDR treatment plans. The presented methods lay the groundwork for risk-robust, simulation-based treatment planning and can be capable of transitioning LDR treatment planning towards more reliable and therefore faster and safer treatments. The offered approaches enhance the state-of-the-art on the one hand side by analyzing the uncertainty of the needle placement through simulations, which can provide an estimate of residual geometrical errors and information on needle navigation, and on the other hand side by assessing locally induced dosimetric errors as a function of seed misplacement. To finalize the concept of simulation-based treatment planning, the presented methods can now be integrated into clinical planning and evaluated there, which is the clinician's area of expertise. This is also where the benefits for the patient can be finally evaluated.

Data Accessibility

The code for the diffuse domain needle insertion simulation is openly available in Heidelberg Open Research Data at `https://doi.org/10.11588/data/QYCZLB`. Both patient data and code associated with the third paper is available under `https://doi.org/10.11588/data/Y3KIPM`.

List of Publications

Peer-reviewed publications included in this dissertation

K.I. Jerg, E.C.N. Okonkwo, F.A. Giordano, Y. Abo-Madyan, F. Momm, J.W. Hesser, "Real-time definition of single seed placement sensitivity in low-dose-rate prostate brachytherapy." *Brachytherapy.* 2023.

K.I. Jerg, L. Boggaram Naveen, G. Kanschat, E.C.N. Okonkwo, J.W. Hesser. "Diffuse domain approach for flexible needle insertion and relaxation." *Int J Numer Meth Biomed Engng.* p. e3782, 2023.

K.I. Jerg, R.P. Austermühl, K. Roth, J. Große Sundrup, G. Kanschat, J.W. Hesser, L Wittmayer. "Diffuse domain method for needle insertion simulations." *Int J Numer Meth Biomed Engng.* vol. 36, no. 9, p. e3377, 2020.

Other peer-reviewed publications

M.F.W. Dellmann, **K.I. Jerg**, J. Stratemeier, R. Heiman, J.W. Hesser, K.P. Aschenbrenner, M. Blessing. "Noise-robust breathing-phase estimation on marker-free, ultra low dose X-ray projections for real-time tumor localization via surrogate structures." *Zeitschrift für Medizinische Physik,* vol. 31, no. 4, pp. 355-364, 2021.

K.I. Jerg, Y. Lyatskaya, J. Stratemeier, J.W. Hesser, K.P. Aschenbrenner. "Conditional random fields for phase-based lung feature tracking with ultra-low-dose x-rays." *Medical Physics,* vol. 46, no. 5, pp. 2337-2346, 2019.

References

[1] L. Wang, B. Lu, M. He, Y. Wang, Z. Wang, and L. Du, "Prostate cancer incidence and mortality: global status and temporal trends in 89 countries from 2000 to 2019," *Frontiers in Public Health*, vol. 10, p. 176, 2022.

[2] World Cancer Research Fund International, "Global cancer incidence in men." `https://www.wcrf.org/cancer-trends/worldwide-cancer-data/`. last checked: 2023-12-23.

[3] N. G. Zaorsky, B. J. Davis, P. L. Nguyen, T. N. Showalter, P. J. Hoskin, Y. Yoshioka, G. C. Morton, and E. M. Horwitz, "The evolution of brachytherapy for prostate cancer," *Nature Reviews Urology*, vol. 14, no. 7, pp. 415–439, 2017.

[4] A. Henry, B. R. Pieters, F. A. Siebert, P. Hoskin, *et al.*, "Gec-estro acrop prostate brachytherapy guidelines," *Radiotherapy and Oncology*, vol. 167, pp. 244–251, 2022.

[5] P. Ghadjar, C. Fiorino, P. M. af Rosenschöld, M. Pinkawa, T. Zilli, and U. A. van Der Heide, "Estro acrop consensus guideline on the use of image guided radiation therapy for localized prostate cancer," *Radiotherapy and Oncology*, vol. 141, pp. 5–13, 2019.

[6] A. Karius, C. Schweizer, V. Strnad, M. Lotter, S. Kreppner, A. Lamrani, R. Fietkau, and C. Bert, "Seed-displacements in the immediate post-implant phase in permanent prostate brachytherapy," *Radiotherapy and Oncology*, vol. 183, p. 109590, 2023.

[7] R. Taschereau, J. Roy, and J. Pouliot, "Monte carlo simulations of prostate implants to improve dosimetry and compare planning methods," *Medical physics*, vol. 26, no. 9, pp. 1952–1959, 1999.

[8] A. Polo, C. Salembier, J. Venselaar, P. Hoskin, P. group of the GEC ESTRO, *et al.*, "Review of intraoperative imaging and planning techniques in permanent seed prostate brachytherapy," *Radiotherapy and Oncology*, vol. 94, no. 1, pp. 12–23, 2010.

[9] D. R. Reed, K. E. Wallner, G. S. Merrick, S. Arthurs, A. Mueller, W. Cavanagh, W. B. Butler, E. Ford, and S. G. Sutlief, "A prospective randomized comparison of stranded vs. loose 125i seeds for prostate brachytherapy," *Brachytherapy*, vol. 6, no. 2, pp. 129–134, 2007.

[10] D. B. Fuller, J. A. Koziol, and A. C. Feng, "Prostate brachytherapy seed migration and dosimetry: analysis of stranded sources and other potential predictive factors," *Brachytherapy*, vol. 3, no. 1, pp. 10–19, 2004.

[11] G. Wei, P. Jiang, C. Li, S. Wei, Y. Jiang, H. Sun, and J. Wang, "A review on permanent implants for prostate brachytherapy with comparison between stranded and loose seeds," *Japanese Journal of Radiology*, pp. 1–12, 2022.

[12] S. Daniel, C. Rabbani, A. Aref, R. Taylor, D. Patel, and P. J. Chuba, "Three-dimensional visualization and dosimetry of stranded source migration following prostate seed implant," *Practical Radiation Oncology*, vol. 2, no. 3, pp. 193–200, 2012.

[13] C. Lee, "Recent developments and best practice in brachytherapy treatment planning," *The British journal of radiology*, vol. 87, no. 1041, p. 20140146, 2014.

[14] S. Langley, J. Uribe, S. Uribe-Lewis, J. Money-Kyrle, C. Perna, S. Khaksar, R. Soares, and R. Laing, "Comparative analysis of clinical outcomes and procedural costs between the conventional two-stage technique and 4d brachytherapy for early prostate cancer," *Clinical Oncology*, vol. 30, no. 1, pp. 57–64, 2018.

[15] H. Matzkin, J. Chen, L. German, and N. J. Mabjeesh, "Comparison between preoperative and real-time intraoperative planning 125i permanent prostate brachytherapy: Long-term clinical biochemical outcome," *Radiation Oncology*, vol. 8, no. 1, pp. 1–8, 2013.

[16] S. Nag, J. P. Ciezki, R. Cormack, S. Doggett, K. DeWyngaert, G. K. Edmundson, R. G. Stock, N. N. Stone, Y. Yu, M. J. Zelefsky, *et al.*, "Intraoperative planning and evaluation of permanent prostate brachytherapy: report of the american brachytherapy society," *International Journal of Radiation Oncology* Biology* Physics*, vol. 51, no. 5, pp. 1422–1430, 2001.

[17] K. Yoshida, T. Ohashi, A. Yorozu, K. Toya, T. Nishiyama, S. Saito, T. Hanada, Y. Shiraishi, and N. Shigematsu, "Comparison of preplanning and intraoperative planning for i-125 prostate brachytherapy," *Japanese journal of clinical oncology*, vol. 43, no. 4, pp. 383–389, 2013.

[18] S. S. Dhaliwal, T. Chettibi, S. Wilby, W. Polak, A. L. Palmer, N. Reynaert, and R. Merzouki, "Review of clinical and technological consideration for mri-guided robotic prostate brachytherapy," *IEEE Transactions on Medical Robotics and Bionics*, vol. 3, no. 3, pp. 583–605, 2021.

[19] Eurostat, "Availability of ct and mri units in hospitals." `https://ec.europa.eu/eurostat/fr/web/products-eurostat-news/-/DDN-20200724-1`. last checked: 2023-12-05.

[20] M. K. Rooney, F. Zhu, E. F. Gillespie, J. R. Gunther, R. P. McKillip, M. Lineberry, A. Tekian, and D. W. Golden, "Simulation as more than a treatment-planning tool: A systematic review of the literature on radiation oncology simulation-based medical education," *International Journal of Radiation Oncology* Biology* Physics*, vol. 102, no. 2, pp. 257–283, 2018.

[21] K. Chethan, M. Zuber, S. Shenoy, *et al.*, "Finite element analysis of different hip implant designs along with femur under static loading conditions," *Journal of Biomedical Physics & Engineering*, vol. 9, no. 5, p. 507, 2019.

[22] Q. Zhang, T. Chon, Y. Zhang, J. S. Baker, and Y. Gu, "Finite element analysis of the lumbar spine in adolescent idiopathic scoliosis subjected to different loads," *Computers in Biology and Medicine*, vol. 136, p. 104745, 2021.

[23] M. Hirschhorn, V. Tchantchaleishvili, R. Stevens, J. Rossano, and A. Throckmorton, "Fluid–structure interaction modeling in cardiovascular medicine–a systematic review 2017–2019," *Medical engineering & physics*, vol. 78, pp. 1–13, 2020.

[24] T. Canchi, A. Saxena, E. Ng, E. C. Pwee, and S. Narayanan, "Application of fluid–structure interaction methods to estimate the mechanics of rupture in asian abdominal aortic aneurysms," *Bionanoscience*, vol. 8, pp. 1035–1044, 2018.

[25] C. M. Scotti, A. D. Shkolnik, S. C. Muluk, and E. A. Finol, "Fluid-structure interaction in abdominal aortic aneurysms: effects of asymmetry and wall thickness," *Biomedical engineering online*, vol. 4, pp. 1–22, 2005.

[26] R. Campobasso, F. Condemi, M. Viallon, P. Croisille, S. Campisi, and S. Avril, "Evaluation of peak wall stress in an ascending thoracic aortic aneurysm using fsi simulations: effects of aortic stiffness and peripheral resistance," *Cardiovascular engineering and technology*, vol. 9, pp. 707–722, 2018.

[27] G. Li, H. Wang, M. Zhang, S. Tupin, A. Qiao, Y. Liu, M. Ohta, and H. Anzai, "Prediction of 3d cardiovascular hemodynamics before and after coronary artery bypass surgery via deep learning," *Communications biology*, vol. 4, no. 1, p. 99, 2021.

[28] M. Fu, O. Salzman, and R. Alterovitz, "Toward certifiable motion planning for medical steerable needles," *Robotics science and systems: online proceedings*, vol. 2021, 2021.

[29] R. Alterovitz, K. Goldberg, J. Pouliot, R. Taschereau, and I.-C. Hsu, "Needle insertion and radioactive seed implantation in human tissues: Simulation and sensitivity

analysis," in *2003 IEEE International Conference on Robotics and Automation (Cat. No. 03CH37422)*, vol. 2, pp. 1793–1799, IEEE, 2003.

[30] N. Chentanez, R. Alterovitz, D. Ritchie, L. Cho, K. K. Hauser, K. Goldberg, J. R. Shewchuk, and J. F. O'Brien, "Interactive simulation of surgical needle insertion and steering," *ACM SIGGRAPH 2009 papers*, pp. 1–10, 2009.

[31] O. Goksel, E. Dehghan, and S. E. Salcudean, "Modeling and simulation of flexible needles," *Medical engineering & physics*, vol. 31, no. 9, pp. 1069–1078, 2009.

[32] Z. Zhang, Y. Wang, P. K. Jimack, and H. Wang, "Meshingnet: A new mesh generation method based on deep learning," in *International Conference on Computational Science*, pp. 186–198, Springer, 2020.

[33] A. Neic, M. A. Gsell, E. Karabelas, A. J. Prassl, and G. Plank, "Automating image-based mesh generation and manipulation tasks in cardiac modeling workflows using meshtool," *SoftwareX*, vol. 11, p. 100454, 2020.

[34] C. Geuzaine and J.-F. Remacle, "Gmsh: A 3-d finite element mesh generator with built-in pre-and post-processing facilities," *International journal for numerical methods in engineering*, vol. 79, no. 11, pp. 1309–1331, 2009.

[35] R. Hess, *The essential Blender: guide to 3D creation with the open source suite Blender*. No Starch Press, 2007.

[36] E. Madenci and I. Guven, *The finite element method and applications in engineering using ANSYS®*. Springer, 2015.

[37] M. Fedele and A. Quarteroni, "Polygonal surface processing and mesh generation tools for the numerical simulation of the cardiac function," *International Journal for Numerical Methods in Biomedical Engineering*, vol. 37, no. 4, p. e3435, 2021.

[38] J. Kockelkoren, H. Levine, and W.-J. Rappel, "Computational approach for modeling intra-and extracellular dynamics," *Physical Review E*, vol. 68, no. 3, p. 037702, 2003.

[39] S. Shah, L. Kallivokas, B. Jaramaz, O. Ghattas, and A. DiGioia, "The fictitious domain method for patientspecific biomechanical modeling: promise and prospects," in *Second Annual International Symposium on Medical Robotics and Computer Assisted Surgery, MRCAS*, vol. 95, p. 329, 1995.

[40] X. Li, J. Lowengrub, A. Rätz, and A. Voigt, "Solving pdes in complex geometries: a diffuse domain approach," *Communications in mathematical sciences*, vol. 7, no. 1, p. 81, 2009.

[41] S. Nath, Z. Chen, N. Yue, S. Trumpore, and R. Peschel, "Dosimetric effects of needle divergence in prostate seed implant using and radioactive seeds," *Medical physics*, vol. 27, no. 5, pp. 1058–1066, 2000.

[42] J. Dawson, T. Wu, T. Roy, J. Gu, and H. Kim, "Dose effects of seeds placement deviations from pre-planned positions in ultrasound guided prostate implants," *Radiotherapy and Oncology*, vol. 32, no. 3, pp. 268–270, 1994.

[43] L. Beaulieu, L. Archambault, S. Aubin, E. Oral, R. Taschereau, and J. Pouliot, "The robustness of dose distributions to displacement and migration of 125i permanent seed implants over a wide range of seed number, activity, and designs," *International Journal of Radiation Oncology* Biology* Physics*, vol. 58, no. 4, pp. 1298–1308, 2004.

[44] K. I. Jerg, R. P. Austermühl, K. Roth, J. Große Sundrup, G. Kanschat, J. W. Hesser, and L. Wittmayer, "Diffuse domain method for needle insertion simulations," *International Journal for Numerical Methods in Biomedical Engineering*, vol. 36, no. 9, p. e3377, 2020.

[45] K. I. Jerg, L. Boggaram Naveen, G. Kanschat, E. C. N. Okonkwo, and J. W. Hesser, "Diffuse domain approach for flexible needle insertion and relaxation," *International Journal for Numerical Methods in Biomedical Engineering*, p. e3782, 2023.

[46] K. I. Jerg, E. C. N. Okonkwo, F. A. Giordano, Y. Abo-Madyan, F. Momm, and J. W. Hesser, "Real-time definition of single seed placement sensitivity in low-dose-rate prostate brachytherapy," *Brachytherapy*, 2023.

[47] Stiftung Deutsche Krebshilfe, Buschstr. 32 53113 Bonn, "Strahlentherapie (radiotherapie, radiatio)." `https://www.krebshilfe.de/informieren/therapie/strahlentherapie-radiotherapie-radiatio/`. last checked: 2023-12-23.

[48] R. K. Funk, A. L. Stockham, and N. N. I. Laack, "Basics of radiation therapy," *Clinical Cardio-Oncology*, pp. 39–60, 2016.

[49] M. J. Gazda and L. R. Coia, "Principles of radiation therapy," *Cancer management: a multidisciplinary approach*, 2001.

[50] S. Pölz and B. Breustedt, "Personalised body counter calibration using anthropometric parameters," *Radiation protection dosimetry*, vol. 170, no. 1-4, pp. 221–224, 2016.

[51] R. Pacelli and L. Mansi, "Eric Hall and Amato J. Giaccia: Radiobiology for the radiologist, 6th edn. Lippincott Wilkins & Williams, Philadelphia, USA, 2006, ISBN: 0-7817-4151-3," 2007.

[52] B. J. Stish, B. J. Davis, L. A. Mynderse, R. H. McLaren, C. L. Deufel, and R. Choo, "Low dose rate prostate brachytherapy," *Translational andrology and urology*, vol. 7, no. 3, p. 341, 2018.

[53] Eckert & Ziegler, BEBIG GmbH, "Ldr prostate seed brachytherapy." `https://shop.bebig.com/`. last checked: 2023-10-27.

[54] Eckert & Ziegler, BEBIG GmbH, "Nadeln für die ldr-brachytherapie." `https://medical.ezag.com/de/products/ldr-nadeln/`. last checked: 2023-10-27.

[55] H. H. Holm, "The history of interstitial brachytherapy of prostatic cancer," in *Seminars in surgical oncology*, vol. 13, pp. 431–437, Wiley Online Library, 1997.

[56] M. J. Rivard, J. L. Venselaar, and L. Beaulieu, "The evolution of brachytherapy treatment planning," *Medical physics*, vol. 36, no. 6Part1, pp. 2136–2153, 2009.

[57] Mayo Foundation for Medical Education and Research (MFMER), "Permanent prostate brachytherapy." `https://www.mayoclinic.org/tests-procedures/prostate-brachytherapy/multimedia/permanent-prostate-brachytherapy/img-20008710`. last checked: 2023-10-27.

[58] C. V. Guthier, *Development of a real-time inverse planning system for radiation therapy based on compressed sensing*. PhD thesis, 2015.

[59] R. Nath, L. L. Anderson, G. Luxton, K. A. Weaver, J. F. Williamson, and A. S. Meigooni, "Dosimetry of interstitial brachytherapy sources: recommendations of the aapm radiation therapy committee task group no. 43," *Medical physics*, vol. 22, no. 2, pp. 209–234, 1995.

[60] M. J. Rivard, B. M. Coursey, L. A. DeWerd, W. F. Hanson, M. Saiful Huq, G. S. Ibbott, M. G. Mitch, R. Nath, and J. F. Williamson, "Update of aapm task group no. 43 report: A revised aapm protocol for brachytherapy dose calculations," *Medical physics*, vol. 31, no. 3, pp. 633–674, 2004.

[61] C. Salembier, P. Lavagnini, P. Nickers, P. Mangili, A. Rijnders, A. Polo, J. Venselaar, P. Hoskin, *et al.*, "Tumour and target volumes in permanent prostate brachytherapy: a supplement to the estro/eau/eortc recommendations on prostate brachytherapy," *Radiotherapy and oncology*, vol. 83, no. 1, pp. 3–10, 2007.

[62] N. M. Boroujeni, J.-P. P. Richard, D. Sterling, and C. Wilke, "A linear optimization model for high dose rate brachytherapy using a novel distance metric," *Physics in Medicine & Biology*, vol. 68, no. 17, p. 175018, 2023.

[63] C. V. Guthier, P. F. Orio III, I. Buzurovic, and R. A. Cormack, "Knowledge-based inverse treatment planning for low-dose-rate prostate brachytherapy," *Medical Physics*, vol. 48, no. 5, pp. 2108–2117, 2021.

[64] H.-P. Wieser, E. Cisternas, N. Wahl, S. Ulrich, A. Stadler, H. Mescher, L.-R. Müller, T. Klinge, H. Gabrys, L. Burigo, *et al.*, "Development of the open-source dose calculation and optimization toolkit matrad," *Medical Physics*, vol. 44, no. 6, pp. 2556–2568, 2017.

[65] J. Jiang, Y. Guo, Z. Bi, Z. Huang, G. Yu, and J. Wang, "Segmentation of prostate ultrasound images: the state of the art and the future directions of segmentation algorithms," *Artificial Intelligence Review*, vol. 56, no. 1, pp. 615–651, 2023.

[66] X. Wang, Z. Chang, Q. Zhang, C. Li, F. Miao, and G. Gao, "Prostate ultrasound image segmentation based on dsu-net," *Biomedicines*, vol. 11, no. 3, p. 646, 2023.

[67] X. Xu, T. Sanford, B. Turkbey, S. Xu, B. J. Wood, and P. Yan, "Polar transform network for prostate ultrasound segmentation with uncertainty estimation," *Medical Image Analysis*, vol. 78, p. 102418, 2022.

[68] R. W. Ogden, *Non-linear elastic deformations*. Courier Corporation, 1997.

[69] M. B. Boubaker, M. Haboussi, J.-F. Ganghoffer, and P. Aletti, "Predictive model of the prostate motion in the context of radiotherapy: a biomechanical approach relying on urodynamic data and mechanical testing," *Journal of the mechanical behavior of biomedical materials*, vol. 49, pp. 30–42, 2015.

[70] G. Ravali and M. Manivannan, "Haptic feedback in needle insertion modeling and simulation," *IEEE reviews in biomedical engineering*, vol. 10, pp. 63–77, 2017.

[71] N. Abolhassani, R. Patel, and F. Ayazi, "Needle control along desired tracks in robotic prostate brachytherapy," in *2007 IEEE international conference on systems, man and cybernetics*, pp. 3361–3366, IEEE, 2007.

[72] H. Kataoka, T. Washio, M. Audette, and K. Mizuhara, "A model for relations between needle deflection, force, and thickness on needle penetration," in *Medical Image Computing and Computer-Assisted Intervention–MICCAI 2001: 4th International*

Conference Utrecht, The Netherlands, October 14–17, 2001 Proceedings 4, pp. 966–974, Springer, 2001.

[73] T. Lehmann, M. Tavakoli, N. Usmani, R. Sloboda, *et al.*, "Force-sensor-based estimation of needle tip deflection in brachytherapy," *Journal of Sensors*, vol. 2013, 2013.

[74] K. Yan, W. S. Ng, K. V. Ling, Y. Yu, T. Podder, T.-I. Liu, and C. Cheng, "Needle steering modeling and analysis using unconstrained modal analysis," in *The First IEEE/RAS-EMBS International Conference on Biomedical Robotics and Biomechatronics, 2006. BioRob 2006.*, pp. 87–92, IEEE, 2006.

[75] M. G. Jushiddi, J. J. Mulvihill, D. Chovan, A. Mani, C. Shanahan, C. Silien, S. A. M. Tofail, and P. Tiernan, "Simulation of biopsy bevel-tipped needle insertion into soft-gel," *Computers in biology and medicine*, vol. 111, p. 103337, 2019.

[76] O. Goksel, S. E. Salcudean, S. P. DiMaio, R. Rohling, and J. Morris, "3d needle-tissue interaction simulation for prostate brachytherapy," in *Medical Image Computing and Computer-Assisted Intervention–MICCAI 2005: 8th International Conference, Palm Springs, CA, USA, October 26-29, 2005, Proceedings, Part I 8*, pp. 827–834, Springer, 2005.

[77] S. P. DiMaio and S. E. Salcudean, "Interactive simulation of needle insertion models," *IEEE transactions on biomedical engineering*, vol. 52, no. 7, pp. 1167–1179, 2005.

[78] N. Abolhassani, R. Patel, and M. Moallem, "Needle insertion into soft tissue: A survey," *Medical engineering & physics*, vol. 29, no. 4, pp. 413–431, 2007.

[79] S. P. DiMaio and S. E. Salcudean, "Needle insertion modeling and simulation," *IEEE Transactions on robotics and automation*, vol. 19, no. 5, pp. 864–875, 2003.

[80] Y. Ji, L. Ruan, W. Ren, G. Dun, J. Liu, Y. Zhang, and Q. Wan, "Stiffness of prostate gland measured by transrectal real-time shear wave elastography for detection of prostate cancer: a feasibility study," *The British journal of radiology*, vol. 92, no. 1097, p. 20180970, 2019.

[81] J. M. Betts, C. Mears, H. M. Reynolds, M. A. Ebert, and A. Haworth, "Prostate cancer focal brachytherapy: Improving treatment plan robustness using a convolved dose rate model," *Procedia computer science*, vol. 108, pp. 1522–1531, 2017.

[82] M. Raissi, P. Perdikaris, and G. E. Karniadakis, "Physics-informed neural networks: A deep learning framework for solving forward and inverse problems involving nonlinear partial differential equations," *Journal of Computational physics*, vol. 378, pp. 686–707, 2019.

[83] A. M. Roy, R. Bose, V. Sundararaghavan, and R. Arróyave, "Deep learning-accelerated computational framework based on physics informed neural network for the solution of linear elasticity," *Neural Networks*, vol. 162, pp. 472–489, 2023.

Acknowledgements

I would like to express my gratitude to numerous people without whom this thesis would not have been possible:

- **Prof. Dr. Jürgen Hesser** Thank you for giving me the opportunity to work on this topic and to be part of your research group. Especially, I appreciate your openness and trust to let me work on my ideas and offering your help where I needed it. I am grateful for your constant support and guidance throughout the past years. Last but not least, I want to thank you for acquiring financial support for this work, such as the DFG grant number HE 3011/36-1.
- **Prof. Dr. Guido Kanschat** Thank you for offering mathematical support and the helpful discussions.
- **Prof. Dr. Mark Ladd** Thank you for showing interest in my work and becoming a referee for this thesis.
- **Prof. Dr. Andreas Mielke and Prof. Dr. Rüdiger Klingeler** Thank you for agreeing to be a committee member for the oral examination.
- **My colleagues** I want to thank Yasser Abo-Madyan and Ernest Okonkwo for the clinical insights regarding brachytherapy. My special gratitude goes to Ernest for inviting me to Offenburg and providing patient data, which I used for my research. Moreover, I want to thank Lisa Wittmayer for introducing me to diffuse domain FE simulations and René Austermühl for many fruitful discussions regarding simulation design and code architecture. Lastly, I appreciate the discussions and constructive comments from Tobias Meißner and Sara Monji-Azad.
- **My family** My special thanks goes to my parents for supporting me in pursuing my goals and Manuela and Tobias for always being there and encouraging me.